From the holdings of the Department of Special Collections , Princeton University Library, Princeton, NJ

These documents are either in the public domain, or can only be used for educational and research purposes (Fair use) as per U.S. Copyright law (text below). By accessing this file, all users agree that their use falls in the public domain or within fair use as defined by the copyrightlaw. We do not charge any permission or usage fees for the publication of images of material inour collections, including those provided by Princeton University Library, via our website, catalog, or directly from staff.For more information regarding copyright, credit, and citation please review the information onthe Copyright, Credit and Citation Guidelines page of our website.
https://library.princeton.edu/special-collections/policies/copyright-credit-and-citation-guidelines. If you have any questions, including how to order higher-quality images from the collection, contact Special Collections Public Services via our Ask Us! Form. https://library.princeton.edu/special-collections/ask-us

---

Doctoral Dissertations, 2011-2026 Atmospheric and Oceanic Sciences

2017

Aspects of Eddy Momentum Fluxes in the General Circulation of the Troposphere

Lutsko, Nicholas

Princeton, NJ : Princeton University

---

http://arks.princeton.edu/ark:/88435/dsp015q47rr38h

U.S. Copyright law: The copyright law of the United States (Title 17, §108, United States Code) governs the making of photocopies or other reproductions of copyrighted material. Under certain conditions specified in the law, libraries and archives are authorized to furnish a photocopy or other reproduction. One of these specified conditions is that the photocopy or reproduction is not to be used for any purpose other than private study, scholarship, or research. If a user makes a request for, or later uses, a photocopy or reproduction for purposes in excess of fair use that user may be liable for copyright infringement. This institution reserves the right to refuse to accept a copying order if, in its judgment, fulfillment of the order would involve a violation of copyright law. https://www.copyright.gov/title17/title17.pdf

Aspects of Eddy Momentum Fluxes in the General Circulation of the Troposphere

Nicholas James Lutsko

A Dissertation
Presented to the Faculty
of Princeton University
in Candidacy for the Degree
of Doctor of Philosophy

Recommended for Acceptance
by the Program in Atmospheric and Oceanic Sciences
Adviser: Professor Isaac M. Held

September 2017

© Copyright by Nicholas James Lutsko, 2017.

All rights reserved.

Abstract

This thesis investigates the roles of eddy momentum fluxes (EMFs) in several aspects of the tropospheric circulation. The thesis begins by examining how large-scale orographic forcing and ENSO-like equatorial heating affect horizontal EMFs in a multi-layer primitive equation model (the GCM). For the orographic forcing a transition is seen from a linear regime, in which the response is dominated by zonal propagation, to a nonlinear regime, in which the response mostly propagates meridionally. The dynamics of this transition are investigated by comparing the behavior of the GCM with simpler models and it is also shown that the transition leads to relatively larger stationary EMFs in the nonlinear regime. In the equatorial heating experiments the winds in the deep tropics accelerate as the strength of the heating is applied and eventually superrotate. The superrotation is driven by the EMFs due to the stationary waves excited by the heating, and is closely related to the breakdown of the GCM's linear response.

Complementing these, the second half of the thesis consists of two projects which study the relationship between EMFs and mid-latitude jets. First, the EMFs in the lower troposphere of two idealized models as well as in a reanalysis dataset are investigated. The pattern of lower tropospheric EMFs is remarkably similar across the datasets, with even a two-layer quasi-geostrophic (QG) model capturing the basic structure seen in the reanalysis data of EMF divergence in the center of the jet at slow phase speeds and EMF convergence at fast phase speeds. A physical picture of the underlying dynamics is presented based on the dynamics of the QG model.

Finally, the Fluctuation-Dissipation Theorem (FDT) is used to predict how the two-layer QG model responds to small, zonally-symmetric perturbations. It is found that the FDT can accurately predict the models response to barotropic perturbations (perturbations with the same magnitude and sign in each layer) but is less successful at predicting the response to baroclinic perturbations (perturbations with the same

magnitude but opposite sign in each layer). Some alternative strategies for producing better FDT estimates are investigated, and these may be relevant for studies with more comprehensive atmospheric models.

Acknowledgements

There are many people to thank for the scientific and emotional support I needed to complete this thesis. My family comes first of course: Mummy, Papa, Chris, Sniffy, Oma and Opa, Nana and Gary, the Worthingtons, Minerva – Thank you!

I am deeply grateful for the privilege of working with my adviser, Isaac Held. Isaac was patient with me, invested in my work and always made time to meet with me for as long as I needed. He taught me so much about the climate system, and also about how to be a good scientist. I have found the example he sets to be inspirational, and I hope I can apply some of the lessons he taught me to the rest of my research career.

Working in Princeton, I've met so many interesting people, who have helped in different ways. I thank my cohort for these past five years: Anna T (and Curt and Cholla!), Jane and Rob. We're an unlikely bunch but they are my oldest friends in Princeton. Anna FitzMaurice was the perfect tea-partner and put up with my mischief, as did the rest of her harem: Natasha, Charlotte and Hannah. Spencer Hill was a great office-mate – when he came in – and shared my enthusiasm for discovering the world of climate science. Max was nostalgic for Europe with me, and I'm glad we were able to collaborate on a project eventually. Carl taught me about wines and knife skills while we talked about the NBA, Zizek and Gaussian mountains. Samantha ate breakfast with me on Saturday mornings and explained New Jersey to me. I also thank Chris Rogerson and Jacob for 5 years of Cut the Check, great meals and good basketball talk. Outside of Princeton, Christian, Ben and Chris Hunter rooted for me from afar, made every effort to visit me and gave great banter. I owe Harriet more thanks than anyone else, and I wouldn't have gotten this far with out her. I also thank the Laus for their constant kindness and support.

Being part of the AOS program and working at GFDL, I have always felt that I had limitless resources at my disposal, which I have perhaps taken for granted at times. The GFDL technical staff provided me with a lot of help and I thank GFDL

for giving me more computer resources than I've needeeds. My committee – Steve Garner, Tim DelSole and Stephan Fueglistaler – was underused, but I benefited from speaking with them individually, especially Stephan who was a great resource for me the past five years. Yi Ming kindly agreed to be a reader for me, and I had a lot of fun hanging out with him around the lab and at conferences. I also thank Pablo Zurita-Gotor for his patience with my mistakes and the time he put in to help me with my projects. The thesis has benefited a lot from his efforts. I wouldn't be able to graduate without Anna Valerio, who put up with my administrative incompetence for five years and somehow managed to keep me on track. Finally, I thank the Princeton/NOAA Cooperative Institute for Climate Science for funding my first two years here and I thank the NSF for kindly awarding me the grant which has supported me the past three years.

Dedicated to my family: Mummy, Papa and Chris.

Contents

Abstract iii

Acknowledgements v

List of Tables xii

List of Figures xiii

1 Introduction **1**

2 The Response of an Idealized Atmosphere to Orographic Forcing: Zonal vs Meridional Propagation **8**

2.1 Introduction 8

2.2 Primitive Equation Model and Experiments 12

2.3 Primitive Equation Model Results 13

2.3.1 The small mountains 13

2.3.2 The large mountains 17

2.3.3 Mountain torque 20

2.3.4 Plumb flux 23

2.4 Other Model Configurations 26

2.4.1 Adding orography to a winter-like climate 26

2.4.2 Removing the mountain-induced radiative cooling 28

2.5 Understanding the Linear Response 29

2.5.1 Barotropic model formulation 29

2.5.2 Mimicking the responses of the GCM 31
2.5.3 The index of refraction and the barotropic model 33
2.6 Understanding the Nonlinear Response 36
2.6.1 Vertical motion along the mountain surface 36
2.6.2 Plumb fluxes in the barotropic model 38
2.7 Conclusion 41

3 The Impact of Orographic Forcing on the Momentum Budget of a Dry Atmosphere 44
3.1 Introduction 44
3.2 Momentum Budget of the Control Integration 47
3.3 Response to Small Mountains 48
3.3.1 Normalized torque and stationary EMF convergence 48
3.3.2 Stationary wave model results 49
3.4 Responses to Large Mountains 55
3.4.1 Responses of the torque and the stationary EMF convergence 55
3.4.2 Responses of the friction and the transient EMF convergence . 57
3.5 Conclusion 60

4 The Response of Dry Atmospheres to ENSO-like Heating: Superrotation and the Breakdown of Linear Theory 63
4.1 Introduction 63
4.2 Model and Experiments 66
4.3 Responses to Heating 68
4.3.1 Eddy streamfunction and zonal-mean wind responses 68
4.3.2 Vorticity budget analysis 72
4.4 Zonal Momentum Budget 78
4.5 Varying the Baroclinicity 84

4.6 Constraining the Tropical Static Stability 88
4.7 Conclusion 91

5 Lower Tropospheric Eddy Momentum Fluxes in Idealized Models and Reanalysis Data 94

5.1 Introduction 94
5.2 Data, Models and Methods 96
5.2.1 Reanalysis data 96
5.2.2 Two-layer QG model 96
5.2.3 Primitive equation model 98
5.2.4 Methods 99
5.3 EMFs in Reanalysis Data 99
5.4 EMF spectra of the Idealized Models 103
5.5 Effects of varying the frictional time-scale 109
5.6 Interpretation of the Lower Tropospheric Spectra 111
5.7 Conclusion 115

6 Applying the Fluctuation-Dissipation Theorem to a Two-Layer Model of Quasi-Geostrophic Turbulence 117

6.1 Introduction 117
6.2 Methodology 121
6.2.1 Model formulation 121
6.2.2 Control simulations and perturbations 122
6.2.3 Regularization Strategy 126
6.2.4 Testing Gaussianity 128
6.2.5 Another Computational Note 129
6.3 Model Results 129
6.3.1 Behavior of the model as β is increased 129

6.3.2 Model Responses 133
6.4 FDT Calculations 136
6.4.1 Choosing how many EOFs to retain 136
6.4.2 Barotropic Perturbation 139
6.4.3 Baroclinic Perturbation 145
6.5 Conclusions 150

7 Conclusion **153**
7.1 Summary 153
7.2 Discussion 156

A Cooper-Haynes Algorithm **159**

Bibliography **161**

List of Tables

4.1 List of experiments performed with the Held and Suarez set-up. Δ_y is the equator-to-pole temperature difference in the equilibrium temperature profile. 68

List of Figures

1.1 Climatological December-January-February (DJF) deviations from the zonal-mean ("eddy") geopotential height at 300hPa for 1979 to 2013 from the ERA-Interim reanalysis dataset [23]. The large-scale waves seen in the Northern Hemisphere are a superposition of quasi-stationary Rossby waves forced by orography and by heating. . 4

1.2 Total cloud cover on January 14th 2010 as measured by the Clouds and the Earth's Radiant Energy System (CERES) experiment. 6

2.1 Latitude/longitude cross-sections taken at 350hPa of the eddy stream-function response of the primitive equation model to idealized topography with $H = 250$m (top left), $H = 333$m (top right), $H = 400$m (center left), $H = 500$m (center right) and $H = 700$m (bottom left). The responses have been normalized by 1000m $/H$ and the data is plotted using a polar stereographic projection. The green ovals show the H / 2 contour. 14

2.2 Pressure/longitude cross-sections taken at 46° latitude of the eddy zonal wind response of the primitive equation model to idealized topography with $H = 250$m (top left), $H = 333$m (top right), $H = 400$m (center left), $H = 500$m (center right) and $H = 700$m (bottom left). The contour interval is 0.5 ms^{-1}, the zero contour is shown by a thicker line and areas of negative winds are shaded in gray. The responses have been normalized by 1000m $/H$. 15

2.3 Left: the time-averaged zonal-mean zonal wind profile from a control simulation of the primitive equation model at 300hPa, 350hPa, 400hPa and 450hPa (solid lines) and the zonal wind profile at 350hPa from an unperturbed experiment with $\epsilon = 10$K (dashed). Right: the profiles of the index of refraction n_s^2 for each of these. Zonal wavenumbers to the left of the curves are able to propagate while those to the right are evanescent. 16

2.4 As in Figure 2.1 but for $H = 1$km (top left), $H = 2$km (top right), $H = 3$km (center left), $H = 4$km (center right) and $H = 5$km (bottom left). The responses have again been normalized by 1000m $/H$ and the same color scale is used. 18

2.5 The un-normalized eddy streamfunction responses at 350hPa for $H = 4$km (top) and $H = 5$km (bottom). The contour interval is 10 m^2s^{-1} between -100 and 100m^2s^{-1} and then the interval is 50 m^2s^{-1} between ± 100 and $\pm 400\text{m}^2\text{s}^{-1}$. Black contours have been added for clarity. . . 19

2.6 As in Figure 2.2 but for $H = 1$km (top left), $H = 2$km (top right), $H = 3$km (center left), $H = 4$km (center right) and $H = 5$km (bottom left), and the responses have not been normalized. The contour interval is 1 ms^{-1}, the zero contour is shown by a thicker line and areas of negative winds are shaded in gray. Where visible the mountains are shaded in black. 20

2.7 The normalized eddy streamfunction responses at 350hPa to mountains with $H = 333$m (top), 700m (middle) and 4km (bottom) from simulations run at T85 resolution. 21

2.8 The normalized zonally-averaged mountain torque per degree latitude T for the primitive equation experiments with $H < 1$km (left) and with $H \geq 1$km (right). For each curve the shading envelopes the region between T calculated using the first half of the simulation and T calculated using the second half of the simulation. 22

2.9 The normalized Plumb wave activity flux vectors at 350hPa (arrows), the normalized divergence of the Plumb flux (shading), the critical line ($u = 0$, red) and the $n_s^2 = 5.1$ contours (green) for the primitive equation model experiments with $H = 333$m (top), 1km (center) and 2km (bottom) experiments. Regions of flux convergence are shaded and the contour interval is $2 \times 10^{-6}\text{ms}^{-2}$. 24

2.10 The ratio of the meridional component of the Plumb flux integrated across the 30°N latitude circle to the zonal component of the Plumb flux integrated across the 160° longitude circle plotted as a function of H. Note the logarithmic scale on the x-axis. 25

2.11 Same as Figure 2.9 but for experiments with $\epsilon = 10$K. The top panel shows the response to a 400m Gaussian mountain and the bottom experiment shows the response to a 400m ridge-like mountain. The contour interval is now 4×10^{-6}ms^{-2} and the green lines show the $n_s = 4^4$ contours. 27

2.12 Vertically averaged radiative heating rate in the $H = 2$km case. The green oval shows the 1km contour of the mountain. 28

2.13 Normalized eddy streamfunction responses at 350hPa for three different mountain heights with the new T_{eq} fields that remove the vertically-averaged radiative heating. 30

2.14 Left: the eddy streamfunction responses for three values of H_b from the barotropic simulations with the time-averaged zonal-mean zonal wind profile at 350hPa from the control simulation of the primitive equation model with $\epsilon = 0$K, normalized by 1000m / H_b and plotted using a polar stereographic projection. Right: same for the simulations in which the mean flow relaxation time r varies with latitude, as described in section 2.6.2. 32

2.15 Same as Figures 2.9 and 2.11 but for the barotropic experiments with H_b =200m (top), 500m (middle) and 1km (bottom). The contour interval for the flux convergence is now 6×10^{-7}ms^{-2}. 34

2.16 Same as Figure 2.3 but for u_E calculated from equation 2.6 with $c = 0$ (the 300hPa zonal wind profile used in [54]), $c = 0.4$, $c = 0.8$ and $c = 1$ (the 350hPa wind profile from the control experiment of the GCM). 35

2.17 The Plumb fluxes (arrows), critical lines (red) and $n_s = 5$ contours (green) for $H_b = 100$m and $c = 0$ (top left panel), $c = 0.4$ (top right), $c = 0.8$ (bottom left) and $c = 1$ (bottom right). When $c = 0$ u_E is the 300hPa zonal-mean wind profile from [54] and when $c = 1$ u_E is the zonal-mean wind profile at 350hPa in the control simulation of the GCM under equinoctial conditions. The scale of the arrows is the same in all panels. 36

2.18 The full vertical motion forced by the topography, F_{nl}, for the barotropic experiment when $H_b = 200$m (top) and 1km (bottom). The plots have been normalized by $H_b/1000$m and the contour interval is 250mday^{-1}, with positive contours solid and negative contours dashed. The thin dashed lines indicate the latitude of the peak orography and the thick gray lines connect the centers of vertical motion. 38

2.19 As in Figure 2.14, but for the barotropic simulations in which the shape of the vorticity forcing is kept fixed. The titles show the height of mountains which would produce the same vorticity source. 39

3.1 Vertically-integrated terms in the zonal-mean momentum budget of the control simulation. 47

3.2 The normalized mountain torque (top panel), the convergence of the normalized stationary EMF (middle panel) and the sum of these (bottom panel) for the experiments in the linear regime. The dashed lines show the results for the stationary wave model experiments. 50

3.3 The top panel shows the normalized eddy streamfunction response at 350hPa of the stationary wave model to orography with $H = 500$m while the bottom panel shows the normalized response of the full GCM with $H = 400$m. 52

3.4 Top panel: the wind vectors on the lowest σ level for the $H = 500$m experiment with the stationary wave model. Middle-panel: PF_z at 825hPa for the same experiment. Bottom panel: EP_z for the same experiment. 53

3.5 Responses of the terms in the momentum budget (equation 3.9) to mountains with $H \geq$1km. 56

3.6 The maximum stationary EMF convergence versus the maximum mountain torque for the experiments with the GCM. The straight line plots a one-to-one fit and the inset shows a close-up of the six smallest mountains ($H \leq$1km). 57

3.7 Top left panel: 300hPa zonal-mean winds in the control simulation (solid black curve), average ensemble-mean 300hPa winds for days 150-200 from the 2km transient simulations (dashed black curve) and average ensemble-mean 300hPa winds for days 150-200 from the 4km transient simulations (dashed red curve). Top right panel: zonal-mean transient EMF divergence in the control simulation. Bottom left panel: difference between the ensemble-mean transient EMF divergence averaged over the first four days for the transient simulations with $H =$ 2km and the control EMF divergence. Bottom right panel: same as the bottom left panel but for the $H = 4$km simulations. 58

3.8 Eady growth rate at 780hPa for the control experiment (top panel), the 2km experiment (middle panel) and the 4km experiment (bottom panel). Regions where the mountains intrude into this level are shaded in red. The contour interval is 0.05 days^{-1} in each panel. 61

4.1 Eddy streamfunction response at 350hPa for $Q_0 = 0.2$K/day (top left), 0.5K/day (top right), 2K/day (bottom left) and 5K/day (bottom right). The contour intervals are written on the panels, negative values are shaded and the green ovals show the $Q_0/2$ contour. The responses have been symmetrized about the equator to reduce the sampling error. 69

4.2 Eddy streamfunction response at 2°N to equatorial heating for $Q_0 =$ 0.2K/day (top left), 0.5K/day (top right), 2K/day (bottom left) and 5K/day (bottom right). The contour intervals are written on the panels. 70

4.3 Equatorial zonal-mean zonal wind as a function of Q_0. Circles show the vertical-mean wind, triangles show the wind at 250hPa, diamonds show the wind at 350hPa and squares show the wind at 850hPa. Note the logarithmic scale for the x-axis. 71

4.4 Vorticity balance for the $Q_0 = 0.2$K/day experiment. The terms are defined in equation 2.5 and the text below. 73

4.5 Root-Mean Square (RMS) of the terms in the vorticity budget at 250hPa between $-20°$ and $20°$ as a function of Q_0. Note the logarithmic scale for the x-axis. 74

4.6 Tropical static stability for the control experiment (top left) and the experiments with $Q_0 = 0.2$K/day (top right), 0.5K/day (center left), 2K/day (center right) and 4K/day (lower left). The dashed black lines show the tropopause heights in these experiments, with the tropopause defined as the pressure at which $\partial T/\partial z$ is less than 2Kkm^{-1}. Regions in which the static stability is outside the colorbar scale are shaded in gray. 75

4.7 Top panel: zonal mean temperature change (colors) and change in the zonal-mean winds (black contours, with contour interval 0.1ms^{-1} and negative contours dashed) between the $Q_0 = 0.5$K/day experiment and the control experiment. Bottom panel: change in the static stability between the 0.5K/day experiment and the control experiment (colors) and the zonal-mean stationary vertical eddy heat flux in this experiment (black contours, with contour interval 0.002 KPas^{-1} and negative contours dashed). 76

4.8 Same as Figure 4.5 but for the cases with no zonal-mean heating (top panel) and the cases with the Schneider (2004) forcing (bottom panel). 77

4.9 Vertical profile of the zonal momentum budget at the equator for the control experiment. The terms are defined in equation 4.6 and the text below. 78

4.10 Latitude-pressure cross-sections of the responses of the vertical mean (top left panel), horizontal stationary (top right panel), vertical stationary (bottom left panel) and horizontal transient (bottom right panel) terms in the zonal momentum budget for $Q_0 = 0.5$K/day. . . . 79

4.11 Responses of the vertical mean, horizontal stationary, vertical stationary and horizontal transient momentum fluxes to $Q_0 = 0.2$K/day (blue), 0.5K/day (red), 2K/day (green), 4K/day (orange) and 7.5K/day (purple). The curves have been normalized by $1/Q_0$. 81

4.12 Vertical integral of the normalized equatorial stationary horizontal EMF convergence as a function of Q_0 (circles), the integral of the transient horizontal EMF convergence (squares) and the sum of the two (diamonds). 83

4.13 Vertical-mean equatorial zonal-mean zonal wind as a function of Q_0 for Δ_y = 80K (circles), Δ_y = = 60K (triangles), Δ_y = = 40K (squares) and with the Schneider (2004) [106] set-up (diamonds). The red crosses show the experiments run with $\Delta_Y = 40$K initialized with the final state from the $Q_0 = 7.5$K/day experiment. 84

4.14 Top left panel: zonal-mean zonal wind (black contours) and eddy momentum flux divergence (colored contours) for the case with $Q_0 = 7.5\text{Kday}^{-1}$ and $\Delta_y = 40$K. The contour interval for the zonal wind is 10ms^{-1}. Top right panel panel: mean meridional circulation in the same experiment. Bottom left panel: static stability for the same experiment. Bottom right panel: terms in the vertically-integrated momentum budget at the equator for the $Q_0 = 4$K/day and $Q_0 = 7.5$K/day experiments. 85

4.15 The eddy streamfunction responses at 2°N for $Q_0 = 4$K/day (top left panel) and $Q_0 = 7.5$K/day (top right panel) with $\Delta_y = 40$K. The bottom panel shows the vertical profiles of the stationary horizontal EMF convergence in these experiments. 87

4.16 As in Figure 4.1 but for the experiments with the S04 forcing and the results have been normalized by $1/Q_0$. Note the different contour level used in the bottom right panel. 90

5.1 The left panel shows the average DJFM EMF divergence in the southern hemisphere of the MERRA data in color and the zonal-mean zonal winds in gray, with contour spacing 4 ms^{-1} and negative values dashed. Locations at which topography intrudes into more than one third of the gridpoints are shaded. The right panel shows the average DJFM EMF divergence due to eddies with wavenumbers one to five. Note the different colorbar scales. 100

5.2 Top panel: DJFM average of the divergence of the EMF co-spectra at the 300hPa level in the MERRA data. Middle panel: same but with the co-spectra only calculated using wavenumbers one to five. Bottom panel: same but with the co-spectra only calculated using wavenumbers six and higher. The solid black lines show the zonal-mean winds at 300hPa and 800hPa. Δc is 2.3 ms^{-1}. 101

5.3 Same as Figure 5.2 but for the 800hPa level in the MERRA data. Δc is 2.3 ms^{-1}. 102

5.4 Same as Figure 5.2 but for the lower layer of the two-layer QG model (left panels) and the 800hPa level in the primitive equation model (right panels). Δc is 0.06 for the QG model and 2.3 ms^{-1} for the primitive equation model. 104

5.5 Zonal wavenumber-phase speed co-spectra for the eddy momentum flux in the GCM at 48°S. Δc is 2.3 ms^{-1}. 106

5.6 Top panel: Maximum EMF convergence in the jet core as a function of wavenumber for the upper layer of the two-layer QG model (squares), the 300hPa level in the primitive equation model (circles) and the 300hPa level in the MERRA data (triangles). The values have been normalized so that the largest absolute value of the EMF convergence is one and spectra have only been calculated for the first nine wavenumbers. Middle panel: same but for the EMF divergence in the lower layer of the two-layer QG model and the 800hPa level in the primitive equation model and the MERRA data. Bottom panel: the integrated EHF as a function of wavenumber in the lower layer of the QG model and the 800hPa level in the primitive equation model and the MERRA data. 107

5.7 The lower layer EMF divergence divided by the upper layer EMF divergence in the QG model as the frictional time-scale is varied (solid line and triangles). The dashed line and squares show the same quantity but only the lower layer EMF divergence due to eddies with wavenumbers one to five is used. The red dots indicate the ratios for the control simulation. 109

5.8 Divergence of the EMF co-spectra in the upper (top panel) and lower (bottom panel) layer of the two-layer QG model for the experiment with $\tau_F = 100$ days. Δc is 0.06. 111

5.9 Probability density functions (PDFs) of the daily EMF divergence in the center of the upper (thin black lines) and lower (thin red lines) layers of the two-layer QG model. The thicker lines show Gaussian fits to the PDFs and the dashed vertical lines show the means of the distributions. 112

5.10 Contours show the eddy heat flux co-spectra in the lower layer of the two-layer QG model. The solid lines show the upper and lower layer zonal-mean zonal winds and the thick dashed line shows the lower layer PV gradient. Δc is 0.06. 114

6.1 (left) Time-averaged zonal-mean zonal wind profiles for both layers from a 10^5-day integration of the two-layer model using the parameter settings of [140] and (right) the time-averaged zonal-mean EMF and EHF. 121

6.2 *(a)* Profile of $\frac{\partial \psi_R}{\partial y}$; *(b)* the baroclinic perturbation to the zonal momentum equations applied to the two-layer model and *(c)* the resulting model response (the zonal wind tendency is inverted from the thermal forcing); *(d)* the barotropic perturbation (note: the perturbations to the upper and lower layers plot on top of each other) and *(e)* the model response. The vertical gray lines in panels *(c)* and *(e)* show the position of the $max\Delta u$ metric. 124

6.3 *(a)* The leading uncoupled EOF in each layer when $\beta = 0.2$; *(b)* the leading coupled EOF (blue) and the sixth anti-symmetric coupled EOF (red) for the same case. The lines to the left correspond to the lower layer and the lines to the right correspond to the upper layer. 127

6.4 Comparison of the time-averaged zonal-mean zonal winds as β is varied from 0.2 to 0.4. (top) The upper layer and (bottom) the lower layer. . 130

6.5 Autocorrelation of the first principal component as β is increased (5 model days $\equiv$ 1 Earth day). The inset is a close-up of lags zero to 400. 131

6.6 (left) Ensemble-mean estimates of the multivariate skewness, T_γ (top), and kurtosis, T_K (bottom), test statistics as a function of the number of included anti-symmetric EOFs for different values of β. The gray shaded regions show the 95% confidence intervals corresponding to a 10-member mean sample multivariate skewness and kurtosis, when the underlying data are Gaussian and these statistics are distributed as explained in section 6.2.4. The colored shading shows plus/minus one standard deviation divided by $\sqrt{10}$ of the estimates. (right) As in (left), but where the principal component time series are randomly disordered to remove the coupling between EOFs. 132

6.7 *(a)* Variation of $max\Delta u$ as β is increased (black circles) and the corresponding ensemble-mean FDT estimates for the upper layer using the leading EOF (blue triangles) and the first five antisymmetric EOFs (red diamonds). The shading is the plus or minus one standard deviation envelope while the straight lines represent linear least squares fits to the data. *(b)* As in *(a)*, but for the RMS error instead of $max\Delta u$. *(c)*, *(d)* As in *(a)*, *(b)*, but for the lower layer. 134

6.8 Comparison of upper-layer model responses to the barotropic perturbation for three values of β (black lines) and ensemble-mean FDT estimates using the leading coupled EOF (blue lines) in each case. The shading is plus/minus one standard deviation. 135

6.9 *(a)*, *(c)* The model response to the barotropic perturbation without eddies in black, the model responses with eddies and $\beta = 0.2$ in blue and $\beta = 0.4$ in red. P*(c)*, *(d)* As in *(a)*, *(b)*, but for the baroclinic perturbation. 136

6.10 The cumulative variance explained by the anti-symmetric EOFs for three values of β. The horizontal black lines mark the 95% line while the vertical black lines denote the first EOF which was not well separated. 137

6.11 *(a)* FDT estimate of the value of $max\Delta u$ in the upper layer using the leading coupled EOF for the case $\beta = 0.4$ as a function of the upper integration limit, T. The blue dots show the ensemble-mean while the shading is plus/minus one standard deviation. The horizontal dashed line shows the value of $max\Delta u$ for the model response. *(b)* is the same but using the first five anti-symmetric coupled EOFs in the FDT calculations and *(c)* shows this for the $\beta = 0.35$ case also using five EOFs. 140

6.12 As in Figure 6.9 but the FDT estimates used the first five antisymmetric coupled EOFs. 141

6.13 *(a)*, *(c)*, *(e)* as in Figure 6.12 but the no-eddy response has been subtracted from every curve. *(b)*, *(d)*, *(f)* The model response of the upper layer potential vorticity flux in black and the corresponding FDT estimates in blue. 144

6.14 Ensemble-mean FDT estimates for the model's response to the baroclinic perturbation in the case $\beta = 0.2$. *(a)*, *(c)* The results using the first five coupled anti-symmetric EOFs. *(b)*, *(d)* The results using the first six coupled anti-symmetric EOFs. The color scheme is the same as in Figure 6.8 and the top panels show the upper layer while the lower panels show the lower layer. 145

6.15 Ensemble-mean FDT estimates for the upper layer model responses to the barotropic perturbation using the leading barotropic and baroclinic EOFs for three values of β. The color scheme is the same as in Figure 6.8. 146

6.16 As in Figure 6.15 but for the baroclinic perturbation. 147

6.17 As in Figure 6.16 but the FDT estimates use a new basis with the leading EOF having the form of the baroclinic perturbation and are calculated using the whole time-series rather than an ensemble (hence there are no estimates of the sampling error). The lower layer results are similar. 149

Chapter 1

Introduction

Studying the large-scale structure and circulation of the troposphere gives us our most basic understanding of Earth's surface climate and weather. Simple energy balance models can be used to explain why Earth's global-mean surface temperature is about 15°C, but the general circulation of the troposphere controls the distributions of temperature, wind and precipitation on Earth. The general circulation also determines the variability of regional climates and drives the circulation of the oceans. Looking to the future, predictions of how human activities will be impacted by climate change must be based in large part on predictions of how the tropospheric circulation will respond to the heating due to increased carbon dioxide concentrations.

This thesis seeks to improve our understanding of the general circulation by studying the transport of angular momentum in dry atmospheres. The usefulness of angular momentum transport as a starting point for understanding the circulation of the troposphere is now well established [42]; while eliminating moisture is a natural first step when developing theories in atmospheric dynamics, as moist processes can be added later as corrections or modifications to dry theories. My focus has been specifically on the transport of zonal-mean momentum by tropospheric eddies. A complete theory for the general circulation would consist largely of theories for the eddy momentum

fluxes (EMFs) and the eddy heat fluxes (EHFs), in other words for the eddy potential vorticity (PV) fluxes. The EHF is often thought of as a diffusive process [41] and so the central task is to develop an understanding of what sets the diffusivity. In contrast, the EMFs are determined by the complex interplay between eddies and the mean flow, and much of the thesis is focused on understanding the propagation of eddies and how this relates to the mean flow.

The eddies which transport heat and momentum in the troposphere challenge our intuition. They are often called "Rossby" waves[1], and their restoring force is the meridional rotation gradient arising from Earth's spherical geometry and rotation about its axis. This causes their behavior to differ in important ways from that of more familiar waves, such as surface waves driven by wind blowing over water. There is a large body of literature devoted to studying Rossby waves; from the perspective of this thesis their most important property is that they transport (zonal-mean) momentum in the opposite (meridional) direction to that in which they propagate. In other words, they accelerate the flow where they form and decelerate the flow where they break. Their source is typically a baroclinic jet in mid-latitudes, which they help to sustain, while they break near "critical" latitudes where their phase speeds approach the zonal-mean wind speed[2].

This property of Rossby waves plays a fundamental role in atmospheric dynamics. For instance, experiments with comprehensive climate models suggest that the mid-latitude jets in each hemisphere will shift polewards in the future as a result of climate change (e.g., [130]; [12]; [60]). A number of possible mechanisms have been proposed for why this might happen, but the essence of all of these is a meridional shift of either the source of the waves or of the regions where the waves break. Untangling these mechanisms remains an open question and Chapter 6 touches on this issue.

[1] I will use the terms "eddies" and "waves" interchangeably

[2] Chapter 5 considers a situation in which Rossby waves transfer momentum in the same direction as their group velocity, which occurs when the zonal-mean PV gradient along which the waves propagate is negative

The breaking of Rossby waves in the subtropics also helps determine the strength and extent of the tropical Hadley circulation. The steady-state zonal momentum budget in the upper troposphere can be written as [131]

$$f\bar{v}(1 - Ro_L) \approx -\frac{\partial}{\partial y} EMF, \tag{1.1}$$

where f is the Coriolis parameter, $\bar{v}$ is the zonal-mean meridional flow in the upper troposphere and Ro_L is the "local" Rossby number ($= -\bar{\zeta}/f$, where $\bar{\zeta}$ is the zonal-mean relative vorticity). In the angular momentum conserving limit $Ro_L \sim 1$ and v is essentially independent of the EMF divergence by the eddies. However, if Ro_L is small, as is the case much of the time on Earth [107], then the EMF divergence in the subtropics is the main control on the Hadley circulation. Both observations and models indicate that there is a connection between the positions of the mid-latitude jets and the extent of the Hadley circulation ([58]; [15]; [119]), and so it seems likely that future changes in these will be related, making it difficult to untangle the underlying causes.

With this background, the first half of the thesis considers how the EMFs due to stationary waves impact the momentum budget of the atmosphere, while the second half focuses on the relationship between transient EMFs and mid-latitude jets. This division reflects the fact that theories for the zonally-symmetric and zonally-asymmetric components of the general circulation can effectively be developed independently of one another.

The most prominent feature of the zonally asymmetric circulation is the planetary-scale, quasi-stationary waves that are excited by orographic and thermal forcing (Figure 1.1). These waves transport heat and moisture locally, exerting a strong control on regional climates, while the stationary EMFs due to these waves make up a substantial term in the atmosphere's zonal-mean momentum budget.

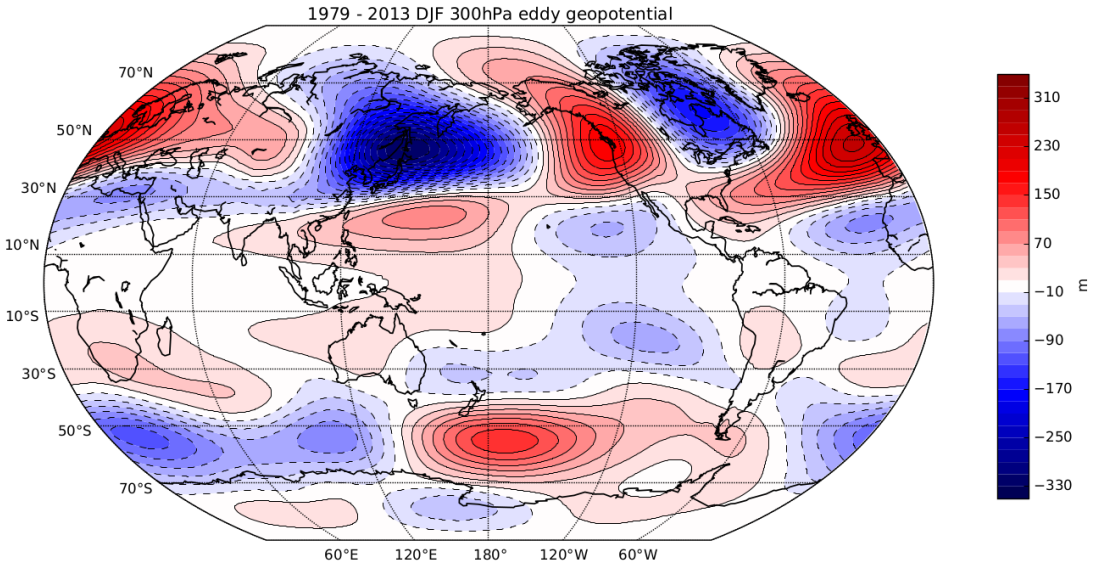


Figure 1.1: Climatological December-January-February (DJF) deviations from the zonal-mean ("eddy") geopotential height at 300hPa for 1979 to 2013 from the ERA-Interim reanalysis dataset [23]. The large-scale waves seen in the Northern Hemisphere are a superposition of quasi-stationary Rossby waves forced by orography and by heating.

Our theoretical understanding of stationary waves is based on linear dynamics, which has provided good qualitative agreement with observations. However, connecting this theory quantitatively to observations involves a number of intermediate steps, including experiments with stationary wave models and with fully turbulent general circulation models (GCMs). Chapters 2, 3 and 4 fill in some of these steps by investigating the linear response of an idealized GCM to forcings that mimic the Tibetan plateau (Chapters 2 and 3) and the heating in the west Pacific during El Nino events (Chapter 4). These are the two dominant sources of quasi-stationary waves in Northern Hemisphere winter [49]. In both cases, the strength of the forcing is varied in a search for a parameter regime in which the model's response is linear in the strength of the forcing, and then the strength of the forcing is increased in order to investigate the breakdown of the linear response and also the consequences for the zonal-mean momentum budget of the transition to non-linearity.

In the case of orographic forcing a surprising transition is seen from a wave that mostly propagates zonally in the linear regime to a wave that mostly propagates meridionally in the non-linear regime. This contrasts with the intuition developed by Hoskins and Karoly (1981) [54], among others, that stationary waves propagate along great circles. Instead, the stationary waves of the linear regime are trapped in the mid-latitude jet and correspond to the "circumglobal" waves first described by Branstator (2002) [9]. Chapter 2 explores this linear regime and also attempts to understand why the waves are no longer trapped by the waveguide in the non-linear regime. The implications of the transition from zonal to meridional propagation for the momentum budget of the GCM are then investigated in Chapter 3.

The model's response to equatorial heating is discussed in Chapter 4. The theory for the tropical atmosphere's response to heating was developed by Matsuno and Gill, based on the dynamics of a linear shallow water layer ([79]; [34]). The so-called Matsuno-Gill model has since proven to be a useful conceptual framework for understanding a wide range of tropical phenomena, including the atmosphere's response to El Nino, the Madden-Julian Oscillation and the atmospheres of tidally-locked exoplanets. The GCM's response to small heatings also resembles the response of the Matsuno-Gill model, but for larger heatings the equatorial winds accelerate and superrotate (they have greater angular momentum than the surface), breaking the assumption of the linear model that the tropical atmosphere is quiescent. This superrotation is driven by the EMFs due to the stationary waves excited by the heating, and much of the chapter is devoted to investigating the relationship between the stationary wave response and the superrotation.

Some of the key features of the transient EMFs are illustrated by Figure 1.2, which shows the total cloud cover on January 14th 2010 as measured by the Clouds and the Earth's Radiant Energy System (CERES) experiment. The regions of high cloud cover tilting southwest-northeast in the Northern Hemisphere and northwest-

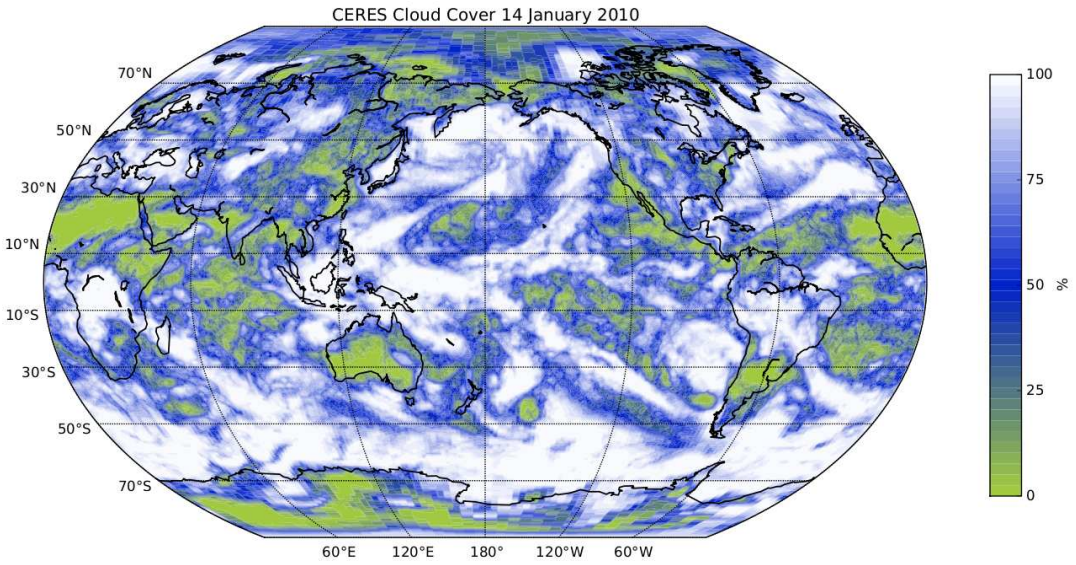


Figure 1.2: Total cloud cover on January 14th 2010 as measured by the Clouds and the Earth's Radiant Energy System (CERES) experiment.

southeast in the Southern Hemisphere are transient baroclinic eddies propagating towards the equator. These waves flux momentum into the mid-latitude jets, which are located further poleward at about 45° in each hemisphere, and, primarily because of Earth's geometry, are more prominent than the waves poleward of the jets, which tilt in the opposite direction. For this reason the transient EMFs are larger on the equatorward flanks of the jets than on the jets' poleward flanks.

Chapters 5 and 6 address two aspects of how transient EMFs influence mid-latitude jets. In Chapter 5 the transient EMFs in the lower tropospheres of a two-layer quasi-geostrophic (QG) model, of the GCM and of a reanalysis dataset are investigated. On Earth the EMFs are much larger in the upper troposphere than in the lower troposphere and so there has been little study of lower tropospheric EMFs, though some recent studies have hinted there they might have an interesting structure ([85]; [86]). Furthermore, lower tropospheric EMFs appear to be more prominent in a number of planetary contexts, including atmospheres with weak surface friction, such as Jupiter's [16]; in atmospheres with multiple jets in each hemisphere [62]; and in

superrotating atmospheres [104]. In these systems lower tropospheric EMFs play a much larger role in controlling the properties of the eddy-driven jets. In Chapter 5 it is shown that the behavior of the lower tropospheric EMFs is similar in both models and in the reanalysis data, and so the dynamics of the QG model can be used to interpret their structure.

Finally, Chapter 6 addresses the question of jet shifts by testing whether the Fluctuation-Dissipation Theorem (FDT) can predict how the jet in the QG model shifts in response to two different perturbations, essentially acting as a closure for the EMFs which determine the model's responses. The motivation for doing this is two-fold. First, a number of recent modeling studies have shown that the amplitude of the mid-latitude response to external forcings is proportional to the time-scale of the jets' internal variability (e.g., [33], [97] and [12]). Second, while the QG system is able to capture the essential dynamics of mid-latitude jets, it is also simple enough that sensitivity tests can be conducted and the causes of discrepancies between the model results and the FDT predictions can be investigated. This contrasts with previous FDT studies that have either considered highly idealized systems, in which the FDT can be shown to hold exactly (e.g., [73]), or have applied the FDT to comprehensive climate models, in which reasons for the success or failure of the FDT are opaque and in which the robustness of the results is questionable ([35]; [21]). Building on the work in this chapter, other authors have recently discussed alternative reasons for the failure of the FDT to make quantitatively accurate predictions, in addition to the reasons discussed here [37].

Chapter 2 is published as Lutsko and Held (2016) [71] and Chapter 6 is published as Lutsko, Held and Zurita-Gotor (2015) [72]. Chapter 5 has recently been submitted for publication with Isaac Held, Pablo Zurita-Gotor and Amanda O'Rourke as co-authors.

Chapter 2

The Response of an Idealized Atmosphere to Orographic Forcing: Zonal vs Meridional Propagation

2.1 Introduction

The response of the atmosphere to orography is one of the oldest problems in atmospheric dynamics. In one of the earliest studies, Charney and Eliassen (1949) addressed the problem in a barotropic quasi-geostrophic model in a β-plane channel, linearized about a uniform zonal-mean flow comparable to that in northern hemisphere wintertime [18]. Many subsequent studies continued to use quasi-geostrophic models on a β-plane in a channel geometry to simulate both orographic and thermally forced waves, reducing the problem to variations in longitude, x, or to variations in the x-z plane ([116]; [102]; [103]; [59]; [26]; [27]; [127]; [22]; [126]). In this channel geometry, in which only zonal and vertical propagation are allowed, resonances appear generically. Therefore, the impression emerged that the atmosphere's response to orography is highly sensitive to changes in parameters such as the zonal-mean flow

and the frictional time-scale. These resonances can in some cases also lead to the existence of multiple equilibrium states when the coupling to the mean flow is included ([19]).

A series of papers by Hoskins and co-authors dramatically changed this intuition in the late 70s and early 80s ([52]; [36]; [54]). These works emphasized the importance for stationary Rossby waves of meridional as well as zonal propagation; in the special case of a zonal-mean zonal flow that is proportional to the cosine of the latitude ray tracing using the barotropic dispersion relationship shows that stationary waves exactly follow great circles ([54]). Ray tracing on more realistic zonal flows typically retains some of this great circle flavor.

The realization that the meridional motion of Rossby waves is just as important as their zonal motion led to a focus on the fate of stationary Rossby waves as they propagate into the tropics ([61]; [47]; [28]). While nonlinear critical layer theory reveals the potential for reflection of these waves back towards midlatitudes, the fact that the climatological stationary eddy momentum flux is directed from the tropics towards midlatitudes indicates that on average these waves are preferentially absorbed rather than reflected. The study of resonances and multiple equilibria in idealized model configurations continued ([56]; [57]; [51]; [75]; [55]), but as Kallen (1985) emphasized, the meridional propagation of Rossby waves into the tropics and the existence of absorption there makes it much harder for resonances to exist, and hence multiple equilibria and the associated sensitivity to the mean flow [57]. While the reflection of Rossby waves by a critical layer has been seen in General Circulation Models (GCMs, [132]), it seems difficult to create enough reflection from the tropics, in the presence of mixing by large-scale transients and of the Hadley cell, that a wave would be able to propagate around the entire globe.

However, in a parallel series of papers it was noticed that mid-latitude jets can act as waveguides for Rossby waves generated by idealized vorticity sources ([8]; [53]; [9]),

resulting in the waves propagating over long zonal distances with little meridional motion. Branstator (2002) coined the term "circumglobal waves" to describe this phenomenon [9], and circumglobal waves have been seen in observations as well as in GCMs and barotropic models ([9]; [7]; [10]; [77]; [90]; [101]). To lowest order, they can be thought of as edge waves propagating along the sharp potential vorticity gradient at the center of a westerly jet. These waves may also play an important role in the response of the stationary wave field to climate change ([109]; [7]; [90]). Using a linear barotropic model, Manola et al. (2013) found that the effectiveness of a waveguide at trapping these circumglobal waves is sensitive to changes in the zonal-mean flow [77].

In this chapter a connection is made between circumglobal waves and the atmosphere's response to orography. Specifically, it is found that in an idealized, dry GCM the response to a small Gaussian mountain resembles a circumglobal wave. The original motivation for carrying out these simulations was to revisit the problem of finding a regime in which the atmosphere's response is a linear function of the height of the orography. If such a regime exists then a link can be made between linear stationary wave models (e.g., [124]) and GCMs, and the breakdown of the linear response as the mountain height is increased can also be investigated. This problem was previously studied in a low-resolution (R15), moist GCM by Cook and Held (1992), who varied the height of idealized Gaussian topography from 700m to 4km and found a "near-linear" regime between 700m and 2km [20]. Here I have extended the range of heights from 250m to 5km and use a dry GCM with T42 and T85 resolutions, in which the climate is zonally symmetric in the absence of the orographic perturbations. (The orography has a half width of 15° latitude and longitude; despite this large size the localized orography is a referred to as a "mountain" in the following.)

It is found that for small enough mountains the response is linear, with the spatial structure independent of the height of the mountain, the amplitude of the response

proportional to the height and the mountain torque on the surface quadratic in the height. In the control set-up this linear response is dominated by a circumglobal wave and so the response is potentially sensitive to the mean-flow. The possibility of resonances is also reintroduced, although in the experiments presented here the forced wave loses amplitude too rapidly to create significant constructive or destructive interference. However, the circumglobal wave co-exists with a meridionally propagating wave and in the nonlinear regime the meridional wave increasingly dominates the response. In addition to the different horizontal directions of propagation these waves have noticeably different vertical structures close to the mountain. In the next chapter the implications of this transition for the zonal-mean momentum budget of the model are investigated.

I also modify the GCM, changing the equilibrium temperature structure by adding asymmetry across the equator to create a cooler and a warmer hemisphere. Topography is then added in the cooler hemisphere to examine the robustness of the zonal propagation in the linear regime.

To better understand the GCM's behavior I have sought the simplest model which can be used as an analogue for the GCM. A barotropic model on a sphere can qualitatively reproduce the linear response in the control setting, but not in the case with hemispheric asymmetry in the equilibrium temperatures. In the latter case the GCM's linear response is not trapped but the barotropic model continues to predict trapping. Consistently, the barotropic index of refraction continues to suggest the potential for trapping. The barotropic model does simulate a transition from zonal to meridional propagation as the topographic amplitude is increased, but the underlying dynamics in the two models appear to be substantially different.

In the following section the GCM model and experiments are described, before the GCM results are presented in sections 2.3 and 2.4. The barotropic model is described in section 2.5, where it is used to understand the linear response of the GCM and also

compared with the index of refraction. In section 2.6 the nonlinear response of the barotropic model is compared with the GCM's nonlinear response before the chapter ends with conclusions in section 2.7.

2.2 Primitive Equation Model and Experiments

The primitive equation simulations were carried out using the GFDL spectral dynamical core forced by zonally symmetric Newtonian relaxation to a prescribed equilibrium temperature field and damped by Rayleigh friction near the surface. The parameter settings are the standard Held and Suarez (1994) [48] parameters with forcing symmetric about the equator. This set-up produces an equinoctial climate similar to that of the real atmosphere, though the north-south temperature gradient is somewhat larger than observed and temperature is constant in the stratosphere.

The model was run at T42 resolution with 30 evenly spaced sigma levels and data was sampled once per day. The control simulation consisted of a 40 000 day integration, with the first 2000 days discarded to ensure the model had spun-up. The qualitative character of the transition from zonal to meridional propagation has been confirmed at T85 resolution (section 2.3.2). While there are undoubtedly some quantitative differences, and integrations with higher horizontal and vertical resolutions are certainly possible, the focus here is on generating long enough integrations to isolate the linear regime within this particular model.

To perturb the model Gaussian mountains were added, of the form

$$h(\phi,\lambda) = H \exp\left\{-\left[\frac{(\phi-\phi_0)^2}{\alpha^2} + \frac{(\lambda-\lambda_0)^2}{\beta^2}\right]\right\} \tag{2.1}$$

where H is the maximum height of the mountain in meters; ϕ and λ are latitude and longitude, respectively; and α and β are half-widths, both set to 15° in the initial

perturbation experiments. λ_0 and ϕ_0 were set to 90°E and 45°N, respectively. This is the same form as the mountains used by Cook and Held [20].

H was varied from 250m to 5000m. For heights less than 250m the responses were not clearly separable from the noise. Cases with H less than 1km were run for 40 000 days and the responses were obtained by discarding the first 2000 days of each perturbation experiment and averaging over the rest of the integration. Cases with larger mountains equilibrated more quickly and so were only run for 20 000 days. The length of all T85 simulations was 20 000 days.

For ease of presentation, I will focus on latitude/longitude cross-sections of the eddy streamfunction responses at 350hPa and pressure/longitude cross-sections of the eddy zonal wind responses at 46°N. However, the important features and trends can be seen at other latitudes and pressures, and using other fields.

2.3 Primitive Equation Model Results

2.3.1 The small mountains

I begin by considering the cases with $H < 1$km. The eddy streamfunction responses at 350hPa for each of these experiments are shown in Figure 2.1 and the eddy zonal wind responses at 46°N are shown in Figure 2.2. In both figures the fields have been multiplied by $1000m/H$ and I refer to these as normalized responses in the following.

In the latitude/longitude cross-sections the responses are very similar in all cases and the normalization shows that the responses also have roughly the same magnitude. For each mountain the strongest response is the low directly to the southeast of the mountain and then consists of a wavenumber five zonal wave which extends east almost around the entire latitude circle. There is also a weak high in the response on the northwest flank of the mountain. Similarly, the responses closely resemble each other in the vertical cross-sections, consisting of an equivalent barotropic wave

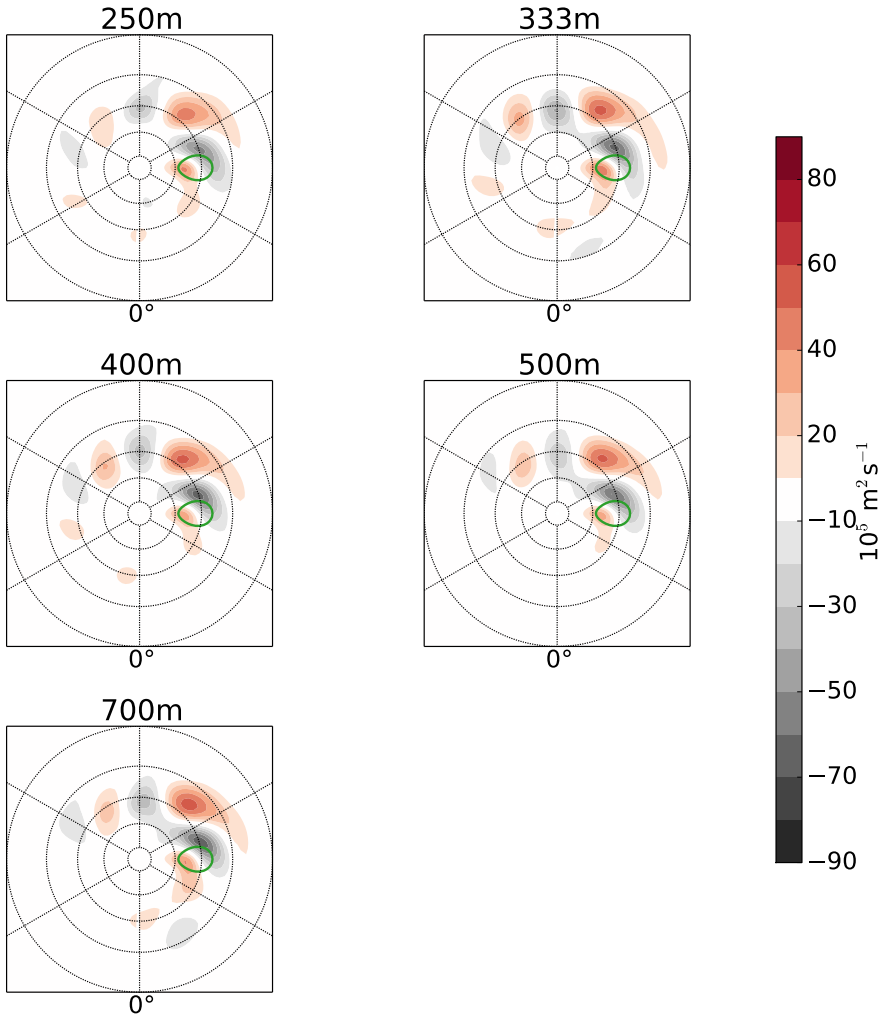


Figure 2.1: Latitude/longitude cross-sections taken at 350hPa of the eddy stream-function response of the primitive equation model to idealized topography with $H =$ 250m (top left), $H =$ 333m (top right), $H =$ 400m (center left), $H =$ 500m (center right) and $H =$ 700m (bottom left). The responses have been normalized by 1000m $/H$ and the data is plotted using a polar stereographic projection. The green ovals show the H / 2 contour.

centered near 300hPa with wavenumber five. The response is strongest directly to the east of the mountain and then the external Rossby wave weakens gradually as it extends around the entire globe.

The zonal waves seen here resemble the "circumglobal" waves described by Branstator (2002) [9], which suggests that the stationary wave produced by the

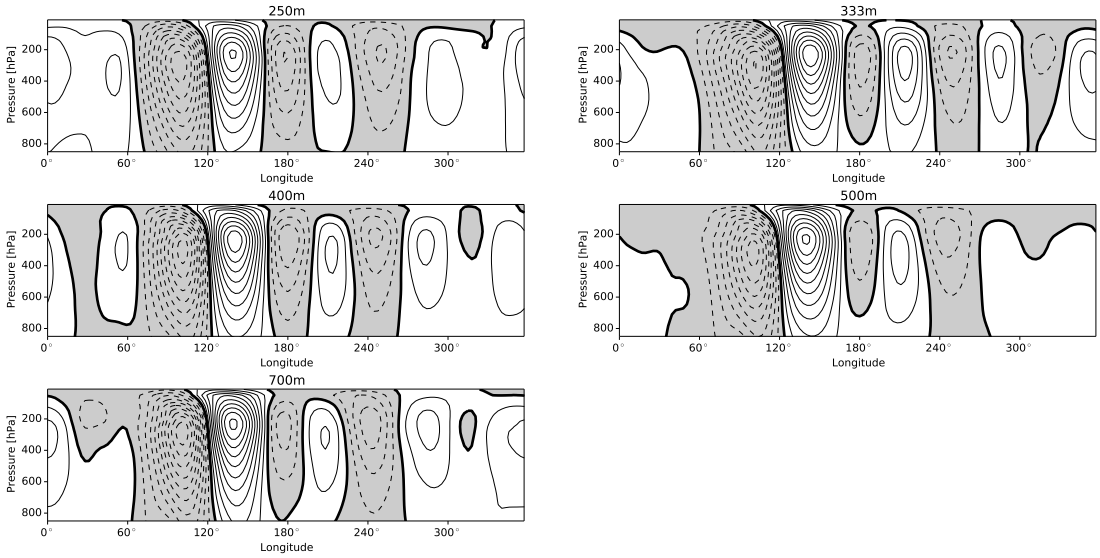


Figure 2.2: Pressure/longitude cross-sections taken at 46° latitude of the eddy zonal wind response of the primitive equation model to idealized topography with $H =$ 250m (top left), $H = 333$m (top right), $H = 400$m (center left), $H = 500$m (center right) and $H = 700$m (bottom left). The contour interval is 0.5 ms^{-1}, the zero contour is shown by a thicker line and areas of negative winds are shaded in gray. The responses have been normalized by 1000m $/H$.

orography is being trapped by the jet. If the flow is sufficiently slowly varying, an index of refraction can be used to determine whether a waveguide exists that can trap stationary external Rossby waves. There are a number of reasons why this diagnostic may not be quantitatively useful, beginning with the fact that the flow may not be sufficiently slowly varying, but it is safe to assume that a waveguide in the index of refraction (a region of propagation surrounded by regions of evanescence) is a necessary condition for the trapping of stationary waves. Therefore, the index of refraction indicates the "potential" for trapping. One can also have a situation in which temporal variations in the flow smooth the long term mean potential vorticity field, reducing the potential for trapping that exists over shorter time averages. But once again one can still hope for qualitative guidance from the index of refraction regarding the potential for trapping.

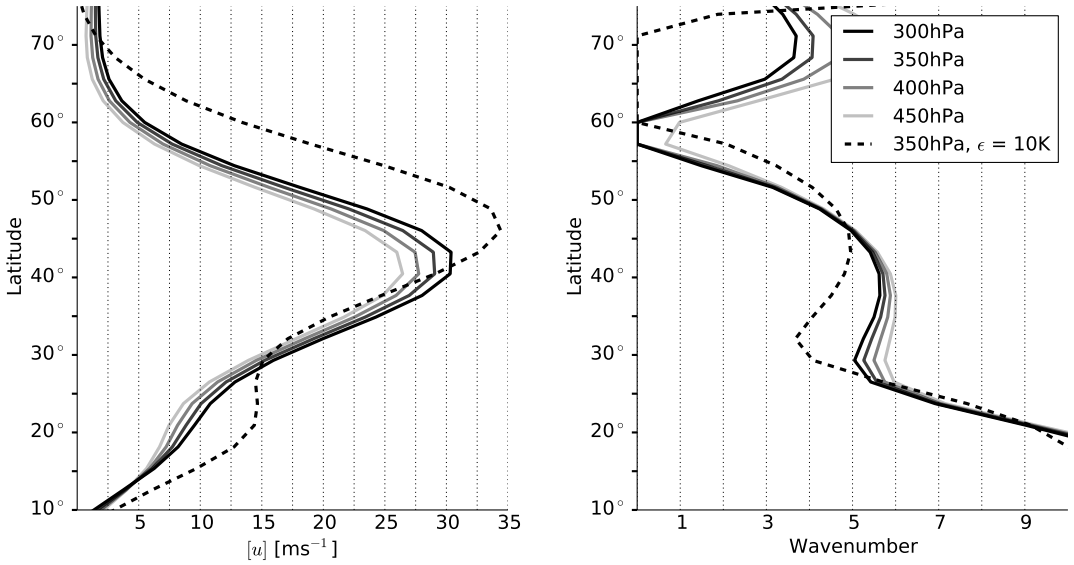


Figure 2.3: Left: the time-averaged zonal-mean zonal wind profile from a control simulation of the primitive equation model at 300hPa, 350hPa, 400hPa and 450hPa (solid lines) and the zonal wind profile at 350hPa from an unperturbed experiment with $\epsilon = 10$K (dashed). Right: the profiles of the index of refraction n_s^2 for each of these. Zonal wavenumbers to the left of the curves are able to propagate while those to the right are evanescent.

By transforming to Mercator co-ordinates the index of refraction, n_s^2, for barotropic waves can be defined as [54]

$$n_s^2 = a\left\{cos^2\phi\left(\beta + \frac{1}{a}\frac{\partial[\zeta]}{\partial\phi}\right)/[u]\right\}, \tag{2.2}$$

where a is the Earth's radius, ζ is the relative vorticity, u is the zonal wind and square brackets indicate zonal averages. For baroclinic models Held et al. (1985) [45] showed that there is a meridionally-varying pressure, $p_e(\phi)$, at which external Rossby waves obey the dispersion relation of barotropic waves; hence the correct $[u]$ to use in equation 2.2 is $[u(p_e)]$. Held et al. found that for northern hemisphere winter conditions p_e is between 450 and 400hPa and so rather than calculate p_e explicitly, in Figure 2.3 I simply show the time-averaged zonal-mean zonal winds from the control

simulation for a range of pressures near 400hPa as well as the corresponding profiles of n_s^2. In the time-mean wavenumber five waves are trapped at 300hPa, though at other levels the jet is also close to being a waveguide, and so this index of refraction suggests that trapping is plausible, possibly with non-negligible leakage.

Indeed, even at these small mountain heights there is some leakage from the waveguide in the form of meridional propagation that seems to begin farthest downstream at the smallest values of H and then progressively becomes apparent closer to the mountain as H increases. The leakage or damping is sufficient in these cases that the amplitude is reduced to small values before returning to the forced region.

2.3.2 The large mountains

The responses for the rest of the mountains are shown in Figure 2.4, which plots the normalized eddy streamfunction responses to the larger mountains at 350hPa; Figure 2.5, which shows the un-normalized eddy streamfunction response for $H =$ 4km and 5km; and in Figure 2.6 which shows the un-normalized eddy zonal velocity responses to the largest mountains at 46°.

For $H =$ 1km the response resembles those of the smaller cases but close to the mountain the wave propagates more strongly into the tropics, while also becoming dominated by a smaller zonal wavenumber. There is still some evidence of the zonal wave further from the mountain, while the anti-cyclone on the northern flank of the mountain becomes relatively stronger. As H is further increased the zonal wave continues to become relatively weaker and the response east of the mountain is then dominated by a wave which propagates meridionally into the subtropics. Note, however, that the circumglobal wave is still present in these simulations; it is just much weaker than the meridional wave, as can be seen from Figure 2.5. To the west of the mountain the anti-cyclone continues to strengthen and move closer to the center of the mountain; for $H =$ 5km it is almost directly over the mountain (bottom panel of

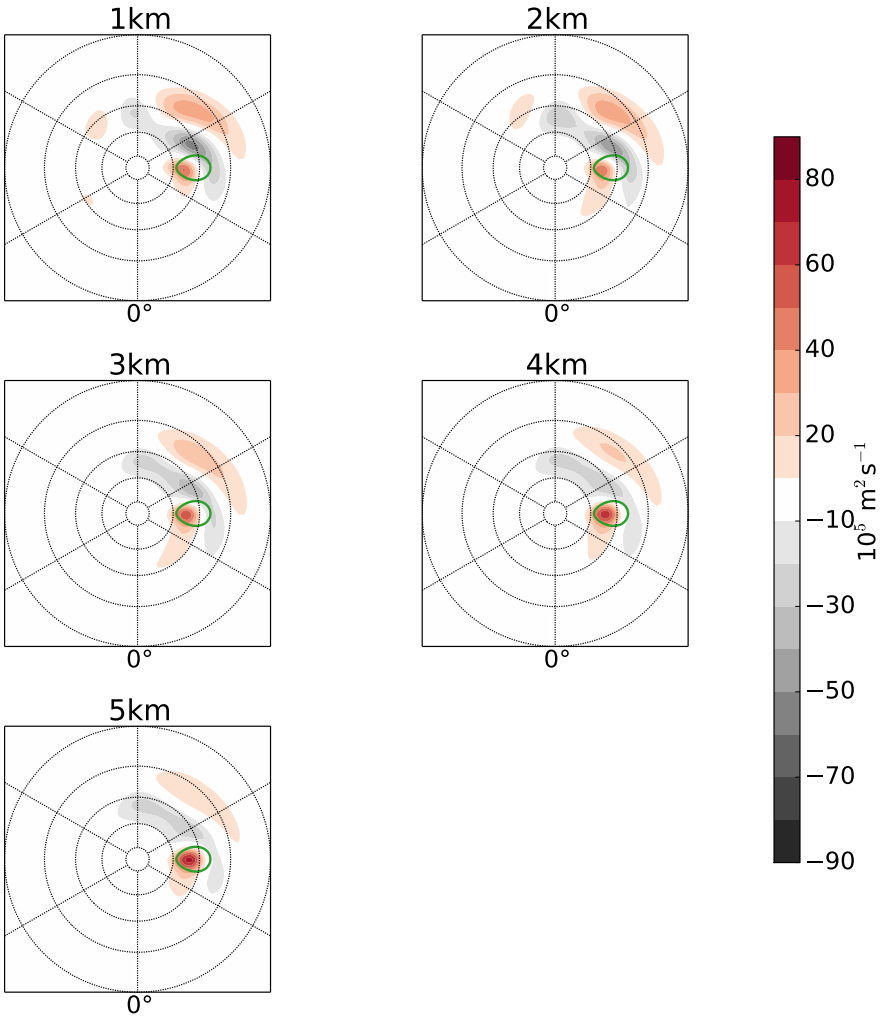


Figure 2.4: As in Figure 2.1 but for H = 1km (top left), H = 2km (top right), H = 3km (center left), H = 4km (center right) and H = 5km (bottom left). The responses have again been normalized by 1000m $/H$ and the same color scale is used.

Figure 2.5). In this respect the response in the vicinity of the mountain for large H resembles the linear f-plane response.

Consistently, in the vertical cross-sections the strong negative zonal wind anomaly over the east flank of the mountain broadens to the west as H is increased so that for H = 5km it is centered directly over the mountain (Figure 2.6). Conversely, the positive wind anomaly east of this weakens significantly relative to the negative anomaly and

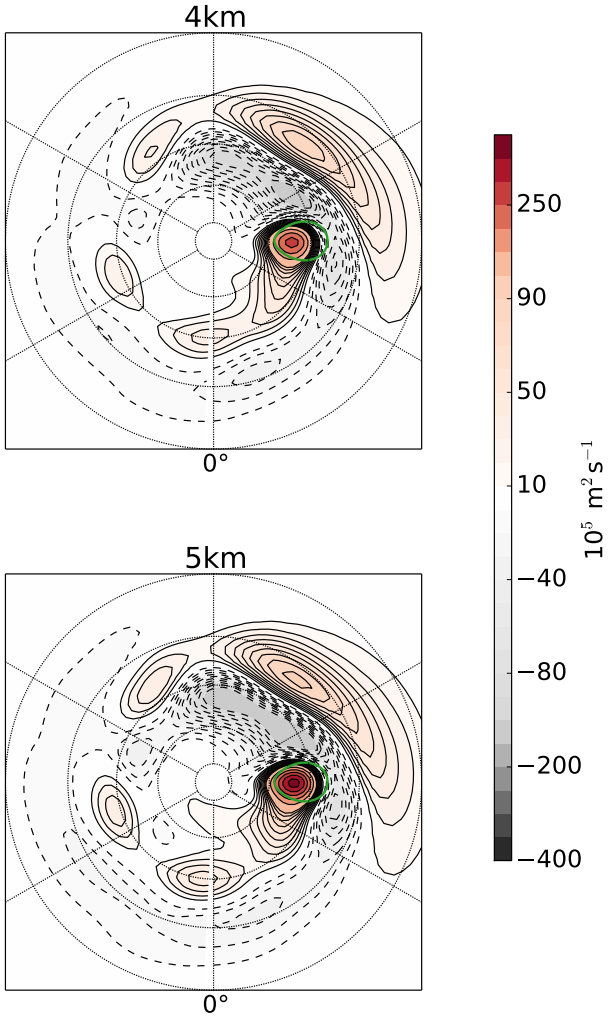


Figure 2.5: The un-normalized eddy streamfunction responses at 350hPa for H = 4km (top) and H = 5km (bottom). The contour interval is 10 m^{2}s^{-1} between -100 and 100m^{2}s^{-1} and then the interval is 50 m^{2}s^{-1} between $\pm$100 and $\pm$400m^{2}s^{-1}. Black contours have been added for clarity.

shifts upwards as H is increased. Away from the mountain the wavenumber five external wave continues to be present even in the cases with the largest mountains.

Finally, Figure 2.7 plots the normalized eddy streamfunction responses at 350hPa for H = 333m, H = 700m and H = 4km in simulations at T85 resolution, demonstrating that the results are robust to doubling the horizontal resolution of the model.

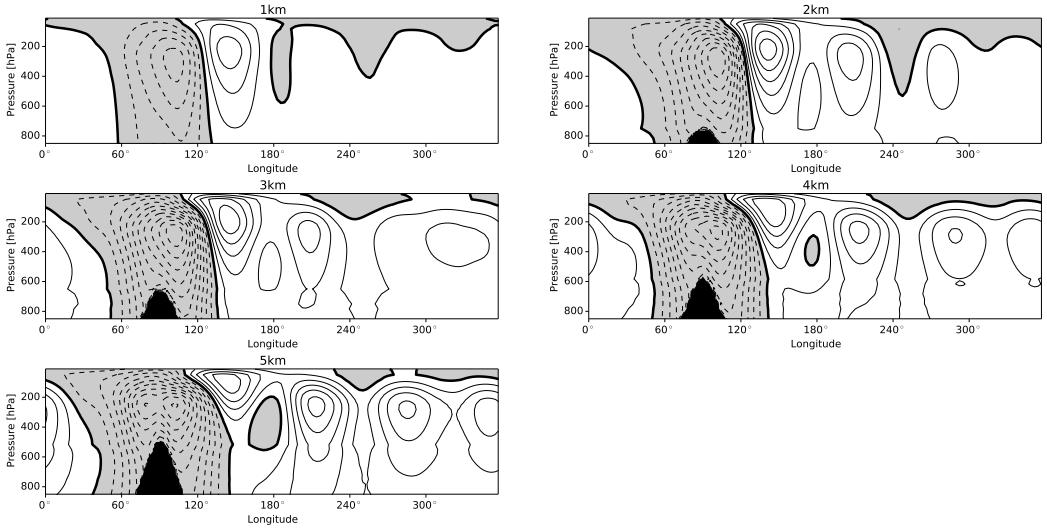


Figure 2.6: As in Figure 2.2 but for H = 1km (top left), H = 2km (top right), H = 3km (center left), H = 4km (center right) and H = 5km (bottom left), and the responses have not been normalized. The contour interval is 1 ms^{-1}, the zero contour is shown by a thicker line and areas of negative winds are shaded in gray. Where visible the mountains are shaded in black.

2.3.3 Mountain torque

Another metric which can be used to assess the linearity of the response to orography is the eastward torque exerted by the mountain on the atmosphere, which according to linear theory should be proportional to H^2. Figure 2.8 shows the normalized zonally-averaged mountain torque per degree latitude which the surface exerts on the atmosphere

$$T = -a^2 cos\phi \left[\overline{p_s \frac{\partial h}{\partial \lambda}}\right] \times \frac{H_{ref}^2}{H^2}, \tag{2.3}$$

where a is the Earth's radius, p_s is the surface pressure, H_{ref} = 1000m, the square brackets denote that this is a zonal mean and the overbar indicates a time-averaged quantity. As a crude measure of the sampling error the shading envelopes the region between T calculated using the first and second halves of the simulation. (The sampling error is very small for $H \geq$ 1km.)

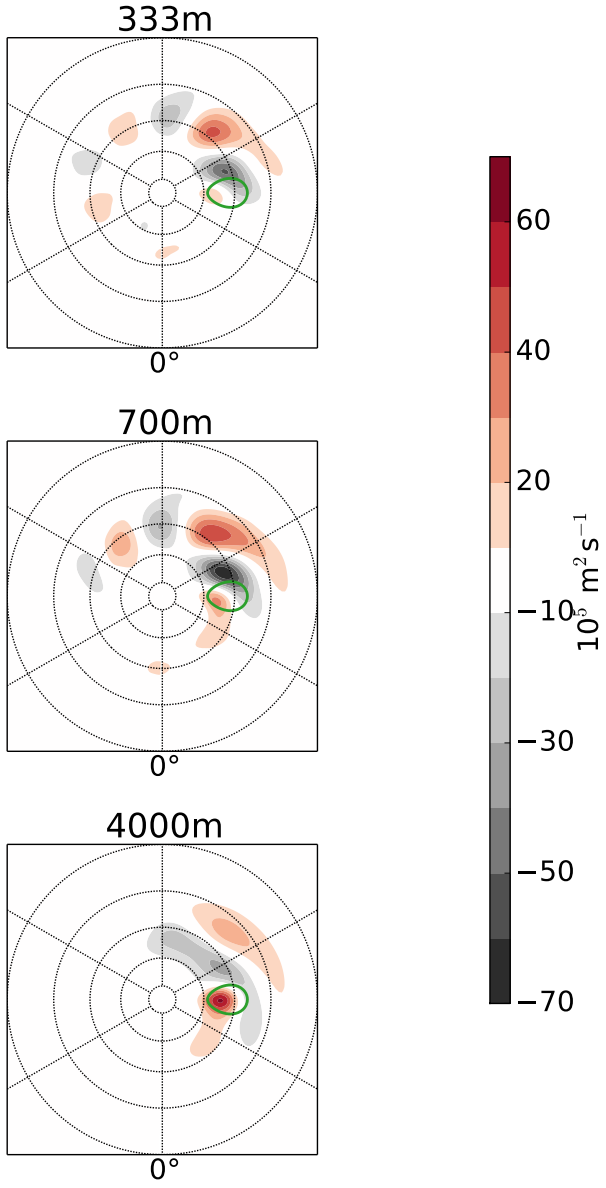


Figure 2.7: The normalized eddy streamfunction responses at 350hPa to mountains with $H = 333$m (top), 700m (middle) and 4km (bottom) from simulations run at T85 resolution.

For $H \leq 1$km the normalized torques are similar to each other, with a strong minimum over the mountain and then a weaker maximum near 54°N. In other words, the flow is decelerated over most of the mountain, and weakly accelerated over the mountain's northern edge. For $H = 2$km the negative torque on the atmosphere over the mountain is still close to the linear limit but the small positive torque to the

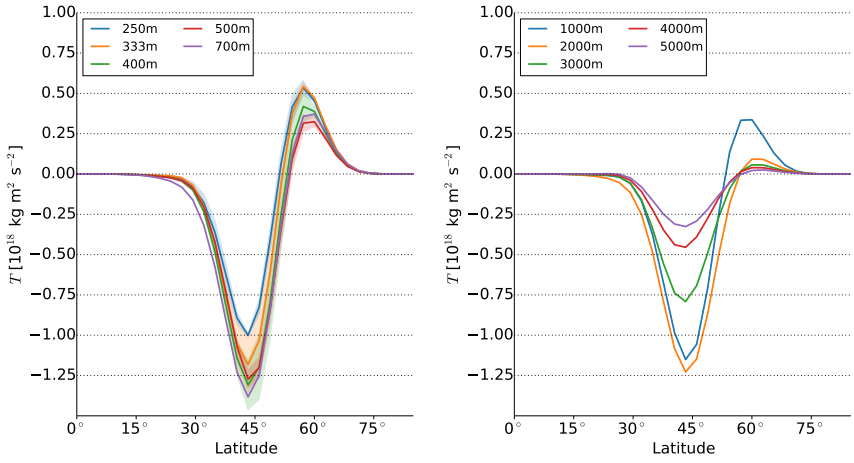


Figure 2.8: The normalized zonally-averaged mountain torque per degree latitude T for the primitive equation experiments with $H < 1$km (left) and with $H \geq 1$km (right). For each curve the shading envelopes the region between T calculated using the first half of the simulation and T calculated using the second half of the simulation.

north is roughly a quarter as large as for the smaller cases after normalization and is also shifted further north by about 7°. So using the mountain torque as a metric of linearity in the vicinity of the mountain indicates that the transition from linear to nonlinear takes place between 1km and 2km although, as discussed earlier, the departures from the linear limit are substantial downstream of the mountain by $H = 1$km. As H is increased from 2km the normalized torques continue to weaken but retain the same shape. This reduction in the normalized torque corresponds to the gradual movement of the high pressure region over the mountain, which results in p_s and $\frac{\partial h}{\partial \lambda}$ moving out of phase.

2.3.4 Plumb flux

For a barotropic flow linearized about a zonally symmetric basic state the barotropic Plumb wave activity flux is given by [92]:

$$\mathbf{A} = \frac{1}{2a^2} \begin{bmatrix} \frac{1}{cos\phi} \left(\frac{\partial \psi'^2}{\partial \lambda} - \psi' \frac{\partial^2 \psi'}{\partial \lambda^2} \right) \\ \frac{\partial \psi'}{\partial \lambda} \frac{\partial \psi'}{\partial \phi} - \psi' \frac{\partial \psi'}{\partial \phi \partial \lambda} \end{bmatrix}. \tag{2.4}$$

Figure 2.9 plots the Plumb flux vectors at 350hPa (arrows, normalized by H^2), the divergence of the Plumb flux (shading, also normalized by H^2), the critical line ($u = 0$, red) and the turning latitudes (where $n_s^2 = 5$, green) for $H = 333$m, 1km and 2km. Plots of the horizontal component of the full baroclinic Plumb flux are qualitatively similar.

The Plumb flux shows where the rectified effect of the orographic stationary wave affects the flow locally. The zonal-mean winds do not vary significantly between the different cases, suggesting that it is non-linearities close to the mountain which cause the increased meridional propagation. In the 333m case the flux close to the mountain is directed to the south-east but downstream of the mountain the flux is purely zonal. For $H = 1$km and $H = 2$km the zonal flux is much weaker relative to the meridional flux close to the mountain.

This relative weakening of the zonal flux can be used to quantify the transition to non-linearity. Figure 2.10 plots the ratio of the meridional Plumb flux across 30°N to the zonal Plumb flux across the 160° latitude circle. There is a clear jump from a ratio of about two to a ratio of more than seven between $H = 700$m and $H =$1km, further demonstrating the transition from zonal to meridional propagation. This pattern is qualitatively similar when other latitudes and longitudes are used.

There is a broad region to the southeast of the mountains in which the convergence of the Plumb flux acts to decelerate the flow (Figure 2.9). This region is north of

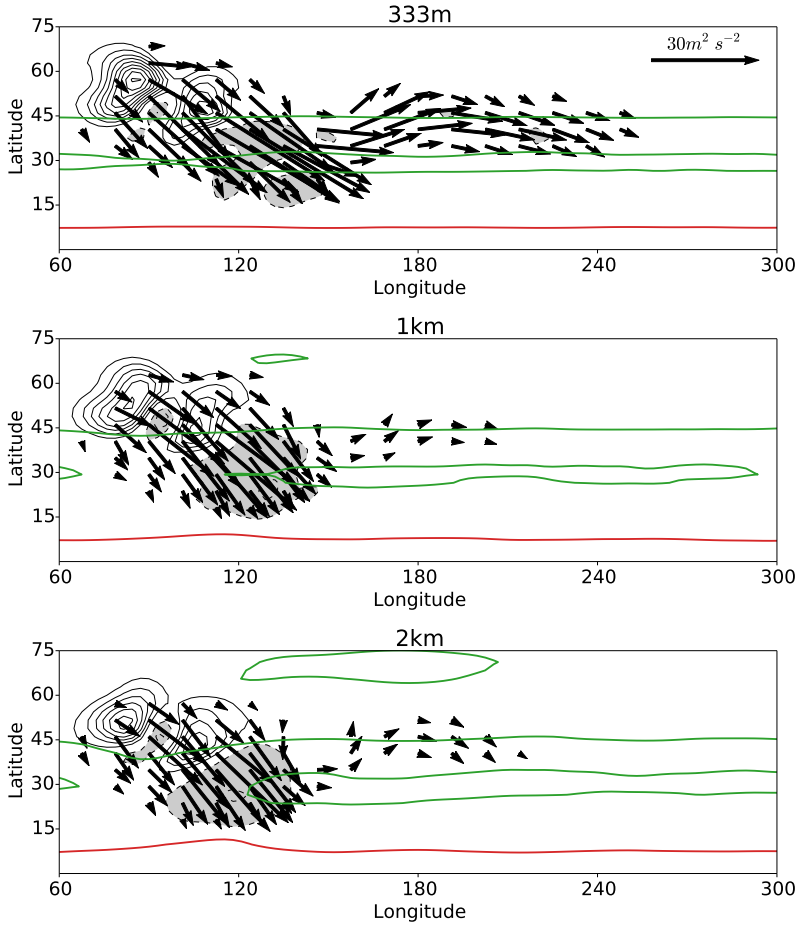


Figure 2.9: The normalized Plumb wave activity flux vectors at 350hPa (arrows), the normalized divergence of the Plumb flux (shading), the critical line ($u = 0$, red) and the $n_s^2 = 5.1$ contours (green) for the primitive equation model experiments with $H = 333$m (top), 1km (center) and 2km (bottom) experiments. Regions of flux convergence are shaded and the contour interval is 2×10^{-6}ms^{-2}.

the critical line and examination of the potential vorticity field shows that there is no significant wave-breaking in the time-mean field, suggesting that potential vorticity mixing due to transient eddies effectively damps the wave before it can break near the critical line. However, the deceleration is in the vicinity of the equatorward turning latitude and the waveguide is progressively eroded as H is increased. Comparing the terms in equation 2.2, this erosion appears to be mostly due to changes in the

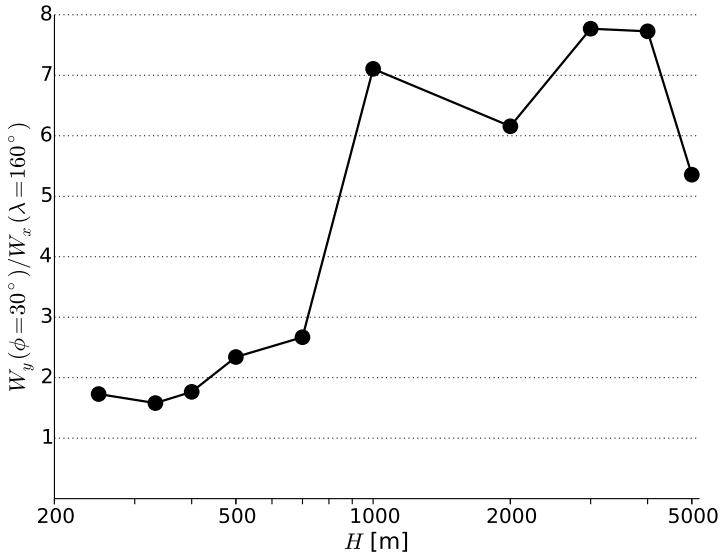


Figure 2.10: The ratio of the meridional component of the Plumb flux integrated across the 30°N latitude circle to the zonal component of the Plumb flux integrated across the 160° longitude circle plotted as a function of H. Note the logarithmic scale on the x-axis.

absolute vorticity induced by the deceleration. In the 2km experiment the region of deceleration is broad enough to distort the critical line, which is pulled a few degrees northwards near 120°.

This erosion of the waveguide is one possible cause of the transition from predominantly zonal to predominantly meridional propagation but there are several other possibilities. As shown in Swanson et al. (1997), barotropic jets have a finite carrying capacity for wave activity [121] and so if the wave activity generated by the mountain exceeds this limit it would lead to non-linear behavior. However, I have not found clear evidence for this mechanism here. Another possible cause of the transition is rotation of the vertical motion along the topography; I return to this in section 5c.

2.4 Other Model Configurations

2.4.1 Adding orography to a winter-like climate

The previous section emphasized the zonal nature of the linear response, in contrast to the many studies which have focused on the meridional propagation of orographically-forced stationary waves. The implication is that there is sensitivity to the mean flow, with some flows resulting in better waveguides. To confirm that this is the case I have repeated some of the experiments from the previous section with an additional term added to the reference temperature, equal to $\epsilon \times sin(\phi)$, with $\epsilon = 10$K and with the orography in the cooler hemisphere. The dashed curves in Figure 2.3 show the zonal wind and index of refraction profiles for this cooler hemisphere. Wavenumber five waves are no longer trapped but there is now a region between about 35° and 54° in which wavenumber four waves could be trapped.

The top panel of Figure 2.11 shows the Plumb flux at 350hPa for the new set-up with $H = 400$m, which I have verified is in the linear regime. The response close to the mountain is directed to the south-east and is stronger than in the corresponding $\epsilon = 0$K experiment (compare the scale of the arrows in Figures 2.10 and 2.11). Using finer scales for the arrows and contours shows that away from the mountain there is a weak zonal wave, and inspection of the eddy streamfunction shows that this wave has wavenumber four, as expected. Since the trapping region is further poleward in this set-up I have run experiments with the mountain centered further north, but this does not increase the zonal propagation.

The bottom panel of Figure 2.11 shows results from a case in which $H = 400$m and the latitudinal half-width (α in equation 1) of the mountain is decreased to 7.5°. Stationary forcing potentially excites all waves with the appropriate total stationary number, $k^2 + \ell^2$, but the relative forcing of the different (k, ℓ) pairs depends on the shape of the forcing. Ridge-like forcing should project more strongly on large k (small

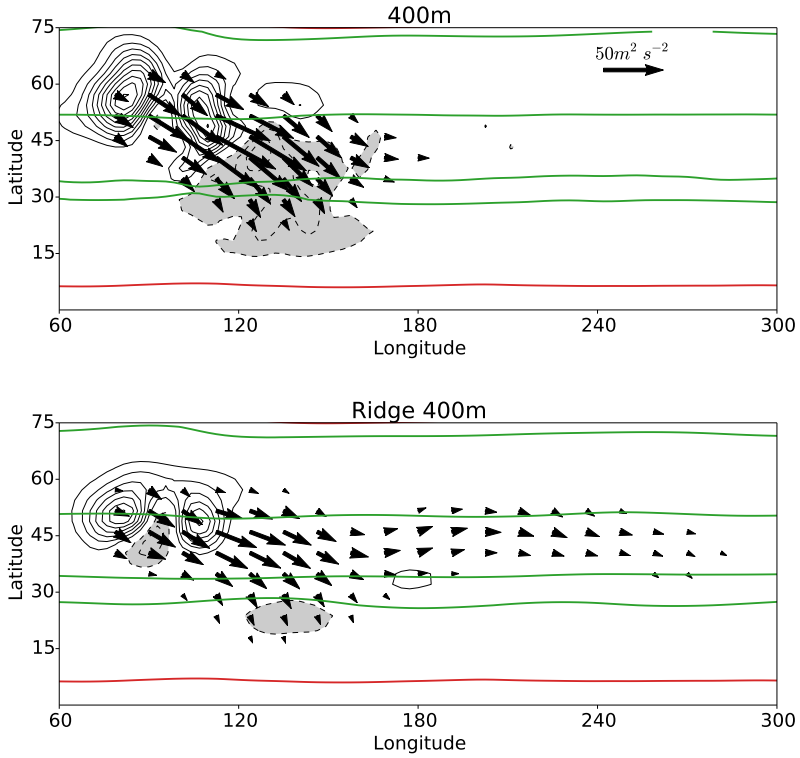


Figure 2.11: Same as Figure 2.9 but for experiments with $\epsilon = 10$K. The top panel shows the response to a 400m Gaussian mountain and the bottom experiment shows the response to a 400m ridge-like mountain. The contour interval is now $4 \times 10^{-6}\text{ms}^{-2}$ and the green lines show the $n_s = 4^4$ contours.

ℓ) compared to more isotropic topography, favoring zonal propagation since the ratio of zonal to meridional propagation is k/ℓ. Therefore a more zonal response is induced, which propagates almost around the entire latitude circle. However, since the linear response is roughly proportional to the total volume of the mountain, the response close to the mountain is weaker than for the original mountain. The response for larger mountain heights resembles the non-linear response when $\epsilon = 0$K with both the Gaussian mountain and with the ridge.

These results demonstrate the limitations of the index of refraction as a diagnostic of trapping for the GCM. While it correctly predicts which waves will be trapped in the two climates, it does not predict that trapping in the $\epsilon = 10$K case is weaker;

nor does it in itself predict that the ridge-like mountain produces a more strongly trapped response without further consideration of the relative excitation of different ray paths.

2.4.2 Removing the mountain-induced radiative cooling

Since the model does not simulate its own surface temperature there is some ambiguity as to the correct way to add orography. In the Held-Suarez set-up the Newtonian relaxation acts on σ-surfaces, so the near-surface air at the top of the mountain is relaxed to the same temperature as the near-surface air at sea level at the same latitude, resulting in a large radiative heating over the mountain. Figure 2.12 shows that in the 2km case the vertical average of this heating is up to 0.32K/day.

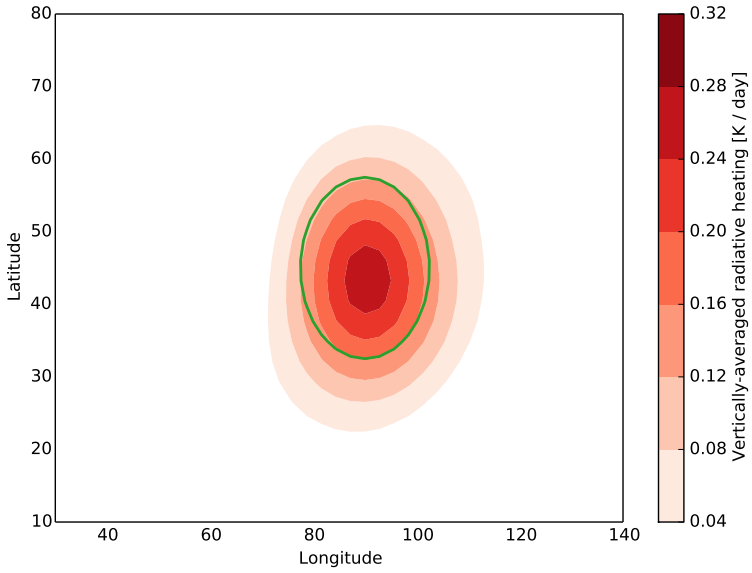


Figure 2.12: Vertically averaged radiative heating rate in the $H = 2$km case. The green oval shows the 1km contour of the mountain.

The simulations discussed in the previous two sections have included this heating, following the conventional approach taken by previous studies (e.g., [32]; [31]; [115]). However, the effects of the heating were investigated by repeating some simulations

with new zonally-varying equilibrium temperature (T_{eq}) fields which eliminated the heating. These T_{eq} fields are a function of pressure, rather than σ; so, for instance, all grid points at a given latitude with altitude 700hPa were relaxed to the same temperature. A new T_{eq} field had to be generated for each mountain height.

The responses with the new T_{eq} fields are very similar to the responses with the standard set-up, but are 25-50% stronger because the response to the radiative heating appears to oppose the response to the orographic forcing somewhat (Figure 2.13; note that the colorbar scale is larger than the one used in Figures 2.1 and 2.4). Nevertheless, a similar transition is seen from a predominantly zonally-propagating response to a predominantly meridionally-propagating response, indicating that the same dynamics are at play in both set-ups.

It is unclear which of these two methods of introducing orography into the model is more physically realistic. I have not attempted to answer this question here, but simply demonstrate the responses when either method is used.

2.5 Understanding the Linear Response

2.5.1 Barotropic model formulation

The barotropic model is formulated as a spectral model which solves the barotropic vorticity equation on a sphere, with Newtonian relaxation to a prescribed zonal-mean vorticity field ζ_E included in order to generate a zonal-mean flow which matches the primitive equation model

$$\frac{\partial \zeta}{\partial t} = -J(\psi, f + \zeta + h) + r\left(\zeta_E(\phi) - \zeta(\lambda, \phi, t)\right) - \nu\nabla^8\zeta, \tag{2.5}$$

where ψ is the streamfunction, ζ is the vorticity ($\nabla^2\psi$), $J()$ is a two-dimensional Jacobian operator and ν is a hyper-diffusion constant (set to $10^{-4}\mathrm{m}^8\mathrm{s}^{-1}$). $r = 10$

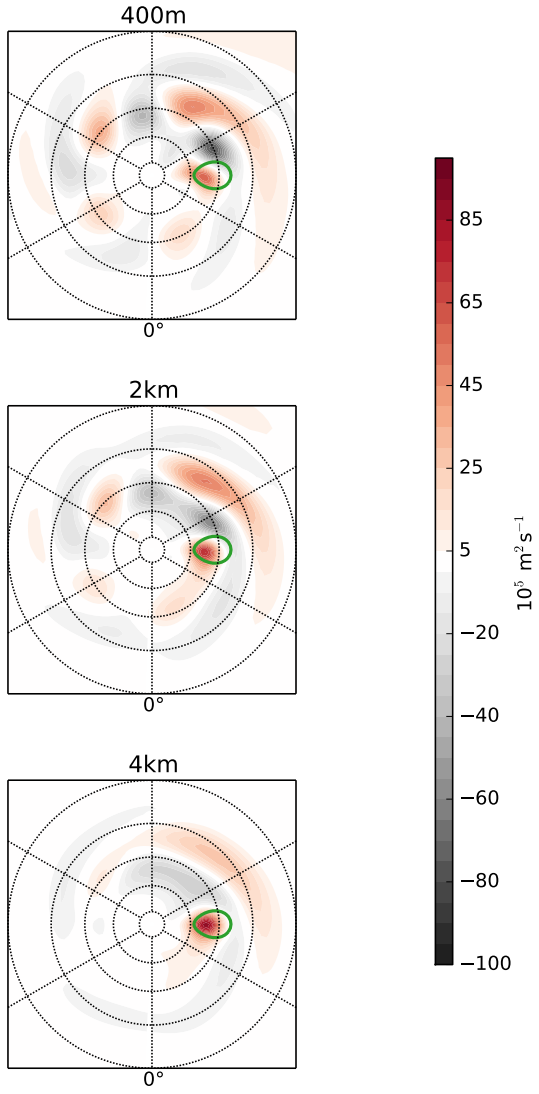


Figure 2.13: Normalized eddy streamfunction responses at 350hPa for three different mountain heights with the new T_{eq} fields that remove the vertically-averaged radiative heating.

days^{-1} in all experiments shown here, though r was varied by a factor of two to ensure that the results are not sensitive to this choice. ζ_E is calculated from the zonal mean zonal-wind profile I wish the model to relax to, u_E, which is discussed below.

Mountains are introduced into the model by a perturbation to the vorticity $h = f_0 H_b / H_s$, with $f_0 = 10^{-4}\text{s}^{-1}$, H_b representing the orography and H_s the depth of

the layer. The orography takes the same Gaussian form as in the primitive equation model. This set-up is very similar to the model used for the "direct numerical simulations" of Wang and Kushner (2010) [134] and is also similar to the shallow water experiments of Polvani et al. (1999) [93].

For linear external Rossby waves the orography must be reduced by a factor $\alpha = \psi_{surf}/\psi(p_e)$ in order to match the primitive equation model, where ψ_{surf} is the external mode streamfunction at the surface and $\psi(p_e)$ is the external mode streamfunction at the latitudinally-varying equivalent barotropic level [45]. This factor is subsumed in the definition of the layer-depth by setting $H_s = H_s^\star/\alpha$, where $H_s^\star$ is the actual depth of the barotropic layer. Rather than calculating α explicitly I simply take a representative value of 0.5 and let $H_s^\star = 5$km so that $H_s = 10$km. While one could try to mimic the linear response of the GCM in a barotropic model if the flow is dominated by external Rossby waves, there is no obvious way of quantitatively capturing the GCM's nonlinear response in a barotropic model. So the focus here is on qualitative rather than quantitative comparisons between the GCM and barotropic solutions.

The barotropic model was run at T85 resolution and data were again recorded once per model day. For each choice of u_E the model was integrated with H_b varying from 10m to 100m, in increments of 10m, and then with H_b varying from 200m to 4000m, in increments of 100m; making 49 experiments in total. In each experiment the model was integrated for 1000 days, with averages taken over the second half of the simulation.

2.5.2 Mimicking the responses of the GCM

In order to qualitatively reproduce the results from the primitive equation model the zonal winds in the barotropic model were relaxed to the time-mean, zonal-mean zonal wind profile at 350hPa from the control simulation of the primitive equation model at

T42 resolution, i.e $u_E = \overline{[u]}_{control,350hPa}$. The computations in [45] suggest a somewhat lower equivalent barotropic level, given the dispersion relation of the external Rossby wave, and I have verified that the results with the barotropic model are robust to choosing a lower level. Results using the flow at 350hPa are shown in order to make a more direct comparison with the figures from sections 2.3 and 2.4.

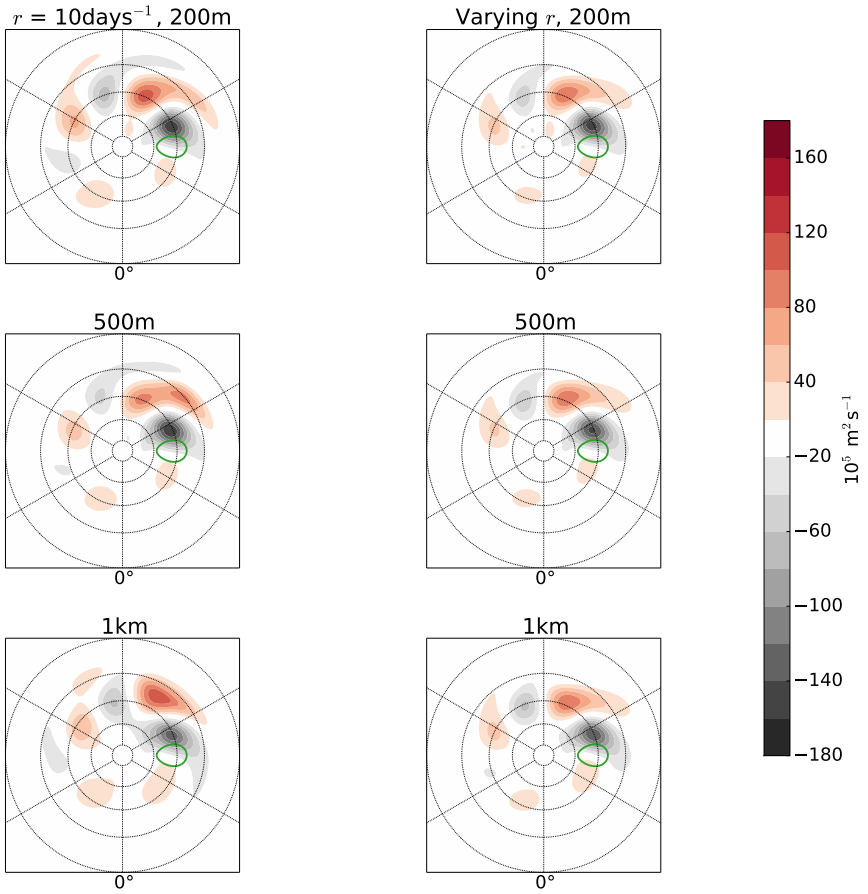


Figure 2.14: Left: the eddy streamfunction responses for three values of H_b from the barotropic simulations with the time-averaged zonal-mean zonal wind profile at 350hPa from the control simulation of the primitive equation model with $\epsilon = 0$K, normalized by 1000m / H_b and plotted using a polar stereographic projection. Right: same for the simulations in which the mean flow relaxation time r varies with latitude, as described in section 2.6.2.

The streamfunction responses to three different mountain heights in this simulation are shown in the left panels of Figure 2.14. For $H_b = 200$m a zonal wave

is produced which resembles the circumglobal wave seen in the primitive equation model, except that it extends further zonally and has no response to the north of the orography. By comparing the responses for different heights I have found that the transition to non-linearity takes place between $H_b = 300$m and $H_b = 500$m. The center-left panel of Figure 2.14 shows that when $H_b = 500$m the zonal wave is still present, though it is relatively weaker, and there is a new wavetrain propagating towards the equator. For $H_b = 1$km the meridional wave appears to have merged with the zonal wave to the southeast of the orography (bottom left panel), while downstream the zonal wave is still present.

The transition from zonal to meridional propagation can also be seen in the Plumb fluxes (Figure 2.15), as the meridional flux is larger and the zonal flux significantly weaker for $H_b = 500$m than for $H_b = 200$m. Just as for the primitive equation model then, the linear response of the barotropic model consists of a circumglobal wave, while the transition to non-linearity is characterized by the development of a meridionally-propagating wave.

However, when u_E is set to the profile generated by the GCM in the $\epsilon = 10$K case the barotropic response consists of a zonally-trapped wavenumber four wave, and forcing with a more ridge-like mountain does not (qualitatively) affect the response (not shown). Hence trapping is favored in the barotropic model compared with the GCM, and the barotropic model cannot capture the sensitivity of the GCM to the zonal-mean wind profile and to the shape of the orography.

2.5.3 The index of refraction and the barotropic model

It is striking how different the linear regime in the GCM simulation is from the classic result in Hoskins and Karoly (1981) and the corresponding barotropic result in Grose et al. (1979) ([54]; [36]). This difference can be understood qualitatively from the barotropic index of refraction. I have examined the linear responses in the

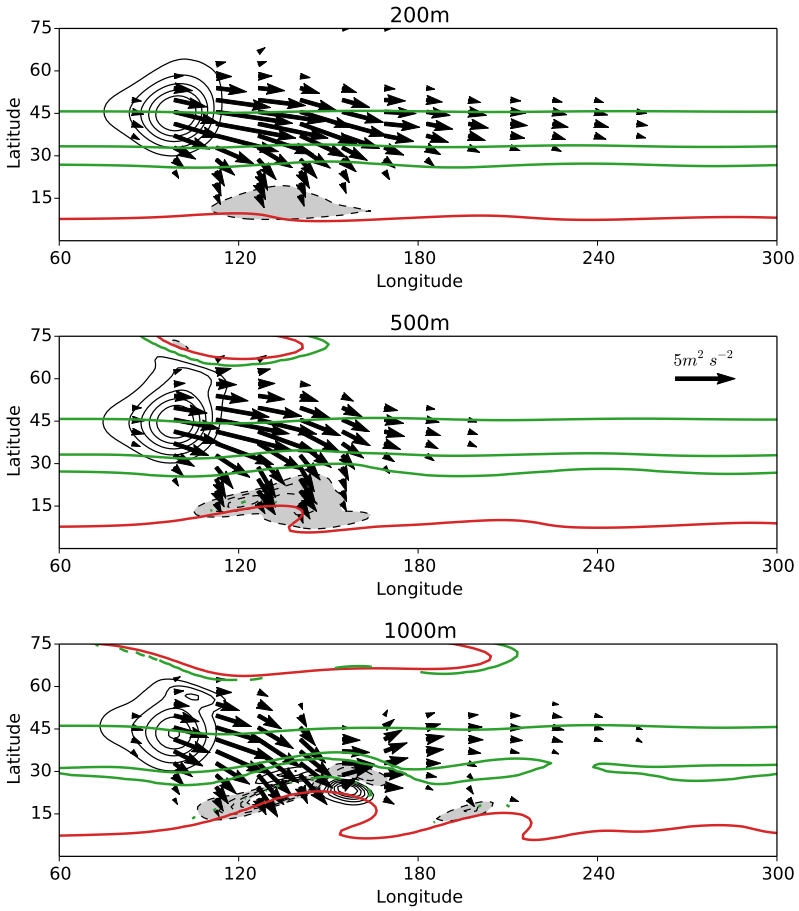


Figure 2.15: Same as Figures 2.9 and 2.11 but for the barotropic experiments with H_b =200m (top), 500m (middle) and 1km (bottom). The contour interval for the flux convergence is now 6×10^{-7}ms^{-2}.

barotropic model in which u_E is a linear combination of the 350hPa wind profile from the control experiment of the GCM and the 300hPa zonal wind profile used in [54], i.e., the average northern hemisphere wintertime flow from Oort and Rasmusson (1971) [83] ($\overline{[u]}_{300,HK}$). That is, u_e is given by

$$u_E = c \times \overline{[u]}_{350,GCM} + (1-c) \times \overline{[u]}_{300,HK}, \tag{2.6}$$

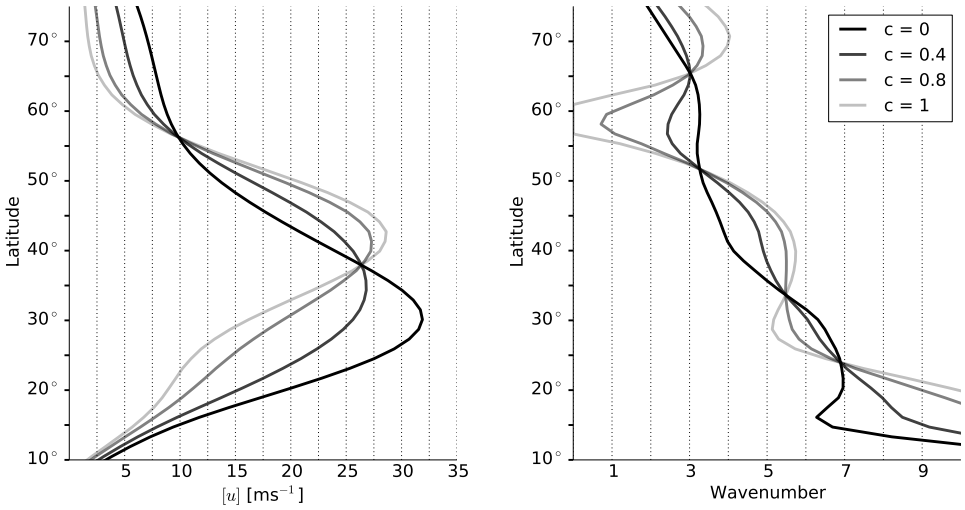


Figure 2.16: Same as Figure 2.3 but for u_E calculated from equation 2.6 with $c = 0$ (the 300hPa zonal wind profile used in [54]), $c = 0.4$, $c = 0.8$ and $c = 1$ (the 350hPa wind profile from the control experiment of the GCM).

where c is a constant. A third-order B-spline was used to interpolate $\overline{[u]}_{300,HK}$ onto the latitude grid used in the barotropic model. As can be seen from Figure 2.16, this zonal wind profile does not act as a waveguide near the mountain.

When $c = 0$ the response is what would be expected from [54], consisting of two waves traveling along great circles: one propagating polewards away from the orography and the other propagating equatorwards (top left panel of Figure 2.17). For $c = 0.4$ the response is similar, though there is less poleward propagation, but when c is increased to 0.8 the poleward propagating wave is mostly inhibited. This is due to the development of a turning latitude for long waves at high latitudes (see corresponding line in right panel of Figure 2.16). Finally when $c = 1$ the waveguide forms and the zonally trapped wave is clearly present (bottom right panel of Figure 2.17). From this I conclude that the response of the barotropic model can be mostly explained by the index of refraction, and that for understanding the linear regime of the GCM, at least, the barotropic model does not add to what can be learned from the index of refraction.

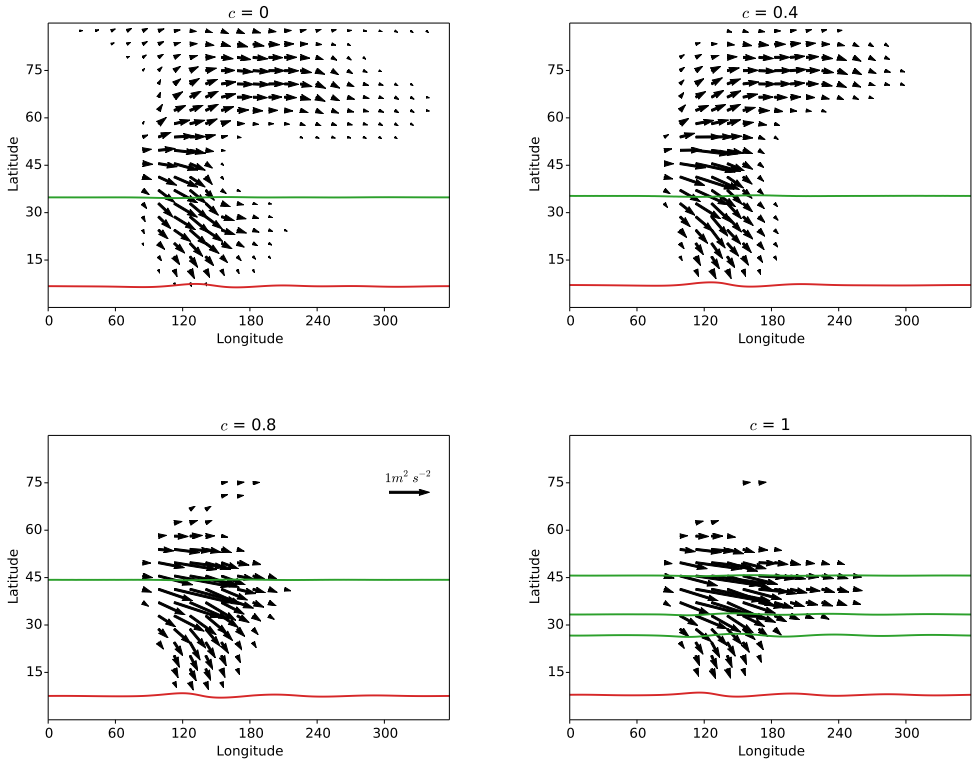


Figure 2.17: The Plumb fluxes (arrows), critical lines (red) and $n_s = 5$ contours (green) for $H_b = 100$m and $c = 0$ (top left panel), $c = 0.4$ (top right), $c = 0.8$ (bottom left) and $c = 1$ (bottom right). When $c = 0$ u_E is the 300hPa zonal-mean wind profile from [54] and when $c = 1$ u_E is the zonal-mean wind profile at 350hPa in the control simulation of the GCM under equinoctial conditions. The scale of the arrows is the same in all panels.

2.6 Understanding the Nonlinear Response

2.6.1 Vertical motion along the mountain surface

Since the barotropic model's response undergoes a similar transition from zonal to meridional propagation, it is natural to ask whether the barotropic model can be used to understand the nonlinear response of the GCM. I start by considering how the shape of the vortex stretching in both models changes as the orographic forcing is strengthened. In both the primitive equation model and the barotropic model the

vertical motion at the surface of the mountain is given by

$$F_{nl} = -f\mathbf{v} \cdot \nabla h, \tag{2.7}$$

where $\mathbf{v}$ is the flow at the lowest model level in the primitive equation model. At small heights F_{nl} is dominated by its linear approximation

$$F_l = -f_0[u]\frac{\partial h}{\partial x}, \tag{2.8}$$

while at larger heights the non-linear terms are more important. In both the GCM and the barotropic model F_l consists of the winds flowing up the west flank of the mountain and down the east flank of the mountain, while the non-linear terms cause F_{nl} to rotate clockwise. Consistent with the responses transitioning from being more zonal to more meridional, the forcing goes from being aligned east/west to being more north-west/south-east. This progression is shown for the barotropic model in Figure 2.18 (the rotation is weaker in the GCM).

As was mentioned in section 2.3.4, this rotation is a possible cause of the transitions in the two models. In particular, Ringler and Cook (1997) [99] suggest that the difference between F_l and F_{nl} is a useful measure of the nonlinearity of the response. To test the importance of this rotation of the vortex stretching, I have run an experiment with the barotropic model in which the orographic forcing is replaced by a fixed vorticity source:

$$\frac{\partial \zeta(\lambda, \phi, t)}{\partial t} = -J(\psi, f + \zeta) + cF_l(\lambda, \phi) + ..., \tag{2.9}$$

where c is a constant factor and F_l is the linear forcing defined in equation 2.8. This keeps the shape of the forcing fixed while its amplitude can be varied, eliminating the rotation of the forcing by the non-linear terms. The responses in this experiment are qualitatively unchanged from the responses to the orographic forcing (Figure 2.19)

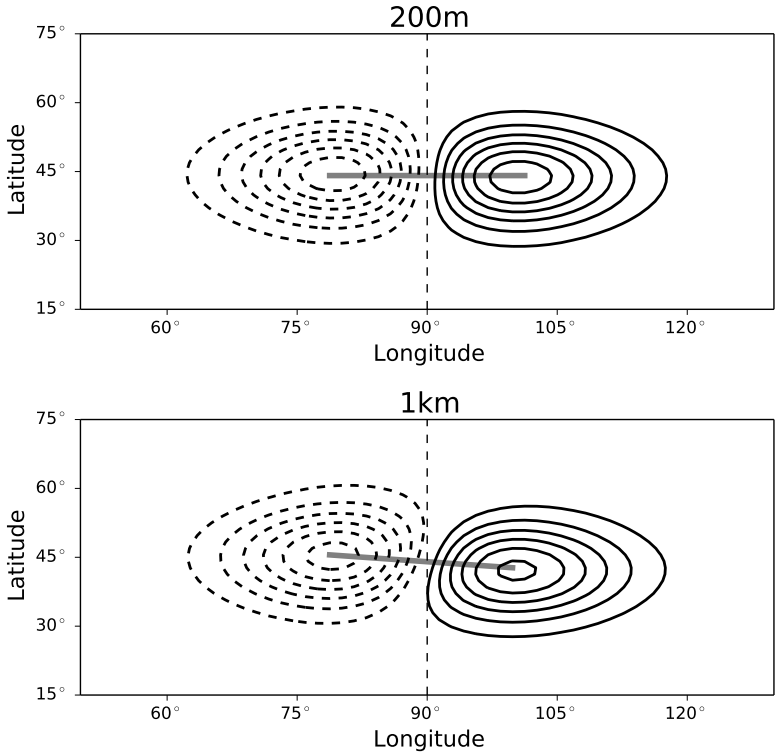


Figure 2.18: The full vertical motion forced by the topography, F_{nl}, for the barotropic experiment when $H_b = 200$m (top) and 1km (bottom). The plots have been normalized by $H_b/1000$m and the contour interval is 250mday^{-1}, with positive contours solid and negative contours dashed. The thin dashed lines indicate the latitude of the peak orography and the thick gray lines connect the centers of vertical motion.

and so the rotation of the forcing with increasing amplitude is not responsible for the transition in the barotropic model. The suggestion is that this result likely carries over to the primitive equation model.

2.6.2 Plumb fluxes in the barotropic model

Returning to Figure 2.15, even for $H_b = 200$m there is a small amount of leakage from the waveguide, which propagates all the way to the equatorward critical line, where the wave breaks. For $H_b = 500$m the zonal flux is relatively weaker and the meridional flux is strengthened, as seen in the GCM, but the leakage from the waveguide has

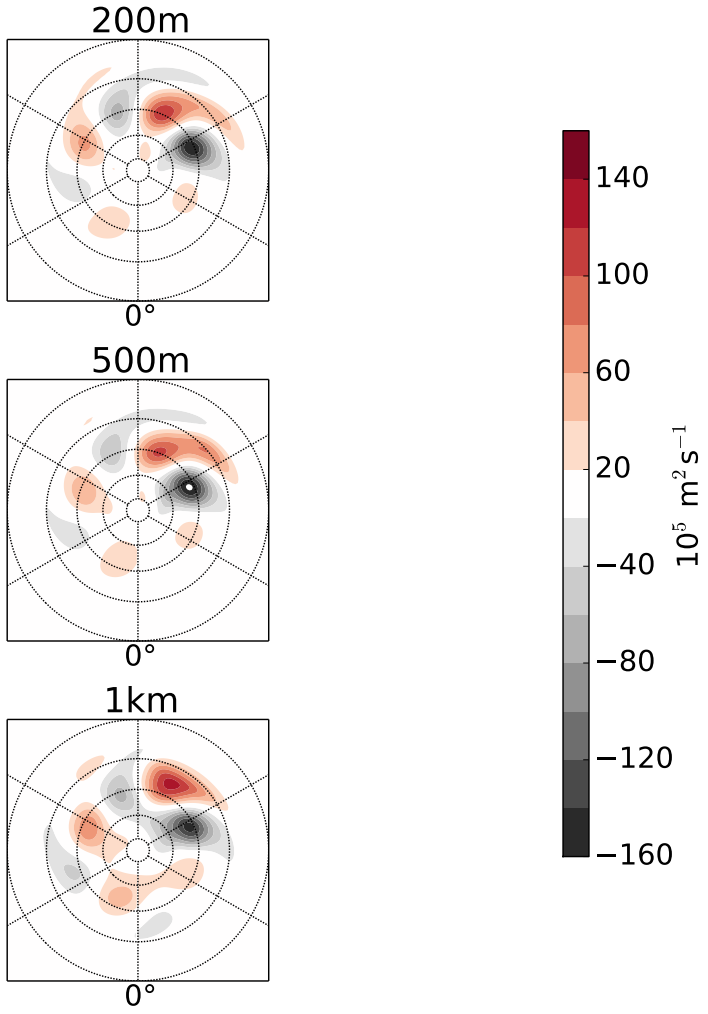


Figure 2.19: As in Figure 2.14, but for the barotropic simulations in which the shape of the vorticity forcing is kept fixed. The titles show the height of mountains which would produce the same vorticity source.

caused a significant northward deformation of the critical line near 120°. When $H_b = 1$km the critical line is highly deformed and the wave reflects off the critical line. Inspection of the potential vorticity field shows the presence of a Kelvin cat's eye, confirming that a reflecting critical layer has been created. For $H_b \geq 2700$m the response actually propagates around the entire latitude circle by reflecting off of critical layers to the north and south.

The transition to meridional propagation takes place before the development of the reflecting critical layer, but I believe that the deformation of the critical line is still responsible for the transition in the barotropic model. For instance, when the critical layer is close enough to the waveguide it could absorb wave activity from the waveguide, promoting meridional propagation. To test whether this is the case, I have repeated the same experiment but with r linearly increasing between 30°N/S and 15°N/S from 10 days^{-1} to 1 day^{-1}. The value of r is 1 day^{-1} between 15°N and 15°S. This set-up does not allow the leakage from the waveguide to propagate as far into the tropics and hence stops the deformation of the critical layer. This delays the transition to non-linearity (right panels of Figure 2.14), so that even at H_b = 1km the response is in the linear regime. At large enough H_b the response does become non-linear, though not due to a deformation of the critical line, and the response is very different to the non-linear responses of either the barotropic model or of the GCM.

The barotropic model is thus able to qualitatively reproduce the transition from a meridionally-trapped wave to a meridionally-propagating wave seen in the GCM, but this transition takes place for different reasons in the two models. Reasons for the inability of the barotropic model to mimic the behavior of the primitive equation model may include the lack of transient eddies or the way the mean-flow is restored in the absence of a Hadley cell. These differences mean that the barotropic model as formulated here cannot be used to investigate the breakdown of the linear response in the primitive equation model quantitatively, although in both models there is leakage from the waveguide at even the smallest mountain heights, and this leakage seems to precede the transition to a response with more meridional propagation.

2.7 Conclusion

In this study I have added Gaussian orography to an idealized, dry GCM forced with the Held-Suarez set-up, searching for a parameter regime in which the model's response to the orography is a linear function of the height of the orography. The smallest mountains considered ($H < 1$km) appear to be in a linear regime for which the response consists of a zonal wave with wavenumber five that is trapped in the mid-latitude jet, resembling the circumglobal wave of Branstator (2002) [9]. For experiments with larger H the response is increasingly dominated by a wave which propagates meridionally into the tropics and the response normalized by the height of the mountain also becomes relatively weaker.

Modifying the GCM's climate by introducing an interhemispheric asymmetry in the radiative equilibrium temperature significantly reduces the trapping when the Gaussian orography is placed in the cooler hemisphere. The stationary wave response is thus able to propagate further meridionally, even for small mountains, as would be expected from previous studies (e.g., [54]; [20]). However, if a more ridge-like mountain is used then zonal waves are more strongly excited and zonal propagation plays a more prominent role in the response. The index of refraction shows that in both climates there is the potential for trapping, but it cannot by itself determine whether the waveguides will be excited by a given orographic forcing.

As a first step towards understanding the transition I have added orographic forcing to a barotropic model on a sphere. Whether the mean-flow is relaxed to the flow from the simulation forced with the standard Held-Suarez settings or to the flow from the simulation with the interhemispheric asymmetry, this model's response to weak, Gaussian forcing consists of a meridionally-trapped, zonally-propagating wave. This is consistent with what is expected from the barotropic index of refraction, and is similar to the results of [77]. For strong enough forcing a meridional wave develops and increasingly dominates the response.

In this sense the barotropic model can successfully reproduce the GCM's transition from zonal to meridional propagation, however the mechanisms responsible for these transitions appear to be quite different in the two models. In the barotropic model leakage from the waveguide is able to propagate to the equatorward critical line, deforming it and pulling it poleward. I believe that the critical line is responsible for the transition when it is close enough to the waveguide, perhaps by absorbing wave activity from the waveguide. For stronger forcings a nonlinear, reflecting critical layer develops. If the wave activity is unable to reach the critical line (e.g., if the mean-flow is restored more strongly at low latitudes) then the transition to non-linearity is significantly delayed and the non-linear response is very different.

I have been unable to confirm what causes the regime transition in the GCM, though in this model most of the leakage from the waveguide is mixed by transient eddies before reaching the critical line and so deformation of the critical line cannot be responsible for the increased meridional propagation. Instead, some possible causes of the transition in the GCM are nonlinearities near the source preventing the waveguide from being excited, or non-linear distortion of the waveguide itself. In both models the rotation of the vortex stretching as the orographic forcing is increased plays a secondary role in the transition.

So although much of the theory of stationary waves has been developed in barotropic settings, barotropic dynamics are not sufficient for understanding the transition in the GCM. One layer systems that more closely mimic the upper tropospheric dynamics of the GCM will be needed if simple models are to be useful in analyzing the GCM results quantitatively.

The orography is the only zonal asymmetry present in the experiments and so the orographic waves are free to propagate without interacting with other stationary waves, which is another way for linear dynamics to break down in a more realistic

setting. I have also not explored how the results are affected by changing the latitude of the orography, apart from briefly in section 2.4.

By isolating a regime in which a dry GCM responds linearly to orography, this study reminds us that the responses to orography of realistic amplitude, even to isolated orography imposed on an otherwise zonally symmetric climate, may not resemble the linear responses, even qualitatively. The results also add to the growing body of literature concerning circumglobal waves, which may be of interest to oceanographers studying the interaction of ocean ridges and the ACC (e.g., [122]). Finally, these results bring the study of stationary waves back to the earlier emphasis on zonal propagation and the potential sensitivity of stationary waves to the mean-flow.

Chapter 3

The Impact of Orographic Forcing on the Momentum Budget of a Dry Atmosphere

3.1 Introduction

After discussing the zonally-asymmetric response of the dry general circulation model (GCM) to idealized, Gaussian orography in the previous chapter, this chapter focuses on the GCM's zonally-symmetric response; specifically, on the response of the GCM's zonal-mean momentum budget.

In the absence of friction, the non-acceleration theorem says that the torque exerted on the atmosphere by the orography is exactly balanced by the convergence of momentum by the stationary waves which the orography excites. Consider the eddy potential vorticity (PV) equation for an inviscid, adiabatic, continuous quasi-geostrophic (QG) system, linearized about a zonal-mean flow $\bar{u}$ [40]

$$\frac{\partial q^*}{\partial t} + \bar{u}\frac{\partial q^*}{\partial x} + v^*\frac{\partial \bar{q}}{\partial y} = 0, \tag{3.1}$$

where $q^* = \nabla^2\psi^* + \frac{f_0^2}{\rho}\frac{\partial}{\partial z}\left(\frac{\rho}{N^2}\frac{\partial\psi^*}{\partial z}\right)$ is the eddy PV, v^* is the eddy meridional wind and $\frac{\partial\bar{q}}{\partial y} = \beta - \frac{\partial^2\bar{u}}{\partial y^2} - \frac{f_0^2}{\rho}\frac{\partial}{\partial z}\left(\frac{\rho}{N^2}\frac{\partial\bar{u}}{\partial z}\right)$ is the zonal-mean meridional PV gradient. ψ^* is the eddy streamfunction, f_0 is a reference value of the Coriolis parameter, ρ is density and N^2 is the buoyancy frequency. The vertical co-ordinate $z = Hln(p_s/p)$, where H is the scale-height of the atmosphere, p is pressure and p_s is surface pressure. The surface boundary condition is the QG thermodynamic equation at $z = 0$

$$\frac{\partial}{\partial t}\left(\frac{\partial\psi^*}{\partial z}\right) + \bar{u}\frac{\partial}{\partial x}\left(\frac{\partial\psi^*}{\partial z}\right) - v^*\frac{\partial\bar{u}}{\partial z} = -\frac{N^2}{f_0}w.$$

The lower boundary condition on the vertical velocity is

$$w(z=0) = -\frac{\partial}{\partial t}\left(\frac{f_0}{g}\psi^*\right) + \bar{u}\frac{\partial h}{\partial x},$$

where h is the height of the mountain and g is the gravitational constant. Substituting and re-arranging then gives

$$\frac{\partial}{\partial t}\left(\frac{\partial\psi^*}{\partial z} - \frac{N^2}{g}\psi^*\right) + \bar{u}\frac{\partial}{\partial x}\left(\frac{\partial\psi^*}{\partial z}\right) - v^*\frac{\partial\bar{u}}{\partial z} = -\frac{N^2}{f_0}\bar{u}\frac{\partial h}{\partial x} \quad \text{at } z = 0. \tag{3.2}$$

Multiplying equation 3.1 by q^*, equation 3.2 by $s^* = \frac{\partial\psi^*}{\partial z} + \frac{N^2}{f_0}h$ and taking zonal-means gives

$$\frac{1}{2}\frac{\partial\overline{q^{*2}}}{\partial t} = -\overline{v^*q^*}\frac{\partial\bar{q}}{\partial y}, \quad \text{for } z > 0, \tag{3.3}$$

$$\frac{1}{2}\frac{\partial\overline{s^{*2}}}{\partial t} - \frac{N^2}{g}\overline{s^*\frac{\partial\psi^*}{\partial t}} = \overline{v^*s^*}\frac{\partial\bar{u}}{\partial z} = -\overline{v^*s^*}\frac{\partial\bar{s}}{\partial y}. \quad \text{at } z = 0, \tag{3.4}$$

The left hand sides of these equations are zero for a steady wave and so $\overline{v^*q^*} = \overline{v^*s^*} = 0$.

In the Transformed Eulerian Mean formulation the zonal momentum equation is

$$\frac{\partial\bar{u}}{\partial t} = \overline{v^*q^*} + f_0\overline{v^R}, \tag{3.5}$$

where $\overline{v^R}$ is the residual velocity

$$\overline{v^R} = \bar{v} - \frac{f_0}{\rho}\frac{\partial}{\partial z}\left(\frac{\rho}{N^2}\overline{v^*\frac{\partial \psi^*}{\partial z}}\right). \tag{3.6}$$

Integrating the momentum equation vertically and using a radiation condition at infinity then gives

$$0 =< \overline{v^*q^*} >= - < \frac{\partial \overline{u^*v^*}}{\partial y} > + \frac{f_0^2}{N^2}\overline{v^*\frac{\partial \psi^*}{\partial z}}(0), \tag{3.7}$$

where angle brackets denote vertical integrals. From before,

$$\overline{v^*s^*}(0) = \overline{v^*\frac{\partial \psi^*}{\partial z}}(0) + \frac{N^2}{f_0}\overline{v^*h} = 0,$$

hence

$$\overline{v^*\frac{\partial \psi^*}{\partial z}}(0) = -\frac{N^2}{f_0}\overline{v^*h}.$$

Finally, substituting into equation 3.7 and using geostrophy

$$< \frac{\partial \overline{u^*v^*}}{\partial y} >= \overline{h\frac{\partial p}{\partial x}}. \tag{3.8}$$

So the expectation from linear theory is that, in the absence of friction, the stationary eddy momentum flux (EMF) convergence and the mountain torque exactly balance. Experiments with GCMs, however, have shown that other terms in the momentum budget also have significant responses when mountains are added. Manabe and Terpstra (1974) compared simulations of a GCM with and without topography, and saw a reduction in the transient EMF when topography is included [76]; while Cook and Held (1992) found that in an idealized, moist GCM the mountain torque is mostly balanced by a reduction in the surface friction [20]. This chapter seeks to add to these studies by analyzing the momentum budgets of the experiments described

in the previous chapter. A particular focus is the impact of the transition in the model's response from predominantly zonal to predominantly meridional propagation as the height of the orography is increased. Intuitively, this transition should lead to a relatively stronger stationary EMF in the non-linear regime, suggesting that the transition is of consequence for the model's momentum budget.

This hypothesis is tested below, and the responses of the momentum budget in the linear and non-linear regimes are investigated more generally. The GCM results are also compared to simulations with a stationary wave model in order to help bridge the gap between linear theory and the behavior of the GCM.

3.2 Momentum Budget of the Control Integration

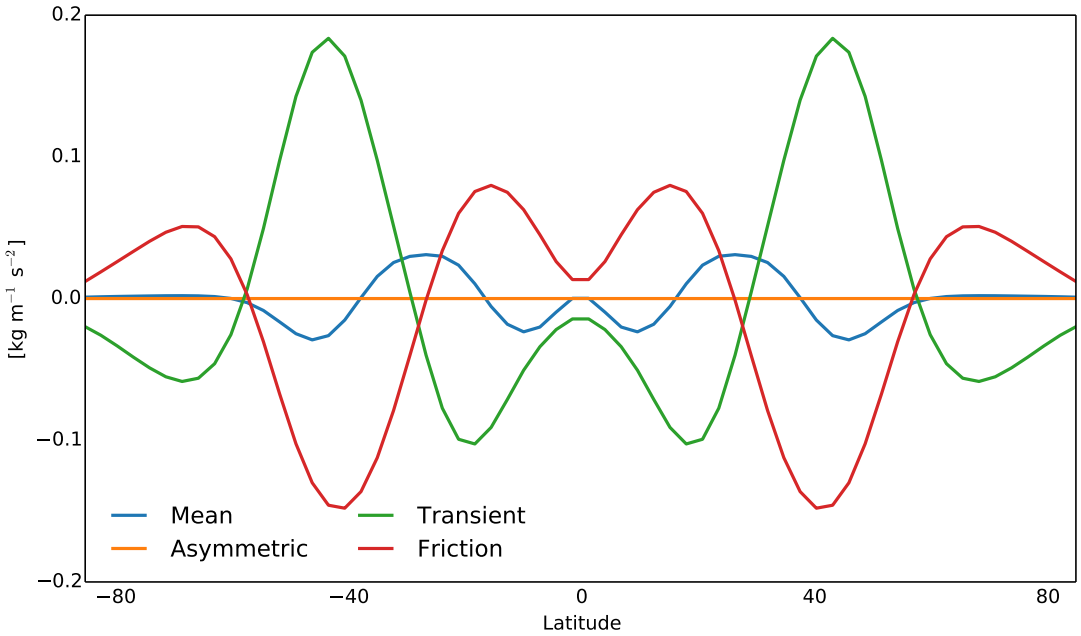


Figure 3.1: Vertically-integrated terms in the zonal-mean momentum budget of the control simulation.

Before analyzing the model's responses, I briefly discuss the momentum budget of the control integration. The steady state, vertically-integrated zonal-mean momen-

tum budget of the GCM can be written as

$$-\int_0^{p_s} \frac{dp}{g} \frac{1}{acos^2\phi} \frac{\partial}{\partial\phi} \left(cos^2\phi \left(\overline{[u][v]} + \overline{[u]^*[v]^*} + \overline{[u'v']} \right) \right) - \left[\overline{\frac{p_s}{acos\phi} \frac{\partial h}{\partial\lambda}} \right] + [\overline{F}] = 0, \quad (3.9)$$

where p_s is surface pressure, a is the Earth's radius, F is friction, square brackets are time means, overbars are zonal means, asterisks are deviations from the zonal mean and primes are deviations from the time mean. I calculate the transient term using the daily zonal-mean surface pressure (data is collected once per day):

$$-\left[\int_0^{\overline{p_s(t)}} \frac{dp}{g} \frac{1}{acos^2\phi} \frac{\partial}{\partial\phi} \left(cos^2\phi(\overline{u'v'}) \right) \right].$$

The profiles of these terms in the control integration are shown in Figure 3.1. As expected, the main balance is between the transient EMF convergence and the friction. These two terms are largest at midlatitudes, where the transient eddies accelerate the flow and the friction decelerates the flow, and change sign in the tropics and at high latitudes. Both terms are small in the subtropics, where the momentum flux by the mean flow is the largest term in the budget.

3.3 Response to Small Mountains

3.3.1 Normalized torque and stationary EMF convergence

The thin lines in Figure 3.2 show the profiles of the torque, normalized by $1km/H$ (top panel), the normalized stationary EMF convergence (middle panel) and the sum of these terms (bottom panel) for the small ($H < 1km$) mountain cases. The torque is approximately linear for these heights and decelerates the flow over most of the mountain and then weakly accelerates the flow between about 55° and 65°, as was seen in section 2.3.3. The stationary EMF convergence is also roughly linear, but

is shifted polewards of the torque, as it accelerates the flow between about 40° and 70° and decelerates the flow at lower latitudes (note: the larger EMF convergence for the 333m case (orange curve) is a result of sampling error). A similar poleward displacement of the stationary EMF convergence relative to the torque can be seen in Figure 13 of [20]. Because of this offset, and the fact that the stationary EMF convergence is slightly larger than the torque, the two terms do not cancel (bottom panel of Figure 3.2) and hence the other terms in equation 3.9 must respond so as to balance the momentum budget. However, the responses of the friction, the momentum flux by the mean flow and the transient EMF are comparable to the sampling error in these experiments; i.e., the changes in the hemisphere with the mountain are comparable to the changes in the hemisphere without the mountain. As such, the discussion of how the momentum balance is maintained is delayed until section 4.

The poleward displacement of the stationary EMF convergence is likely to be caused by a stationary non-linearity and/or by the interaction of the stationary wave with transient eddies. To investigate the relative importance of these two factors, the next subsection presents the results of several experiments in which orography was added to a stationary wave model.

3.3.2 Stationary wave model results

Model description

Following previous studies such as [49] and [17], the stationary wave model consists of the GFDL spectral dynamical core with stronger hyperdiffusion, Rayleigh friction and Newtonian damping; and with the zonal-mean flow strongly relaxed to the time- and zonal-mean flow in the control simulation of the full non-linear model. The results described below come from a simulation in which the hyperdiffusion was doubled from 1.157 $\times 10^{-4}$ $\mathrm{m^8 s^{-1}}$ in the original GCM simulations to 2.31 $\times 10^{-4}$ $\mathrm{m^8 s^{-1}}$ and the

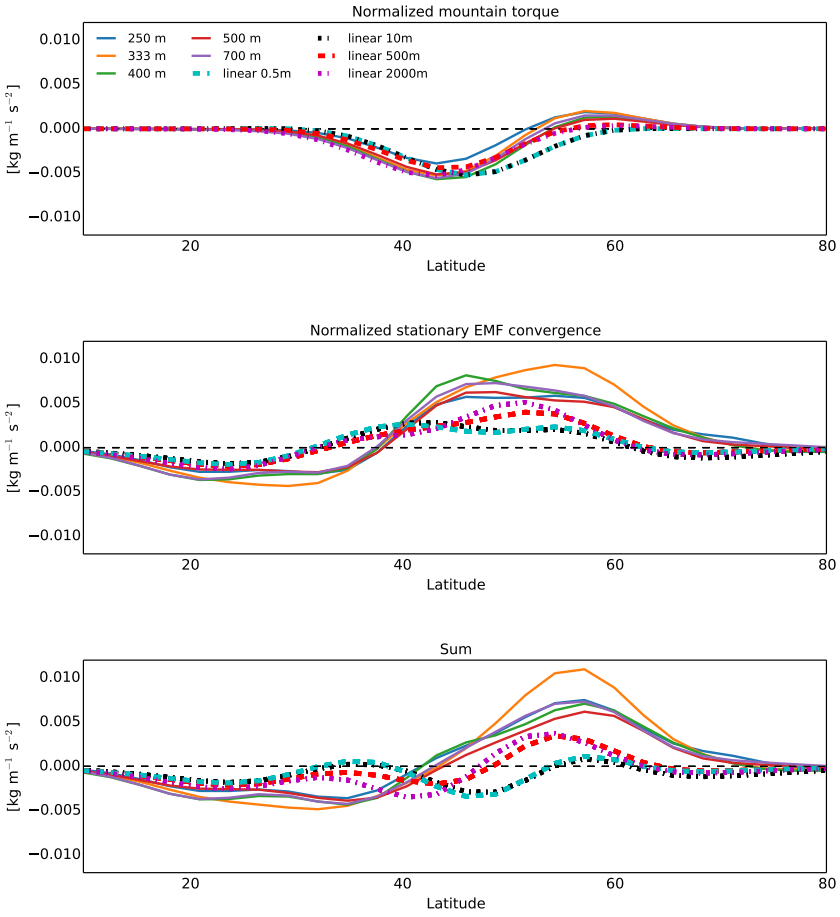


Figure 3.2: The normalized mountain torque (top panel), the convergence of the normalized stationary EMF (middle panel) and the sum of these (bottom panel) for the experiments in the linear regime. The dashed lines show the results for the stationary wave model experiments.

Rayleigh friction damping times for both the vorticity and divergence equations were 0.3, 0.5, 1.0, and 8.0 days at the lowest four σ levels (0.997, 0.979, 0.935 and 0.866), and 15 days throughout the rest of the domain. The Newtonian cooling time-scale was decreased from 40 days (the Held-Suarez value) to 15 days at all levels and the relaxation time-scale of the zonal-mean flow was set to 1 day. There is no objective method for choosing the optimal parameter settings for creating a stationary wave

model and so the simulations were repeated with a number of different settings to ensure that the results are robust to the choices made.

In all experiments the model was integrated for 200 days and averages were taken over days 50 to 200. The flow is steady after 15-20 days. Figure 3.3 compares the normalized eddy streamfunction response of the stationary wave model to $H = 500$m orography and the $H = 400$m simulation with the full GCM. The patterns of the responses are very similar, though the stationary wave model's response is about 25% weaker than the GCMs. The reason for this is that the strong damping limits the zonal propagation of the wave: using finer contour levels reveals that in the GCM the zonal wave actually propagates completely around the latitude circle and constructively interferes with itself. In the stationary wave model the wave is damped before it can make it all the way around. I was unable to find a parameter setting in which the damping is weak enough to allow the wave to propagate completely around the latitude circle while still strong enough to eliminate the transient eddies.

Momentum budget response

The thick dashed lines in Figure 3.2 show the torque and stationary EMF convergence in several of the experiments with the stationary wave model. These are very similar in the $H = 0.5$m and $H = 10$m cases (cyan and black curves, respectively), with the torque decelerating the flow between about 35° and 55° and the stationary EMF convergence accelerating the flow at these latitudes. However, the stationary EMF convergence has a minimum directly above the mountain, whereas the torque is largest there. This reflects a slight deceleration of the jet by the mountains, which causes a small positive response of the friction term (not shown). So for these small mountain the stationary wave model nearly behaves as would be expected from linear theory, but the strong surface friction stops the torque and the stationary EMF convergence from balancing exactly.

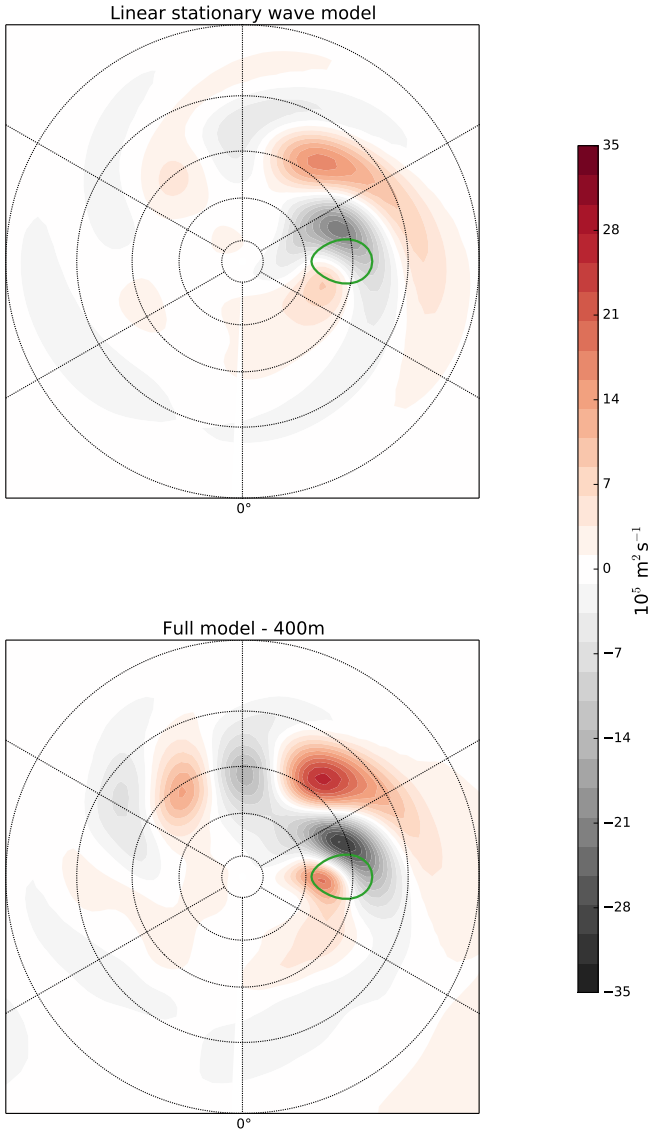


Figure 3.3: The top panel shows the normalized eddy streamfunction response at 350hPa of the stationary wave model to orography with $H = 500$m while the bottom panel shows the normalized response of the full GCM with $H = 400$m.

For both $H = 500$m and $H = 2$km (red and purple curves, respectively) the deceleration by the torque only extends to about 50°, while the stationary EMF convergence has a maximum at about 55°, suggesting the presence of a stationary non-linearity that causes increased stationary EMF convergence on the poleward flank

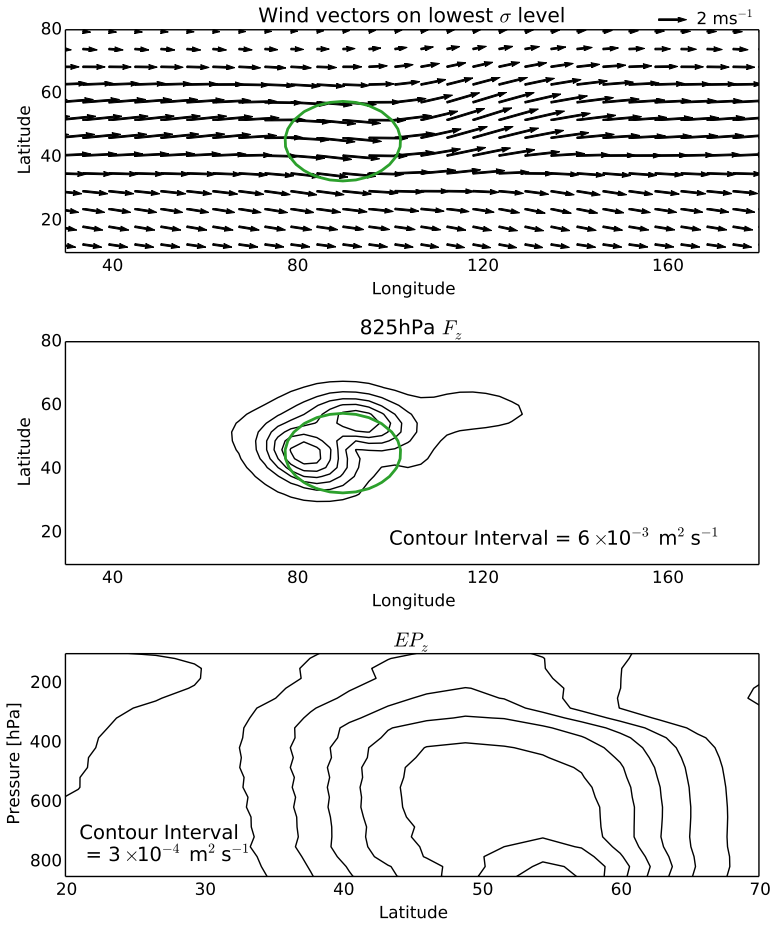


Figure 3.4: Top panel: the wind vectors on the lowest σ level for the $H = 500$m experiment with the stationary wave model. Middle-panel: PF_z at 825hPa for the same experiment. Bottom panel: EP_z for the same experiment.

of the mountain (note that the maximum EMF convergence is relatively larger for the 2km experiment than for the 500m experiment). The presence of this non-linearity suggests that air is flowing around the mountain, in addition to flowing up and over it. This can be seen in the top panel of Figure 3.4, which plots the total wind vectors on the lowest σ-level in the $H = 500$m experiment. Over the mountain the flow is deflected to the south slightly and then downstream of the mountain the flow is deflected to the north.

This meridional flow transports heat and hence acts as a stationary wave source, as a poleward eddy heat flux corresponds to the vertical propagation of wave activity. To illustrate this, the middle panel of Figure 3.4 shows the vertical component of the Plumb flux (PF_z) at 825hPa for the $H = 500$m experiment, with PF_z calculated as [92]

$$PF_z = \frac{p}{1000hPa} f cos\phi \left(\frac{\partial[\overline{\theta}]}{\partial z} \right)^{-1} \left([v^*\theta^*] - \frac{[\psi^*]}{acos\phi} \frac{\partial[\theta^*]}{\partial \lambda} \right), \tag{3.10}$$

where θ is potential temperature. There are two centers of upward propagating wave activity, one directly to the west of the mountain, representing air rising as it encounters the west flank of the mountain, and one to the north of the mountain due to the poleward heat flux by the air deflected around the mountain. [98] also found that the stationary eddy heat flux produces a second stationary wave activity source polewards of the orography in their orographic forcing experiments.

The zonal-mean of PF_z is the vertical component of the Eliassen-Palm flux

$$EP_z = \frac{p}{1000hPa} f cos\phi \left(\frac{\partial[\overline{\theta}]}{\partial z} \right)^{-1} \overline{[v^*\theta^*]}, \tag{3.11}$$

which is shown in the bottom panel of Figure 3.4 for the $H = 500$m experiment. This is largest at about 55°, just as the stationary EMF convergence is largest at 55° in this experiment.

The equivalent plots for the full GCM are very similar but the results are shown here for the stationary wave model to demonstrate that the stationary non-linearity is responsible for this effect, not the transient eddies. Note, however, that the stationary non-linearity may be caused by the strong radiative heating over the mountain (see section 2.4.2), though even in the experiments in which the radiative heating is removed the stationary EMF is shifted polewards of the torque (not shown).

The effects of the transient eddies can be inferred by comparing the curves for the stationary wave experiments with the curves for the full GCM in Figure 3.2.

This indicates that the transients push the stationary EMF convergence even further polewards, though it is also possible that this difference is caused by the strong damping in the stationary wave model. However, Figure 2.9 from Chapter 2 supports the idea that the transients push the wave polewards, as it can be seen that the transient eddies mix out the stationary wave between between about 30° and 40°. This results in stationary EMF divergence at these latitudes and so the region of net stationary EMF convergence is pushed further polewards.

3.4 Responses to Large Mountains

Figure 3.5 shows that the stationary EMF convergence, the transient EMF convergence and the friction all have substantial responses in the experiments with large ($H \geq$1km) mountains, while the changes in the mean momentum flux convergence are small. The following subsection discusses the responses of the torque and the stationary EMF convergence in these experiments and then subsection 3.4.2 describes the responses of the friction and the transient EMF convergence.

3.4.1 Responses of the torque and the stationary EMF convergence

The shapes of the torque and of the stationary EMF convergence are essentially unchanged as H is increased (bottom two panels in the left column of Figure 3.5), though both quantities increase more slowly than the H^2 scaling expected from linear theory (see also Figure 2.8).

In order to investigate the effects of the increased meridional propagation in the non-linear regime, Figure 3.6 plots the maximum mountain torque versus the maximum stationary EMF convergence. The maximums are plotted rather than the integrals of these terms because the stationary EMFs decelerate the flow at low lati-

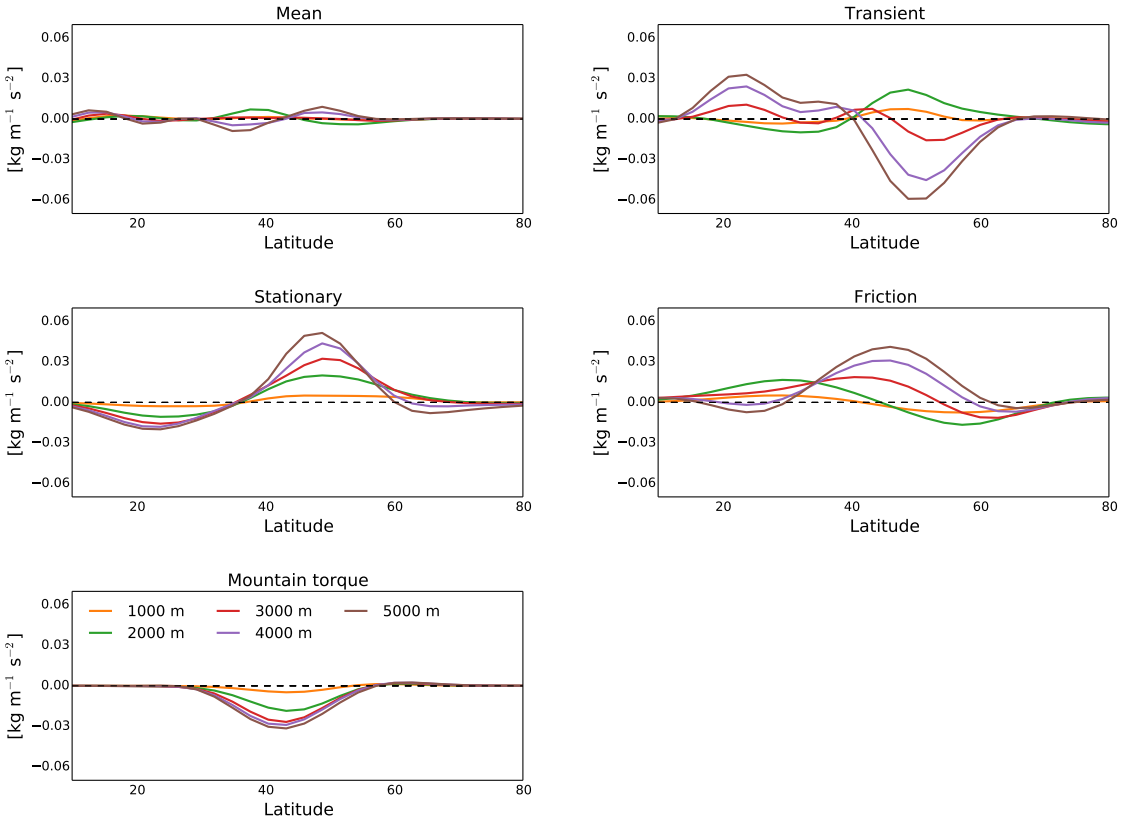


Figure 3.5: Responses of the terms in the momentum budget (equation 3.9) to mountains with $H \geq$1km.

tudes, where the torque is zero. As the inset shows, for small H the torque and the stationary EMF convergence nearly follow a one-to-one line; though the stationary EMF convergence is slightly larger, as was mentioned in section 3.3. However, the stationary EMF convergence increases much faster than the mountain torque for H larger than 1km, so that when $H = 5$km the maximum stationary EMF convergence is about 60% larger than the maximum torque. This confirms the hypothesis made in the introduction to this chapter that the increased meridional propagation of the stationary waves in the non-linear regime results in a larger stationary EMF convergence relative to the torque. This extra stationary EMF convergence must be compensated by the responses of the friction and of the transient EMF convergence.

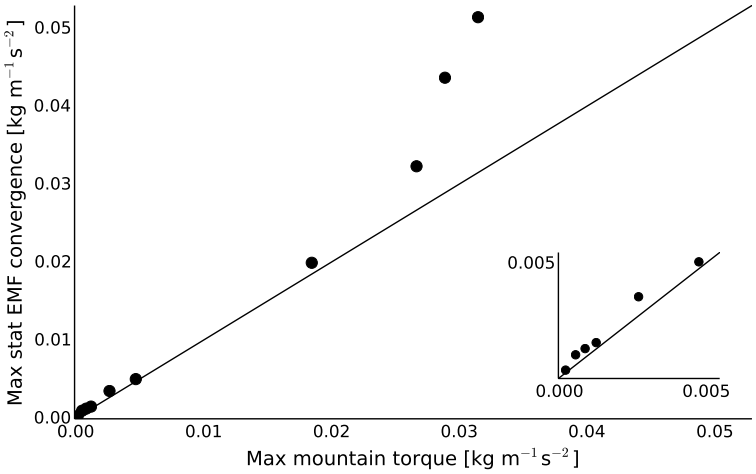


Figure 3.6: The maximum stationary EMF convergence versus the maximum mountain torque for the experiments with the GCM. The straight line plots a one-to-one fit and the inset shows a close-up of the six smallest mountains ($H \leq$1km).

3.4.2 Responses of the friction and the transient EMF convergence

In the H = 1km and H = 2km experiments there is increased transient EMF convergence north of the mountain and decreased convergence to the south, while the response of the friction is positive to the north and negative to the south (right panels of Figure 3.5). These represent a poleward shift of the mid-latitude jet, hints of which can be seen in the experiments with smaller mountains, though the sampling error makes it difficult to robustly distinguish this (not shown). In the H = 4km and H = 5km experiments the jet shifts equatorwards, so the transient EMF convergence is reduced north of the mountain and increased south of the mountain, and the response of the friction is positive to the north and negative to the south. The H = 3km is intermediate between the 2km and the 4km experiments, though there is a slight equatorward shift of the jet in this case.

To investigate this transition from a poleward jet shift to an equatorward jet shift the temporal evolution of the GCM's response to the orography was studied

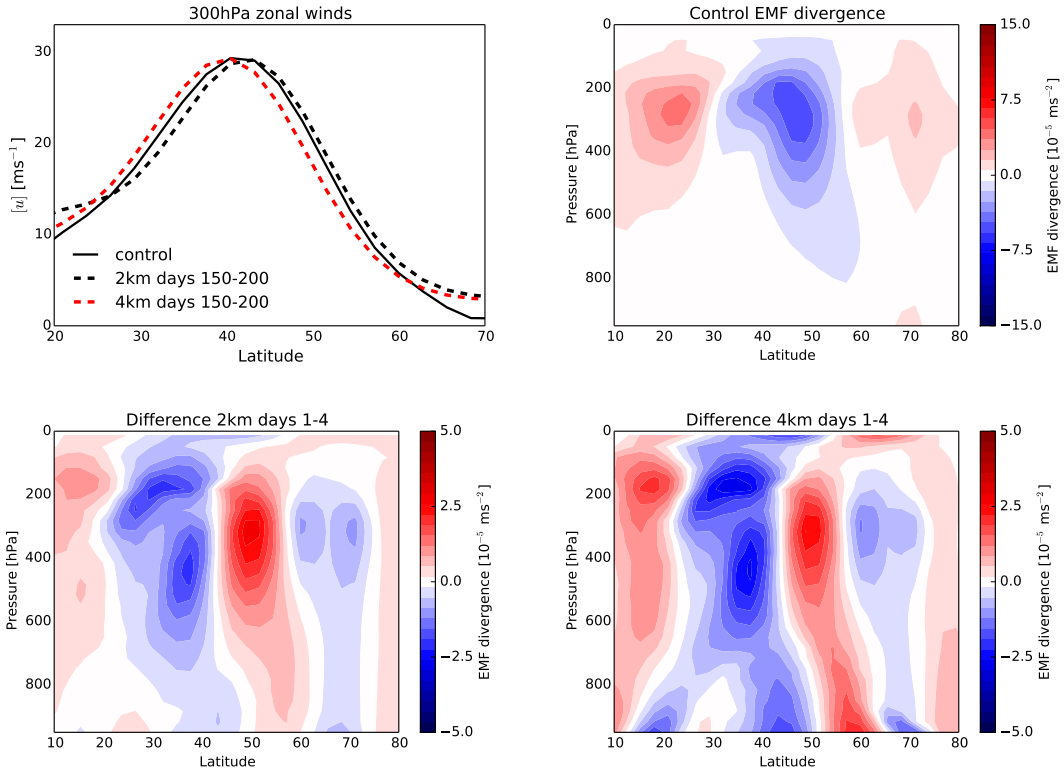


Figure 3.7: Top left panel: 300hPa zonal-mean winds in the control simulation (solid black curve), average ensemble-mean 300hPa winds for days 150-200 from the 2km transient simulations (dashed black curve) and average ensemble-mean 300hPa winds for days 150-200 from the 4km transient simulations (dashed red curve). Top right panel: zonal-mean transient EMF divergence in the control simulation. Bottom left panel: difference between the ensemble-mean transient EMF divergence averaged over the first four days for the transient simulations with $H = 2$km and the control EMF divergence. Bottom right panel: same as the bottom left panel but for the $H = 4$km simulations.

by creating two ensembles of simulations in which orography is abruptly added to the GCM. Each ensemble consisted of 30 simulations lasting 200 days. In one set of simulations an $H = 2$km mountain was added on day 0 while in the other set of simulations an $H = 4$km mountain was added. The initial conditions for each simulation were taken from the control simulation of the GCM and were separated by 100 days to ensure that the ensemble members are independent.

In the ensemble-mean, the jet shifts slightly poleward in the 2km experiments and slightly equatorward in the 4km experiments (top left panel of Figure 3.7). However, in both sets of experiments there is initially EMF convergence equatorward of the mountain and increased EMF divergence poleward of the mountain (bottom two panels of Figure 3.7), indicating that the transient EMF pushes the jet equatorwards for both mountain heights in the first few days after the orography is added.

This suggests that the jet shifts are the result of a competition between the stationary EMF convergence which, as can be seen from Figure 3.5, pushes the jet polewards, and the transient EMF convergence, which initially pushes the jet equatorwards. In the $H = 2$km case the stationary EMF convergence succeeds in pushing the jet polewards and the equilibrated transient EMF then adjusts so as to push the jet further poleward (Figure 3.5). For $H = 4$km the transient EMF convergence on the equatorward flank of the jet is larger than the stationary EMF convergence on the poleward flank of the jet, and the jet shifts equatorwards.

It is not possible to determine why the transient EMFs initially push the jet equatorwards from these experiments, but a possible explanation comes from the lifecycle experiments of Orlanksi (2003), who investigated the influence of low-level baroclinicity on the wave-breaking of baroclinic eddies [84].

Baroclinic eddies can either break cyclonically (cyclonic wave-breaking, CWB) or anti-cyclonically (anti-cyclonic wave-breaking, AWB). CWB tends to occur on the poleward flank of the jet, decelerating the flow there and hence pushing the jet equatorwards, while AWB tends to occur on the equatorward side of the jet, pushing the jet polewards. Orlanski showed that increased low-level baroclinicity results in increased CWB because it strengthens the amplitude of the eddies, which favors CWB. The amplitude of anti-cyclonic eddies is bounded by $-f$, because if the absolute vorticity $\zeta + f$ goes to zero then the stretching term in the vorticity equation, which drives the eddies, also goes to zero. In contrast, the amplitude of

cyclonic eddies is unbounded and so as the amplitude of the eddies increases cyclonic eddies become more prominent, while anti-cyclonic eddies saturate.

Figure 3.8 shows the Eady growth rate (σ_L) at 780hPa for the control experiment with the GCM, the $H = 2$km experiment and the $H = 4$km experiment, where σ_L is calculated as [69]

$$\sigma_L = 0.31 f \frac{\partial u}{\partial z} N^{-1}, \tag{3.12}$$

where z is now the geopotential height. This is taken as a measure of the low-level baroclinicity. As seen by [11] in similar experiments, the low-level baroclinicity is increased directly downstream of the orography and so there is likely to be increased CWB, which would push the jet equatorwards. Confirming this hypothesis would require analyzing the wave-breaking characteristics of the eddies, as well as performing life-cycle calculations.

3.5 Conclusion

This chapter has investigated the zonal-mean response of the GCM to idealized, Gaussian orography, and adds to the literature concerning the response of the atmosphere's momentum budget to orographic forcing. The main results can be summarized as follows:

- For the smallest mountains considered here ($H \leq 10$m) the response of the stationary wave model nearly follows what would be expected from the non-acceleration theorem, as the torque exerted by the mountain on the atmosphere is mostly balanced by the stationary EMF convergence. Friction also plays a role in these experiments, though this effect may be magnified by the strong friction used to keep the stationary wave model steady.

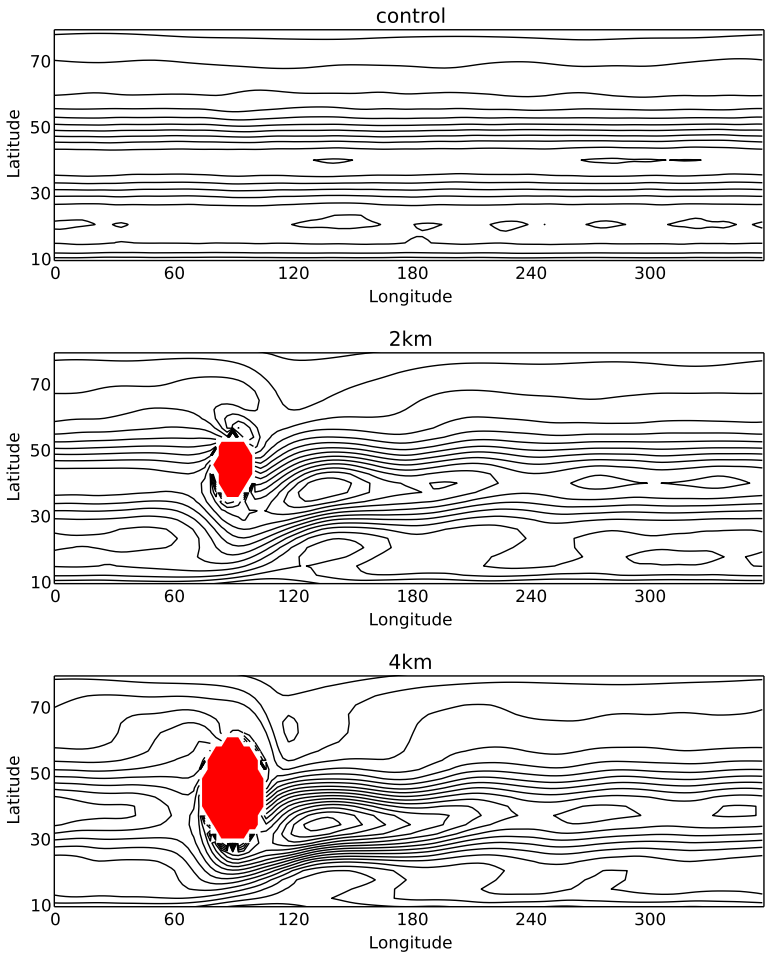


Figure 3.8: Eady growth rate at 780hPa for the control experiment (top panel), the 2km experiment (middle panel) and the 4km experiment (bottom panel). Regions where the mountains intrude into this level are shaded in red. The contour interval is 0.05 days^{-1} in each panel.

- For larger mountains the air increasingly flows around the mountain, rather than simply flowing up and over it, resulting in a stationary non-linearity that induces a second wave activity source poleward of the mountain. Comparing the stationary wave model experiments with the GCM experiments shows that transient eddies also push the stationary EMF convergence polewards of the torque.

- For $H \leq$ 1km the stationary EMF convergence and the torque increase at roughly the same pace in the GCM, but for larger mountains the stationary EMF convergence increases much faster than the torque. This reflects the increased meridional propagation of the stationary wave response in the non-linear regime, and further emphasizes the need to understand the transition from zonal to meridional propagation in the model's response.

- For $H \leq$ 2km the orography causes the mid-latitude jet to shift polewards and also leads to anomalous transient EMF convergence on the poleward side of the jet. Larger mountains cause the jet to shift equatorwards and lead to anomalous transient EMF convergence on the equatorward side of the jet. These shifts seem to be driven by a competition between the stationary EMFs, which always push the jet polewards, and the transient EMFs, which initially push the jet equatorwards. For $H \leq$ 2km the stationary EMFs succeed in pushing the jet polewards and the transient EMFs adjust so that they are larger on the poleward side of the jet, but for the larger mountains the transients cause the jet to shift equatorward, despite the influence of the stationary EMFs.

- A possible explanation for why the transient EMFs push the jet equatorwards is given by the life-cycle experiments of Orlanski (2003). These showed that increased low-level baroclinicity results in increased cyclonic wave-breaking (CWB), which tends to push the jet equatorward. Plots of the low-level Eady growth rate in the GCM experiments confirmed that the baroclinicity is increased downstream of the mountains and so there is likely to be increased CWB, which would be responsible for the anomalous transient EMF convergence equatorward of the jet.

Chapter 4

The Response of Dry Atmospheres to ENSO-like Heating: Superrotation and the Breakdown of Linear Theory

4.1 Introduction

The atmosphere's response to tropical heating has garnered interest from a number of different communities. For instance, it has long been known that convective heating in the west Pacific produces responses far from the heat source via teleconnections [133], and the dynamics of these teleconnections have been extensively investigated (e.g., [114]; [43]; [105]; [124]; [125]; [123]; [87]). In a similar setting, studies of the Madden-Julian Oscillation (MJO) have often focused on the way it is driven by surface latent heat flux anomalies, and contemporary theories for the dynamics of the MJO are built on older theories for the atmosphere's response to stationary tropical heat sources ([6]; [4]; [118]; [2]). Finally, the planetary community has explored the response of

idealized atmospheres to the large-scale (wavenumber one) heating which would be seen on a tidally-locked planet (e.g., [80]; [112]; [113]).

In many of these studies the tropical upper atmosphere's response resembles the response of a linear shallow-water layer to equatorial heating, consisting of an equatorially-trapped Kelvin wave to the east of the heating and Rossby waves propagating away from the equator to the west of the heating. This is the Matsuno-Gill model ([79]; [34]), which has been used in many studies as a starting point for interpreting the results of tropical heating experiments. When necessary, it has also been extended to interpret more complex tropical phenomena (e.g., [112]; [4]; [118]).

In this chapter the linear Matsuno-Gill theory is tested in an idealized, dry general circulation model (GCM) by adding a heat source to the model that mimics the strong diabatic heating in the west Pacific. Just as in the orographic experiments of Chapter 2, the strength of the applied heating is varied in order to isolate a regime in which the model's response is roughly linear in the heating; the aim is to see how well the linear theory can explain the model's response to tropical heating, and over what parameter range the theory is, at least approximately, valid. The strength of the heating is then further increased in order to investigate how the linear response breaks down.

It is found that superrotation, which is when the winds at the equator are westerly, plays a prominent role in the transition from the linear regime to the non-linear regime. Superrotation has been seen in many previous experiments involving tropical heating (e.g., [120]; [104]; [63]; [4]; [112]; [113]) and the atmospheres of Jupiter, Saturn and Titan are all observed to superrotate. The stratosphere also superrotates during the westerly phase of the Quasi-Biennial Oscillation and superrotation has been linked to the "permanent El Nino" state of the tropical Pacific during the Pliocene [128] and may reappear in extreme global warming scenarios [13].

Because it is so common, there is much interest in constructing scenarios in which atmospheric models superrotate. Superrotation was initially studied in idealized, two-

layer models([120]; [104]) and it was found that these systems exhibit hysteresis: the equatorial winds continue to be westerly even when the heating is removed. Hysteresis is also seen in the axisymmetric shallow water model of [110].

Showman and Polvani (2010) demonstrated that a modified form of the Matsuno-Gill model fluxes momentum into the equator and hence can induce superrotation [112]. This theory was verified in a follow-up study in which a heating mimicking that experienced by a tidally-locked exoplanet was applied to an idealized, multi-level GCM [113]. In a similar study, Kraucunas and Hartmann (2005) found that the eddy response to wavenumber two heating of a dry GCM, similar to the one used below, fluxes momentum into the equator, producing superrotation [63]. Analysis of the GCM's momentum budget indicated that the superrotation is limited by the vertical advection of low momentum, near-surface air by the mean tropical circulation. Strengthening the mean circulation by making the equilibrium temperature field hemispherically asymmetric eliminates the superrotation, at least for the heating rates considered by Kraucunas and Hartmann. In a complementary study using a similar set-up, Arnold et al. (2010) showed that a zonally propagating heating mimicking the MJO can also produce superrotation [4].

With the right parameter settings, models can also superrotate without a localized heat source. This is commonly seen for planets that are slowly rotating and/or have small radii; i.e., that have a large (> 1) "thermal Rossby number" [81]. Wang and Mitchell (2014) recently identified a linear instability to explain this result [135], consisting of the interaction between a tropical Kelvin wave and Rossby waves at higher latitudes. By analyzing a mixture of simulations and reanalysis data for Earth and other Solar System bodies, Wang and Mitchell successfully demonstrated that this instability is a necessary (though not sufficient) condition for superrotation in planetary atmospheres with axisymmetric forcing. Finally, [108] and [70] showed that equatorial convection on gas giants can cause superrotation by exciting Rossby waves

in the deep tropics. These waves propagate to higher latitudes, where they break and transfer momentum back to their source, accelerating the equatorial winds. [64] developed a scaling argument for the conditions under which equatorial convection is strong enough to produce superrotation.

The experiments described below are similar to those performed by Kraucunas and Hartmann, though the horizontal extent of the heating is smaller and a much larger range of heating rates is used. This allows the evolution of the response as a function of the heating rate to be studied in detail. The parameters of the model are also varied in order to explore how this affects the response. Strong superrotation is produced when large heating rates are added to a set-up with a relatively weak equator-to-pole temperature gradient.

The model and experiments are described in the following section, after which the results of the experiments with the original Held-Suarez set-up are described in section 4.3 and the dynamics of the superrotation are analyzed in section 4.4. The effects of varying the parameters of the model are discussed in sections 4.5 and 4.6, before the chapter ends with conclusions in section 4.7.

4.2 Model and Experiments

As in Chapter 2, the GCM used in this study is the GFDL spectral dynamical core. This solves the primitive equations, forced by zonally-symmetric Newtonian relaxation to a prescribed equilibrium temperature field and damped by Rayleigh friction near the surface and hyperdiffusion in the divergence equation. To start with the parameter settings are the standard Held-Suarez parameters with forcing symmetric about the equator. The forcing is modified in sections 4.5 and 4.6.

The model was run at T42 resolution with 40 evenly-spaced σ levels. The stronger heatings produce responses that extend into the stratosphere and, although a rela-

tively high vertical resolution is used, the stratospheric responses are likely distorted by the even spacing of the σ levels. It is unclear how this affects the tropospheric responses.

The control simulation consisted of a 40 000 day integration, with the first 2000 days discarded and data sampled once per day. Some experiments were repeated at T85 resolution to confirm that the results are qualitatively the same at higher horizontal resolution, but the focus was on generating long integrations, rather than high resolution integrations, so that the linear regime could be isolated within this particular model.

In the perturbation experiments an equatorial heat source was added to the temperature equation

$$\frac{\partial T}{\partial t} = ... + Q,$$

with the form

$$Q(p, \phi, \lambda) = Q_0 sin\left(\frac{p - p_t}{p_b - p_t}\pi\right) \exp\left\{-\left[\frac{\phi^2}{w_1^2} + \frac{(\lambda - \lambda_0)^2}{w_2^2}\right]\right\} \tag{4.1}$$

where Q_0 is the maximum heating rate; p, ϕ and λ are pressure, latitude and longitude, respectively; and w_1 and w_2 are half-widths. p_t was set to 200hPa, p_b to 800hPa, w_1 to 20°, λ_0 to 150° and w_2 to 30°. The horizontal extent of the heating was taken to roughly mimic the region of strong diabatic heating in the west Pacific, where the maximum column-averaged heating is roughly 1.5K/day (e.g., Figure 8 of [49]). Some of the experiments were repeated with the zonal-mean heating removed, and these are discussed briefly in section 4.3.2.

Q_0 was varied from 0.1K/day to 7.5K/day. The responses to smaller heating rates were not clearly separable from the noise. For comparison, the largest heating applied by Arnold et al. was 0.9K/day and the heating applied by Kraucunas and Hartmann was 1 K/day. For heating rates less than 0.5K/day the responses were

Table 4.1: List of experiments performed with the Held and Suarez set-up. Δ_y is the equator-to-pole temperature difference in the equilibrium temperature profile.

Q_0 (K/day)	Length (days)	Resolution	Δ_y	Repeated with no zonal-mean heating?
0	40 000/20 000	T42/T85	40K/60K/80K	n.a
0.1	40 000	T42	60K	N
0.15	40 000	T42	60K	N
0.2	40 000/20 000	T42/T85	40K/60K/80K	Y
0.25	40 000	T42	60K	N
0.5	40 000/20 000	T42/T85	40K/60K/80K	Y
0.75	20 000	T42	60K	N
1	20 000/20 000	T42	40K/60K/80K	Y
2	20 000/20 000	T42/T85	40K/60K/80K	Y
3	20 000	T42	60K	N
4	20 000/20 000	T42/T85	40K/60K/80K	Y
5	20 000	T42	60K	N
7.5	20 000/20 000	T42/T85	40K/60K/80K	N

obtained by integrating the model for 40 000 days, discarding the first 2000 days of each experiment and then averaging over the rest of the days. Experiments with larger heating rates were only run for 20 000 days as the response emerges more quickly. The T85 simulations were also run for 20 000 days. A complete list of experiments with the Held and Suarez set-up is given in Table 4.1.

4.3 Responses to Heating

4.3.1 Eddy streamfunction and zonal-mean wind responses

The top left panel of Figure 4.1 shows the eddy streamfunction response at 350hPa for the $Q_0 = 0.2$K/day case. The GCM's response is approximately linear for $Q_0 <$ 0.5K/day (see next subsection) and the 0.2K/day case is taken as a representative example of the response in this regime.

The response resembles that of the Matsuno-Gill model and consists of an equatorially-trapped Kelvin wave and a Rossby wave in each hemisphere which

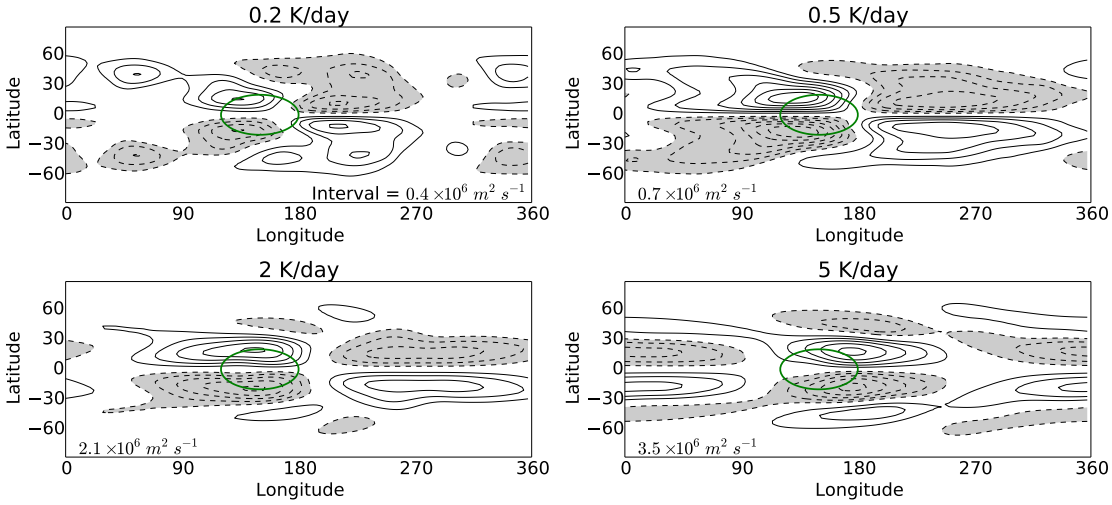


Figure 4.1: Eddy streamfunction response at 350hPa for $Q_0 = 0.2$K/day (top left), 0.5K/day (top right), 2K/day (bottom left) and 5K/day (bottom right). The contour intervals are written on the panels, negative values are shaded and the green ovals show the $Q_0/2$ contour. The responses have been symmetrized about the equator to reduce the sampling error.

propagates meridionally away from the source. The maximum response is also shifted west of the maximum heating, as predicted by linear theory. The vertical profile of the response to $Q_0 = 0.2$K/day is shown in the top left panel of Figure 4.2. The response in the vicinity of the heating consists of a strong anti-cyclone in the upper troposphere, centered at about 250hPa, and a weaker cyclone in the lower troposphere, centered at about 600hPa. Away from the source the Kelvin wave can be seen propagating with an eastward phase tilt with height, eventually extending into the stratosphere, where it is damped out.

For $Q_0 = 0.5$K/day the Kelvin wave dominates the response at 350hPa (top right panel of Figure 4.1), and then the Rossby wave becomes increasingly prominent for larger Q_0 (bottom panels of Figure 4.1). The wavenumber of the waves decreases with Q_0 and so does the normalized amplitude, as can be inferred from the contour intervals. The response also shifts eastward so that its maximum is east of the maximum heating rate for large Q_0. In fact, the responses in these cases, dominated by

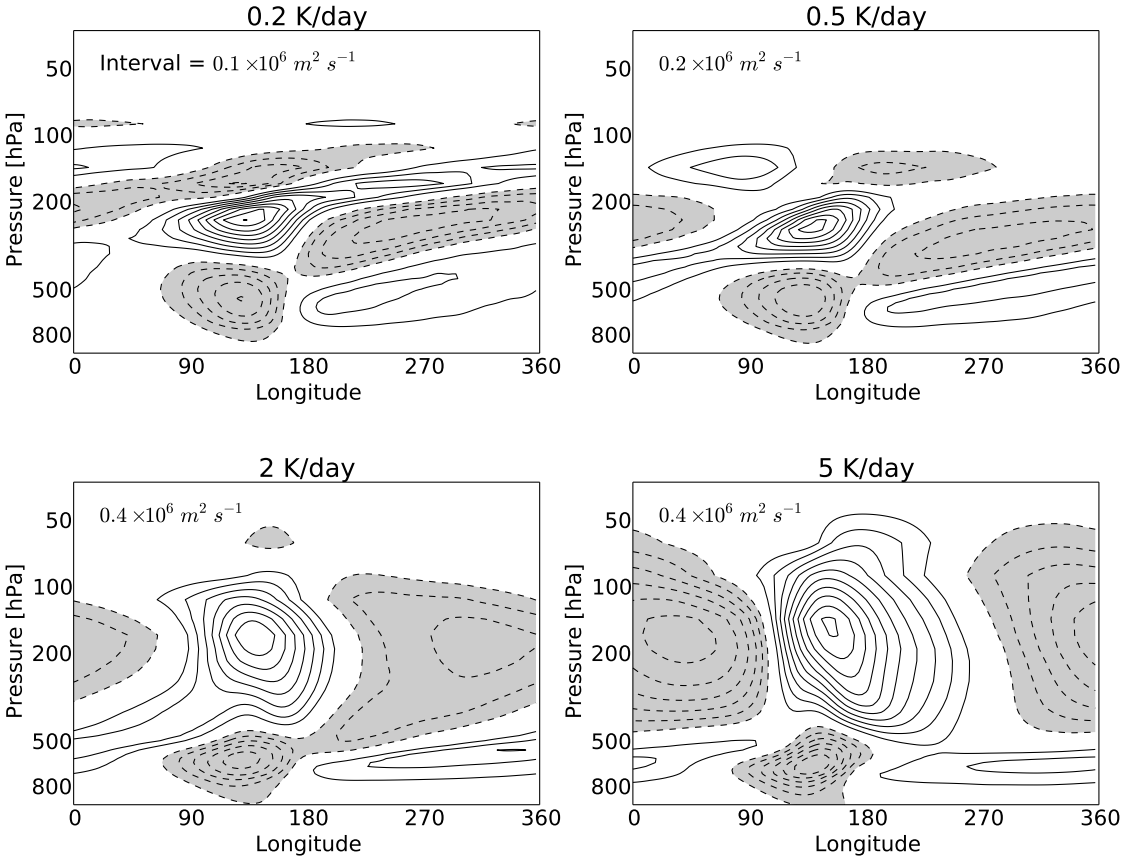


Figure 4.2: Eddy streamfunction response at 2°N to equatorial heating for Q_0 = 0.2K/day (top left), 0.5K/day (top right), 2K/day (bottom left) and 5K/day (bottom right). The contour intervals are written on the panels.

the Rossby wave, are similar to the response of a superrotating barotropic model to tropical heating seen by [105]. [50] found that the response of a two-level primitive equation model to tropical heating also shifts eastward for strong forcings.

The vertical structure of the response is similar in the 0.2K/day and 0.5K/day cases, but then changes for larger Q_0 (bottom panels of Figure 4.2). In these cases the response in the upper troposphere consists of a wavenumber one wave that extends into the stratosphere. The maximum response is at about 175hPa and also shifts eastward as Q_0 is increased. The response in the lower troposphere is at roughly the same height as in the experiments with weak heating and does not shift in longitude, so the

response in the vicinity of the heating increasingly tilts to the east with height. The Kelvin wave is still visible away from the forcing in the lower- and mid-troposphere, but it is blocked from propagating into the upper troposphere.

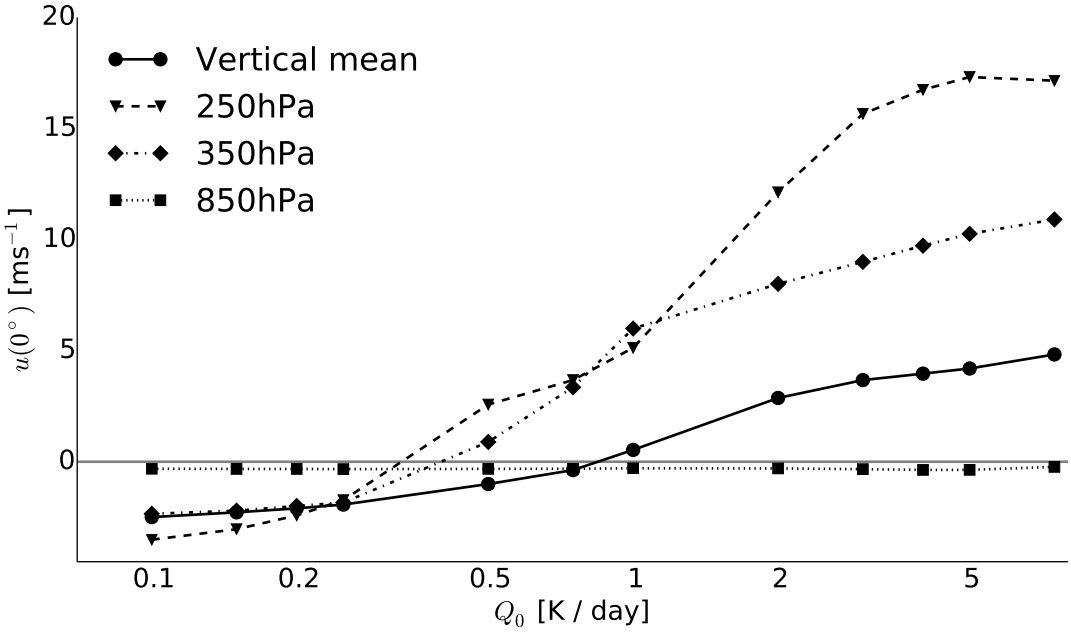


Figure 4.3: Equatorial zonal-mean zonal wind as a function of Q_0. Circles show the vertical-mean wind, triangles show the wind at 250hPa, diamonds show the wind at 350hPa and squares show the wind at 850hPa. Note the logarithmic scale for the x-axis.

In addition to these eddy responses, the zonal winds at the equator accelerate as Q_0 is increased (Figure 4.3, note that there are no gridpoints at the equator and so equatorial values are obtained by averaging the values on either side of the equator). In fact, the flow superrotates at upper levels for $Q_0 = 0.5$K/day and the vertically-averaged winds are superrotating for $Q_0 = 1$K/day and above. The acceleration continues until $Q_0 = 4$K/day, after which the winds saturate.

4.3.2 Vorticity budget analysis

Because the Coriolis force is weak in the tropics, tropical diabatic heating is primarily balanced by vertical motion acting on the static stability. This corresponds to the weak temperature gradient approximation of the thermodynamic equation [117]

$$\omega^* N^2 \approx -Q, \tag{4.2}$$

where ω^* is the stationary eddy pressure velocity (dp/dt) and N^2 is the static stability. Substituting into the continuity equation then shows that heating induces a large-scale horizontal divergence

$$\nabla \cdot \bar{\mathbf{v}}^* \approx \frac{\partial}{\partial p}\left(\frac{Q}{N^2}\right), \tag{4.3}$$

which in turn drives rotational flow through the vortex stretching term in the stationary eddy vorticity equation:

$$\begin{aligned} 0 = &- [\bar{u}]\frac{1}{acos\phi}\frac{\partial \bar{\zeta}^*}{\partial \lambda} - \left(\beta + \frac{1}{a}\frac{\partial [\bar{\zeta}]}{\partial \phi}\right)\bar{v}^* - \left(f + [\bar{\zeta}]\right)\nabla \cdot \bar{\mathbf{v}}^* - \nabla \cdot \left(\bar{\zeta}^* \bar{\mathbf{v}}^*\right)^* \\ &- \nabla \cdot \left(\overline{\zeta' \mathbf{v}'}\right)^* - \hat{\mathbf{k}} \cdot \nabla \times \overline{\omega \frac{\partial \mathbf{v}}{\partial p}}^*, \end{aligned} \tag{4.4}$$

where a is the radius of the earth, [] denotes a zonal-mean, $\bar{}$ denotes a time-mean, * denotes a departure from the zonal-mean and $'$ denotes a transient term. The stretching term is the third term on the right hand side. The first two terms represent the linear advection of eddy vorticity by the zonal-mean zonal wind and the linear advection of mean vorticity by the eddy meridional wind, respectively. The fourth term is the non-linear flux divergence of eddy vorticity and the fifth term is the transient flux divergence of eddy vorticity. Finally, the sixth term is the creation of vorticity by twisting and vertical advection.

The linear response of the Matsuno-Gill model essentially consists of a Sverdrup balance between the second and third terms; that is, between the meridional advection

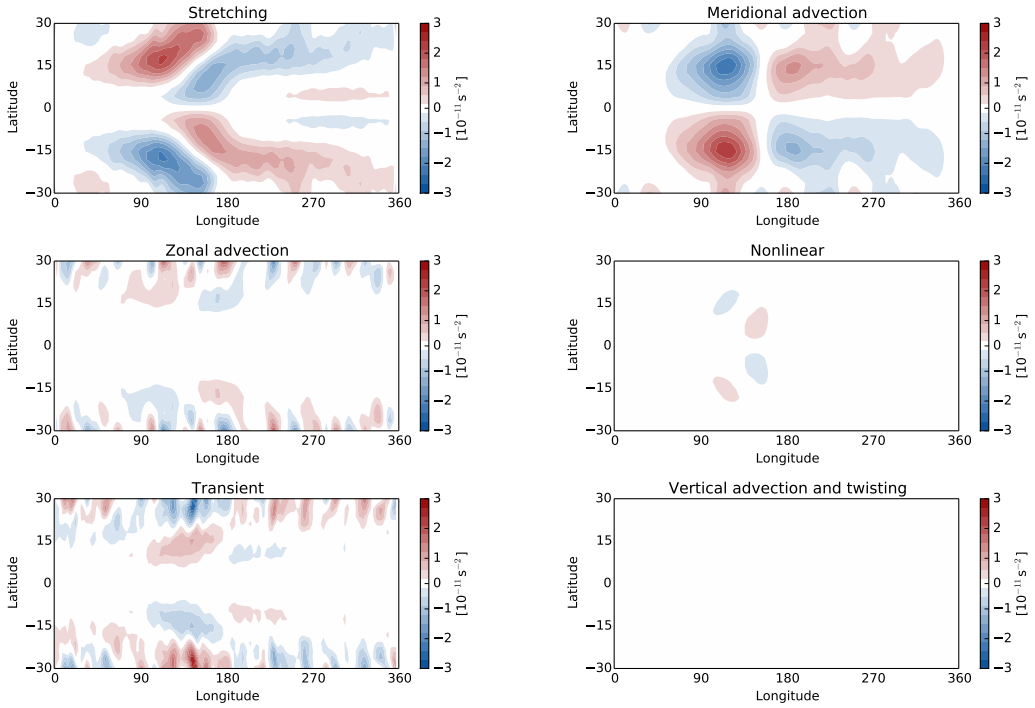


Figure 4.4: Vorticity balance for the $Q_0 = 0.2$K/day experiment. The terms are defined in equation 2.5 and the text below.

term and the stretching. In Figure 4.4 it can be seen that these terms do make up the majority of the eddy vorticity budget in the tropics of the small Q_0 simulations, with transients also playing a role. The budget is quite noisy in the extra-tropics.

To quantify how the terms in the budget change as a function of Q_0, the Root-Mean-Square (RMS) values of the terms in equation 4.4 at 250hPa between -20° and 20° are shown in Figure 4.5 as a function of Q_0. The results are similar using other latitude bounds and at other heights. For $Q_0 < 0.5$K/day the stretching term and the meridional advection term increase approximately linearly, and track each other very closely, confirming that the GCM is behaving linearly in this parameter range. As Q_0 is increased the meridional term saturates, though it remains the largest term in the budget. In contrast, the stretching term increases more slowly between $Q_0 = 0.5$K/day and $Q_0 = 1$K/day, and then actually decreases between $Q_0 = 1$K/day and

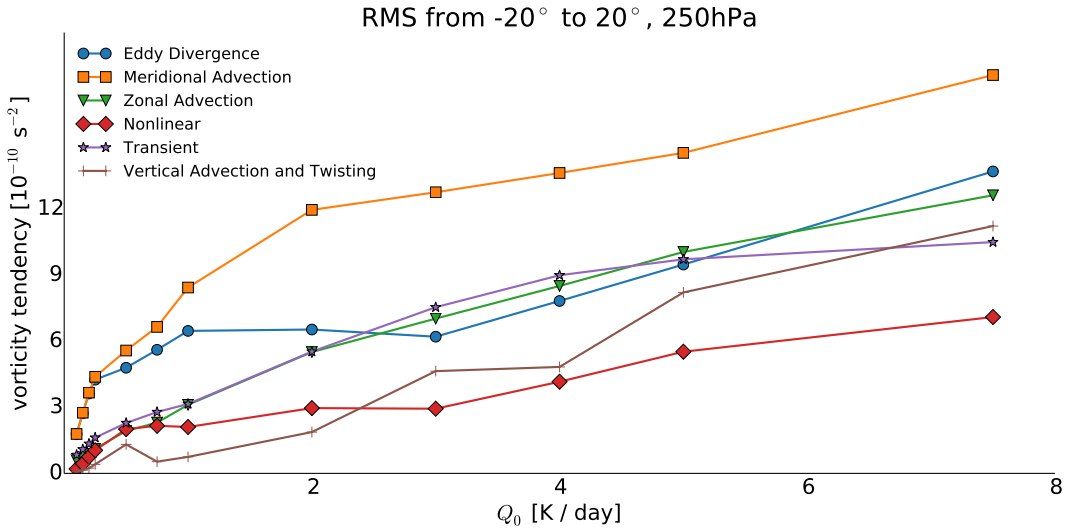


Figure 4.5: Root-Mean Square (RMS) of the terms in the vorticity budget at 250hPa between $-20°$ and $20°$ as a function of Q_0. Note the logarithmic scale for the x-axis.

$Q_0 = 3$K/day, before increasing again. As a result, the contributions of the zonal advection term and the transient term, which both become more prominent as Q_0 is increased, are comparable to the contribution of the stretching term for $Q_0 \geq 2$K/day.

The non-monotonic behavior of the stretching term is driven by changes in the divergence, as changes in the zonal-mean absolute vorticity are small (not shown). Laraia and Schneider (2015) give an expression for the scaling of the divergence in equation 4.3 as [64]

$$\nabla \cdot \bar{\mathbf{v}}^* \sim \frac{gQ_0}{\theta_0 H_t N^2}, \tag{4.5}$$

where g is the gravitational acceleration, θ_0 is a reference potential temperature and H_t is the tropopause height. Since the divergence does not increase linearly for $Q_0 \geq 0.5$K/day, H_t and/or N^2 must be increasing. These two quantities are shown in Figure 4.6 for the control case and for four heating experiments. Clearly it is the static stability which causes the divergence to depart from a linear scaling, as the heating stabilizes the tropical mid-troposphere, while the tropopause height is essentially constant. As discussed by [63], localized heating stabilizes the tropics by increasing

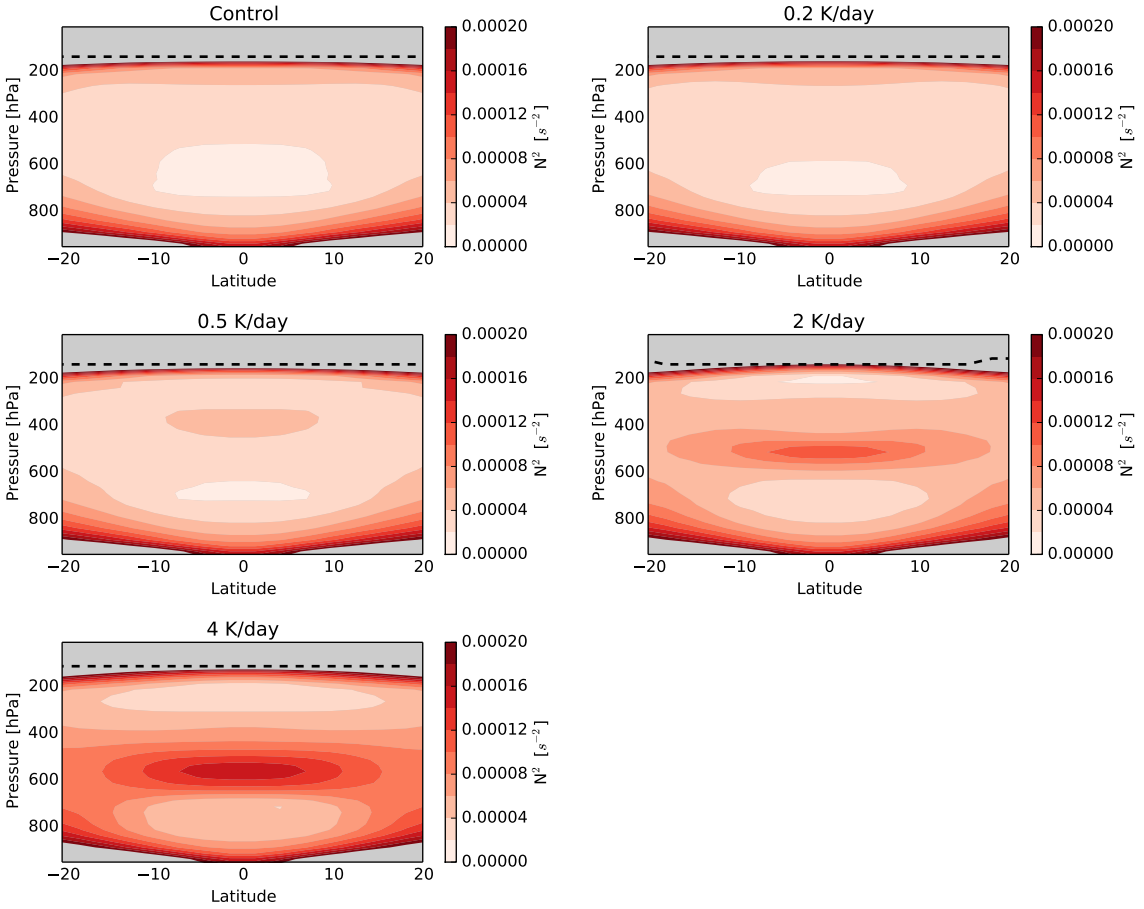


Figure 4.6: Tropical static stability for the control experiment (top left) and the experiments with $Q_0 = 0.2$K/day (top right), 0.5K/day (center left), 2K/day (center right) and 4K/day (lower left). The dashed black lines show the tropopause heights in these experiments, with the tropopause defined as the pressure at which $\partial T/\partial z$ is less than 2Kkm^{-1}. Regions in which the static stability is outside the colorbar scale are shaded in gray.

the vertical wind shear in the upper troposphere, which causes temperatures there to increase in order to keep thermal wind balance (top panel of Figure 4.7); and by converging heat into the tropical mid-troposphere via the stationary vertical eddy heat flux (lower panel of Figure 4.7). In Figure 4.6 it can be seen that the layer of high stability that is created by the stationary eddy heat flux descends in the troposphere as Q_0 is increased, reflecting a change in the vertical structure of the response. The reason for the increased vertical wind shear is discussed in the next section.

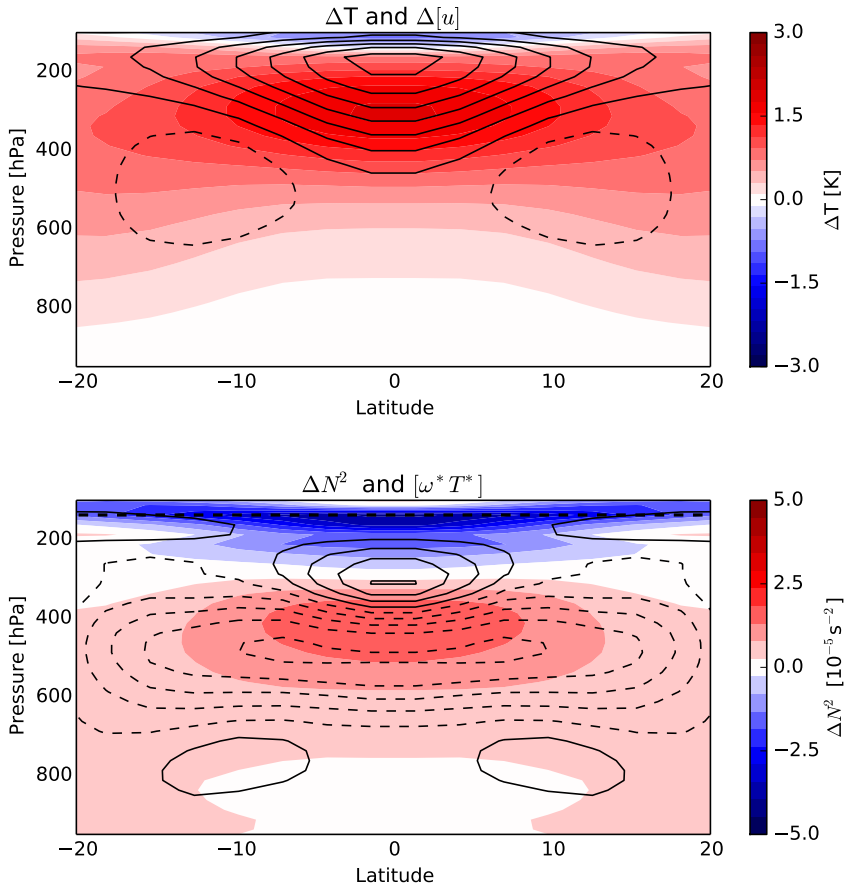


Figure 4.7: Top panel: zonal mean temperature change (colors) and change in the zonal-mean winds (black contours, with contour interval 0.1ms^{-1} and negative contours dashed) between the $Q_0 = 0.5$K/day experiment and the control experiment. Bottom panel: change in the static stability between the 0.5K/day experiment and the control experiment (colors) and the zonal-mean stationary vertical eddy heat flux in this experiment (black contours, with contour interval 0.002 KPas^{-1} and negative contours dashed).

Figure 4.8 repeats Figure 4.5, but plots the terms in the vorticity budget for the experiments with the zonal-mean heating removed. The progression is very similar, but the magnitude of the stretching term is larger because the tropical static stability increases more slowly and so the divergence increases more rapidly with Q_0. The responses have the same structure as in the cases with net zonal-mean heating (not shown).

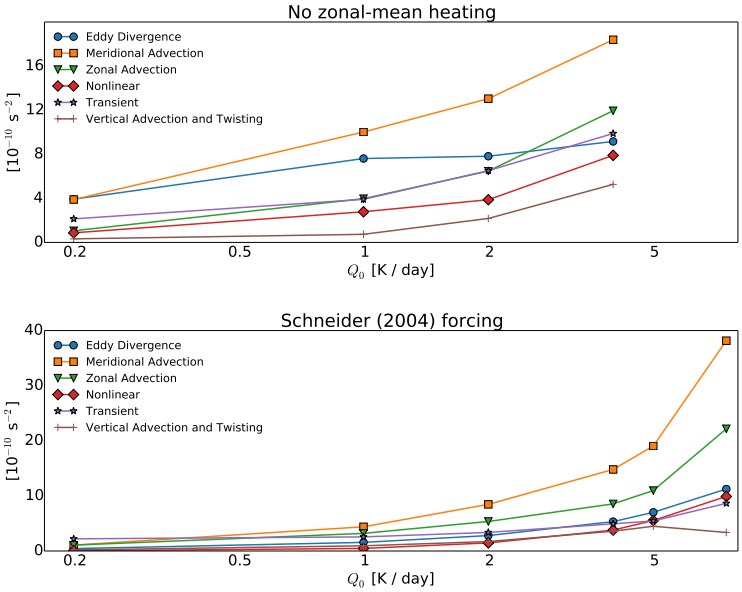


Figure 4.8: Same as Figure 4.5 but for the cases with no zonal-mean heating (top panel) and the cases with the Schneider (2004) forcing (bottom panel).

To summarize this section, the GCM's response is approximately linear for $Q_0 < 0.5$ K/day and resembles what would be expected from the Matsuno-Gill model. For larger values of Q_0 the Sverdrup balance making up the Matsuno-Gill model breaks down as the stretching term becomes relatively weaker because of the increased stability of the tropical atmosphere. At the same time, the equatorial winds accelerate and begin to superrotate, breaking the assumption of the Matsuno-Gill model that the tropics are quiescent. However, the linear regime appears to break down because of the increased stability before the superrotation can influence the response. The next section analyzes the zonal-momentum budget in order to understand the reasons for the transition to superrotation.

4.4 Zonal Momentum Budget

The steady-state zonal-mean momentum budget is

$$
\begin{aligned}
0 = & f[\bar{v}] - \frac{[\bar{v}]}{a cos\phi}\frac{\partial}{\partial\phi}\left([\bar{u}]cos\phi\right) - [\bar{\omega}]\frac{\partial[\bar{u}]}{\partial p} - \frac{1}{acos^2\phi}\frac{\partial}{\partial\phi}\left([\bar{u}^*\bar{v}^*]cos^2\phi\right) \\
& - \frac{\partial}{\partial p}[\bar{u}^*\bar{\omega}^*] - \frac{1}{acos^2\phi}\frac{\partial}{\partial\phi}\left([\overline{u'v'}]cos^2\phi\right) - \frac{\partial}{\partial p}[\overline{u'\omega'}] + [\bar{F}_x],
\end{aligned}
\tag{4.6}
$$

where F_x is the frictional drag in the zonal direction. The vertical Coriolis term, the metric terms and the hyperdiffusion have been ignored.

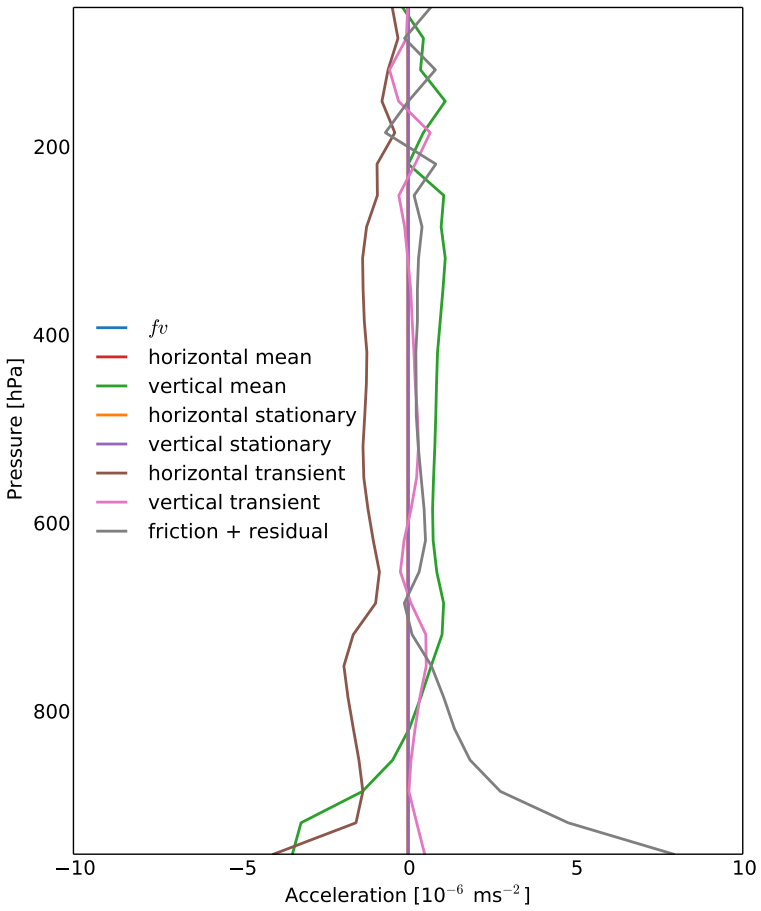


Figure 4.9: Vertical profile of the zonal momentum budget at the equator for the control experiment. The terms are defined in equation 4.6 and the text below.

The vertical profiles of the terms in the budget at the equator are shown for the control simulation in Figure 4.9. Outside of the boundary layer, the dominant balance is between the vertical advection of air by the Hadley circulation, which accelerates the flow, and the divergence of momentum by horizontally propagating transient eddies, which decelerates the flow. This is the same balance seen by [64].

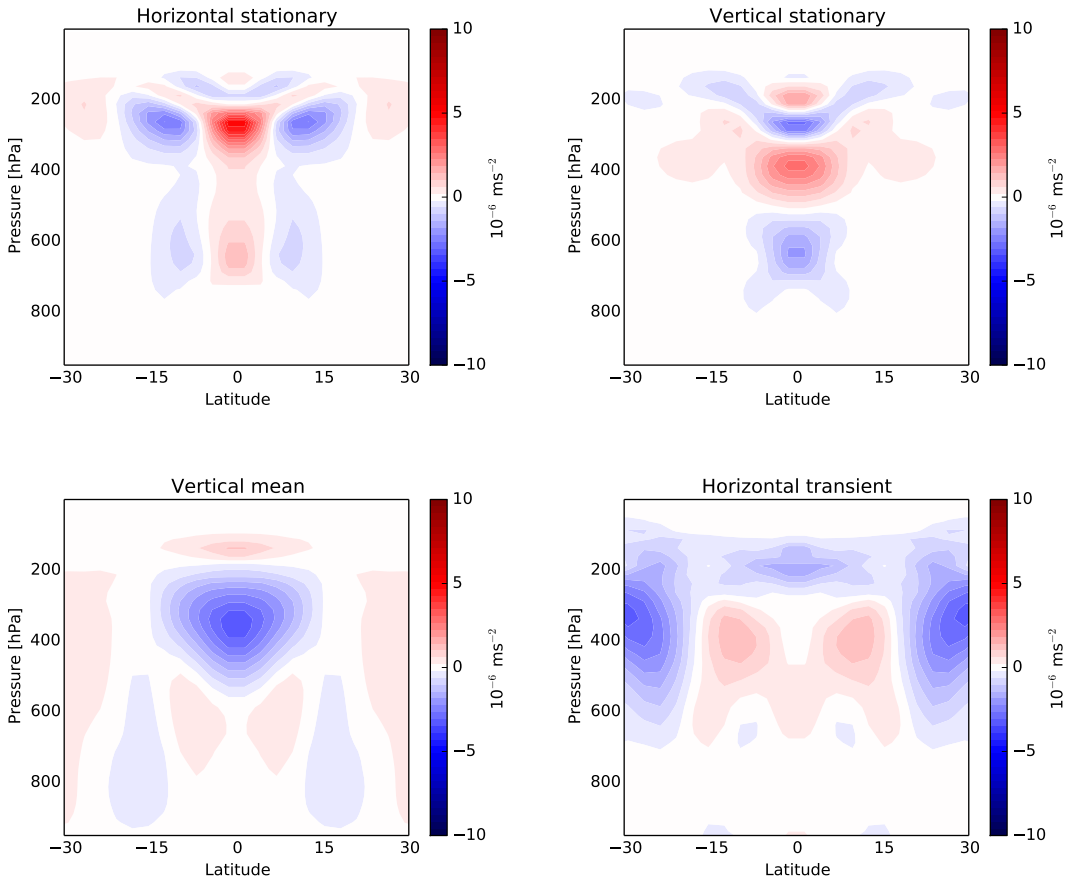


Figure 4.10: Latitude-pressure cross-sections of the responses of the vertical mean (top left panel), horizontal stationary (top right panel), vertical stationary (bottom left panel) and horizontal transient (bottom right panel) terms in the zonal momentum budget for $Q_0 = 0.5$K/day.

Figure 4.10 shows the response of the momentum budget in the tropics for Q_0 = 0.5K/day. The changes in fv, the mean horizontal term, the transient vertical term and the friction (outside the boundary layer) are small and so these are not

shown. The stationary horizontal term transfers momentum from the subtropics into the equator, with two maxima, one at about 250hPa and one at about 650hPa (top left panel). These are the heights at which the eddy streamfunction response is largest (Figure 4.2). The stationary vertical term cannot cause a vertical-mean acceleration of the flow [94], but it redistributes momentum vertically: there are minima at the equator close to the heights of the maxima in the stationary horizontal EMF and a maximum in the mid-troposphere. Hence the stationary wave transfers momentum from the subtropical upper- and lower-troposphere into the equatorial mid-troposphere.

This acceleration is opposed by the vertical mean term, which decelerates the flow by bringing up low momentum air from near the surface. This deceleration is largest at about 350hPa. The transients weakly decelerate the flow at about 200hPa and accelerate the flow at lower altitudes.

As discussed in the previous section, the largest acceleration takes place in the upper troposphere and so the vertical wind shear increases. Examining the transient evolution of the zonal winds in the perturbation experiments reveals that initially the stationary wave causes a large acceleration of the equatorial winds in the mid-troposphere, as the horizontal stationary flux transfers momentum into the equatorial upper and lower troposphere and the vertical stationary term transfers this to the mid-troposphere. After 10-20 days the mean vertical term adjusts, however, and counters the acceleration in the mid-troposphere. The residual acceleration is largest in the upper troposphere (Figure 4.7).

Profiles of the responses of the terms in the equatorial momentum budget are shown for several values of Q_0 in Figure 4.11, with the changes normalized by $1/Q_0$. The stationary horizontal EMF convergence is similar in the 0.2K/day and the $Q_0 =$ 0.5K/day cases, with a sharp peak at about 250hPa and a broader peak in the lower troposphere centered at about 650hPa. The upper tropospheric peak is slightly lower

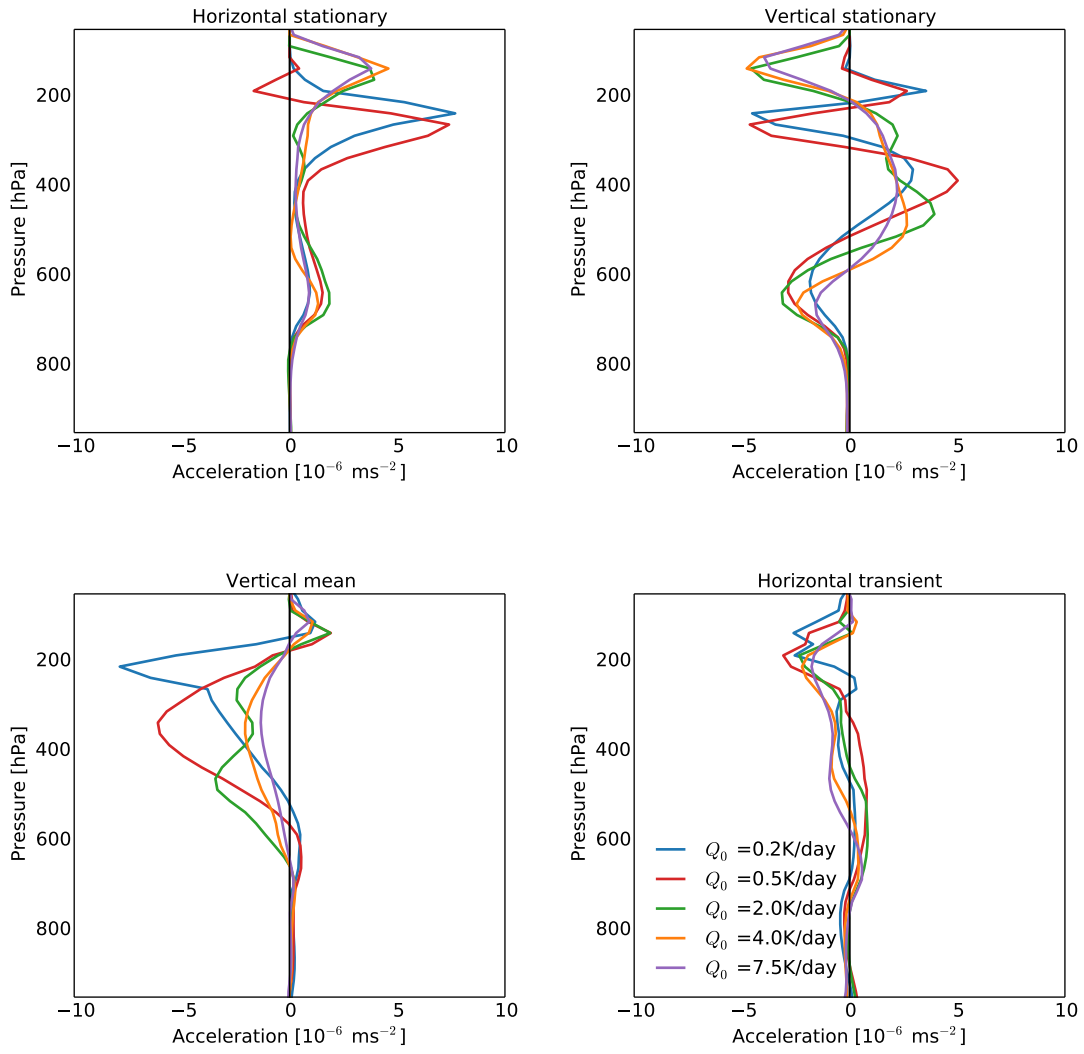


Figure 4.11: Responses of the vertical mean, horizontal stationary, vertical stationary and horizontal transient momentum fluxes to $Q_0 = 0.2$K/day (blue), 0.5K/day (red), 2K/day (green), 4K/day (orange) and 7.5K/day (purple). The curves have been normalized by $1/Q_0$.

in the 0.5K/day case and close inspection of Figure 4.2 shows that the maximum eddy streamfunction response in this case is also at a slightly lower altitude in the upper troposphere. The upper tropospheric peak in the stationary horizontal EMF convergence is relatively weaker for larger heating rates, though it has approximately the same magnitude for $Q_0 = 2$K/day to $Q_0 = 7.5$K/day, and is shifted up to about

175hPa. This upward shift reflects the deepening of the response into the stratosphere seen in Figure 4.2. In the lower troposphere the maximum stays at roughly the same height and has roughly the same normalized magnitude in all cases.

The changes of the stationary vertical term mirror those of the stationary horizontal term. For $Q_0 = 0.2$ and 0.5K/day the stationary vertical flux decelerates the flow between about 300 and 200hPa and between 700 and 500hPa, and accelerates the flow in between, as well as between about 200 and 150hPa. For the larger heatings the region of deceleration in the upper troposphere moves upwards and is between about 200hPa and 50hPa and the region of acceleration expands from about 600hPa to 200hPa. In all of the experiments then, the stationary vertical term transfers the momentum fluxed into the equatorial upper and lower troposphere by the horizontal stationary term into the mid-troposphere.

The mean vertical term is fairly similar across the different experiments, except that its normalized amplitude decreases as Q_0 is increased. This is because the wind shear does not increase substantially for $Q_0 > 0.5$K/day. The altitude of the maximum deceleration descends as Q_0 is increased, from a sharp peak at about 200hPa for $Q_0 = 0.2$K/day to a smoother maximum at about 350hPa in the large Q_0 experiments.

The transient horizontal term is roughly linear in Q_0 and this term generally acts to accelerate the flow in the lower to mid-troposphere and decelerate the flow in the upper troposphere. However, as Q_0 increases the transition from acceleration to deceleration descends, so that the transient eddies decelerate the flow more strongly in the vertical mean. This is made clearer in Figure 4.12, which plots the vertical integrals of the stationary horizontal EMF convergence, the transient horizontal EMF convergence and the sum of the two as a function of Q_0. The integral of the stationary horizontal EMF convergence increases monotonically with Q_0, though the rate of increase decreases for $Q_0 \geq 0.5$K/day, while the integral of the transient horizontal term is essentially zero until $Q_0 = 2$K/day, after which it increases rapidly and so the

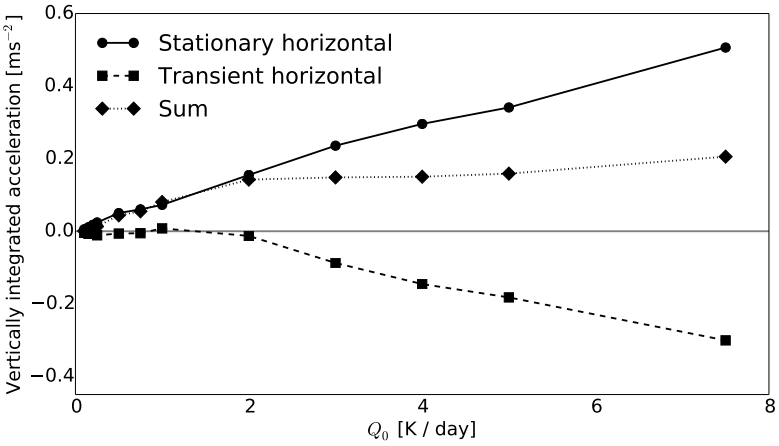


Figure 4.12: Vertical integral of the normalized equatorial stationary horizontal EMF convergence as a function of Q_0 (circles), the integral of the transient horizontal EMF convergence (squares) and the sum of the two (diamonds).

sum of these two terms is roughly constant for $Q_0 \geq 2$K/day (note that the sum is mostly balanced by the vertical mean term and the friction).

This result contrasts with previous studies, such as [63], which have found the mean vertical term to be the only negative feedback on the superrotation. Here the mean vertical term saturates with Q_0 and so the horizontal transient term becomes important for large heating rates. This term becomes important because the acceleration of the winds in the deep tropics allows eddies originating in mid-latitudes to penetrate deeper into the tropics and break closer to the equator, transferring more momentum from the deep tropics to the extra-tropics. I attribute this difference to the larger heating rates used here. Note that this is the opposite of what happens in the two-level model of Saravanan; in that model the tropics become entirely transparent to baroclinic eddies, which pass into the opposite hemisphere without impacting the equatorial flow.

4.5 Varying the Baroclinicity

Stronger (weaker) baroclinicity at mid-latitudes leads to stronger (weaker) transient EMFs and also to a stronger (weaker) Hadley circulation, altering the momentum balance of the GCM. To investigate how the results of the previous sections are affected by this, new sets of experiments were performed with the equator-to-pole temperature difference in the equilibrium temperature profile, Δ_y, set to 40K and with Δ_y set to 80K. In the original Held and Suarez set-up Δ_y is 60K.

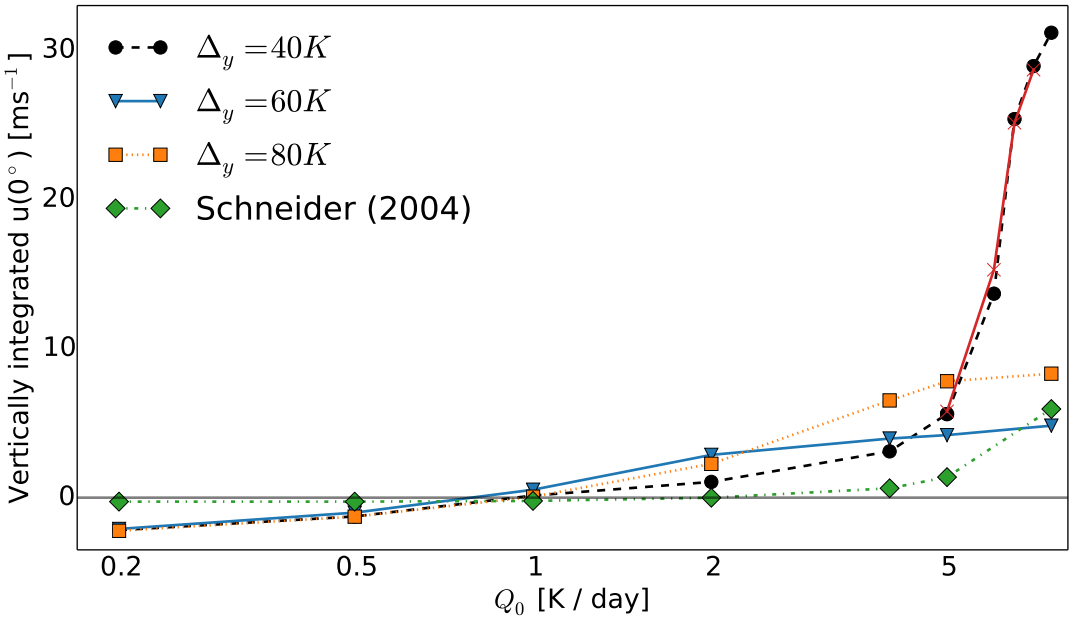


Figure 4.13: Vertical-mean equatorial zonal-mean zonal wind as a function of Q_0 for Δ_y = 80K (circles), Δ_y = = 60K (triangles), Δ_y = = 40K (squares) and with the Schneider (2004) [106] set-up (diamonds). The red crosses show the experiments run with Δ_Y = 40K initialized with the final state from the Q_0 = 7.5K/day experiment.

In the experiments with Δ_y = 80K the responses are very similar to the original cases, but somewhat weaker. For this reason, and because of the stronger Hadley circulation, the vertical-mean zonal winds initially accelerate more slowly as Q_0 is increased (orange squares in Figure 4.13); however they keep accelerating and are actually stronger when Q_0 = 4K/day than they are in the corresponding Δ_y = 60K

case. A similar analysis to section 4.3.2 reveals that the tropical static stability increases more slowly in this set-up as Q_0 is increased and so the stationary wave response also saturates more slowly.

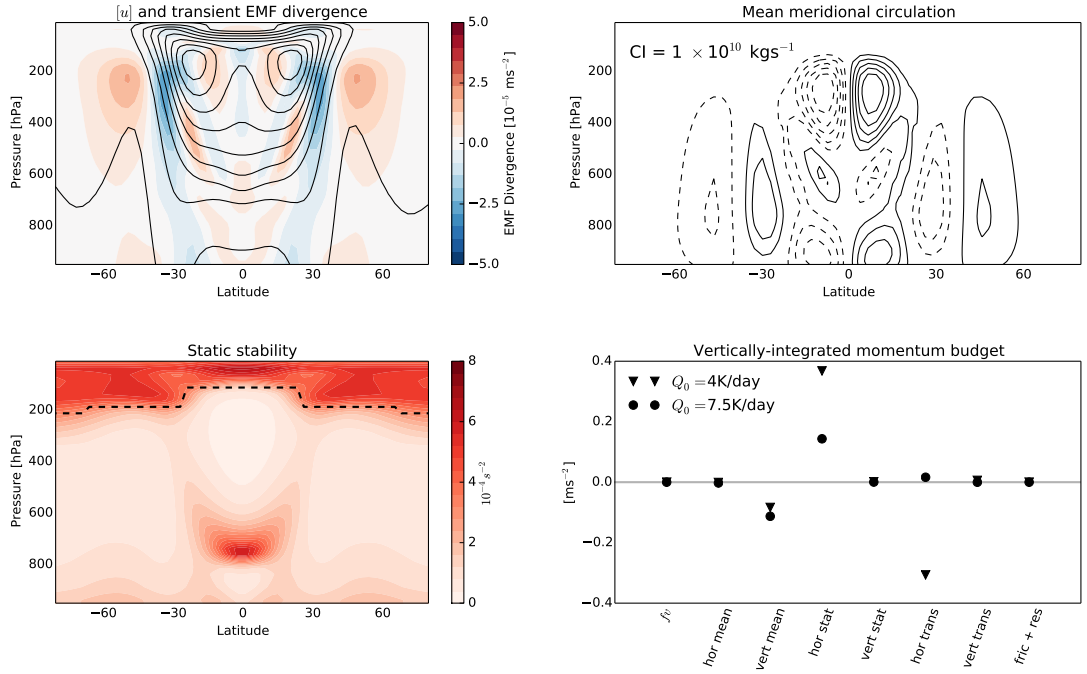


Figure 4.14: Top left panel: zonal-mean zonal wind (black contours) and eddy momentum flux divergence (colored contours) for the case with $Q_0 = 7.5\text{Kday}^{-1}$ and $\Delta_y = 40\text{K}$. The contour interval for the zonal wind is 10ms^{-1}. Top right panel panel: mean meridional circulation in the same experiment. Bottom left panel: static stability for the same experiment. Bottom right panel: terms in the vertically-integrated momentum budget at the equator for the $Q_0 = 4\text{K/day}$ and $Q_0 = 7.5\text{K/day}$ experiments.

When $\Delta_y = 40\text{K}$ the equatorial winds accelerate more slowly at first (black circles in Figure 4.13), but then there is a small jump from about 5ms^{-1} to about 7ms^{-1} between $Q_0 = 4\text{K/day}$ and $Q_0 = 5\text{K/day}$, and then a larger jump for $Q_0 = 7.5\text{K/day}$, as the winds accelerate to 32ms^{-1}. Figure 4.14 studies this experiment in more detail.

The top left panel shows there are very strong jets in the subtropics of each hemisphere (the maximum wind speeds are almost 100 ms^{-1}), with large shear on the poleward flanks of the jets co-located with regions of transient EMF convergence.

In the top right panel it can be seen that there are three circulation cells present in the tropics of each hemisphere: the conventional Hadley circulation rises to about 700hPa, then there is a counter-circulation extending from about 700hPa to 400hPa and then a third circulation cell above this. This three cell system develops because the rising air of the Hadley circulation is impeded by a layer of very high stability in the mid-troposphere (bottom left panel).

The bottom right panel compares the vertically-integrated terms in the equatorial momentum budget for this experiment with those from the 4K/day experiment. As would be expected from the previous section, in the 4K/day experiment the balance is mostly between the stationary EMF convergence, which accelerates the flow, and the mean vertical advection and the transient EMF convergence, which decelerate the flow. In the $Q_0 = 7.5$K/day experiment the mean vertical advection is similar, despite the re-organization of the tropical circulation; however the acceleration by the stationary eddies is about half the acceleration in the 4K/day experiment, while the transient EMF convergence is almost zero. The colored contours in the top left panel show that in the deep tropics the upper troposphere now acts as a source of transient EMF while the lower troposphere is still a sink of transient EMF, and these contributions essentially cancel when the vertical integral is taken. This is similar to how the transient eddies behave when Q_0 is small (Figure 4.12).

The eddy streamfunction responses near the equator in the two experiments are shown in the top panels of Figure 4.15 and the vertical profiles of the stationary horizontal EMF convergence at the equator are shown in the bottom panel of this figure. The streamfunction response in the 4K/day case is similar to the corresponding case with $\Delta_y = 60$K, and the stationary wave acts to accelerate the flow throughout the troposphere. In contrast, the response in the 7.5K/day experiment has an equivalent barotropic structure that is more similar to the vertical structure of mid-latitude stationary waves. The profile of the stationary EMF convergence also changes, as the

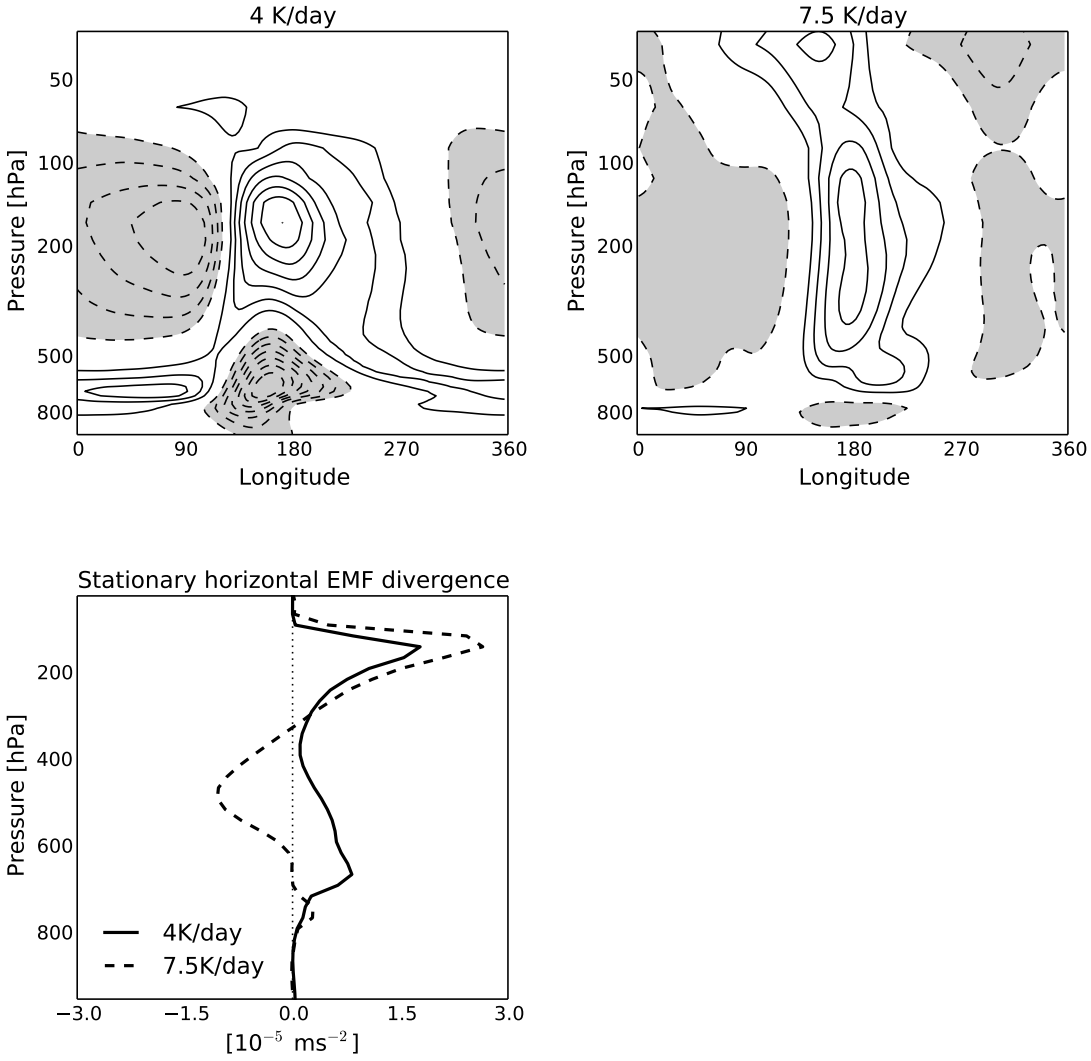


Figure 4.15: The eddy streamfunction responses at 2°N for $Q_0 = 4$K/day (top left panel) and $Q_0 = 7.5$K/day (top right panel) with $\Delta_y = 40$K. The bottom panel shows the vertical profiles of the stationary horizontal EMF convergence in these experiments.

wave continues to accelerate the flow in the upper troposphere but decelerates the flow in the mid-troposphere for $Q_0 = 7.5$K/day and so the net acceleration of the equatorial winds by the wave is reduced.

This strong superrotation is reminiscent of the axisymmetric shallow-water model results of Shell and Held (2004) [110] and also of the two-level results of Saravanan

(1993) [104], both of which found hysteresis in their experiments. In the shallow-water model the only damping on superrotation is the vertical advection of low momentum air by the Hadley circulation, and a hysteresis is present as the damping either weakens as the applied forcing is increased or strengthens as the forcing is increased, resulting in the existence of a strongly superrotating state and a weakly superrotating state for the same forcing [110]. In the two-level model the tropics become transparent to baroclinic eddies when strong equatorial heating is applied, eliminating the damping due to the transient EMF divergence. This persists when the heating is removed and so this model also experiences hysteresis [104].

While neither of these is exactly analogous to the situation here, the possibility of hysteresis in the GCM was investigated by performing a number of experiments initialized with the final state of the $Q_0 = 7.5$K/day experiment (red crosses in Figure 4.13), as well as some additional experiments starting from rest and using values of Q_0 between 5K/day and 7.5K/day. No evidence of hysteresis was found, however, because the transition from the equator being a sink of baroclinic eddies to the equator being both a source and a sink of baroclinic eddies is gradual, and there is no sudden jump from one state to the other. Moreover, although the tropical circulation transitions to having a three cell structure, the deceleration by the mean vertical advection stays roughly constant.

4.6 Constraining the Tropical Static Stability

The previous sections have shown that the GCM's response to tropical heating is closely tied to the behavior of the static stability in the deep tropics. This puts into question the relevance of the results for moist atmospheres, as the tropical stability responds quite differently to heating in the presence of moisture. As a step towards addressing this question, several experiments were repeated with the Held-Suarez

forcing replaced by the forcing of Schneider (2004) (S04, [106]), which strongly relaxes temperatures in the deep tropics to a moist pseudoadiabat. In this set-up an extra term is added to the temperature equation:

$$\frac{\partial T}{\partial t} = ... - w(\phi)\frac{T - T_m(p)}{\tau_c}, \tag{4.7}$$

where τ_c is the convective time-scale, set to 4 days, and T_m is the moist pseudoadiabatic temperature, calculated using the instantaneous surface temperature, T_s, as

$$T_m = T_s + \int_{p_s}^{p} \Gamma_m(p')dp', \tag{4.8}$$

where Γ_m is the moist pseudoadiabatic lapse rate. The weight function $w(\phi)$ is given by

$$w(\phi) = 1 - tanh\left(\frac{sin^2\phi}{sin^2\phi_t}\right),$$

with ϕ_t chosen to be 6°. The [106] forcing also uses a different T_{eq} field:

$$T_{eq}(p,\phi) = 200K\left(1 + \left(\left(\frac{T_{s,eq}(\phi)}{200K}\right)^4 - 1\right)(p/p_0)^{3.5}\right)^{1/4}, \tag{4.9}$$

where

$$T_{s,eq}(\phi) = 300K + \Delta_y(1/3 - sin^2\phi), \tag{4.10}$$

with $\Delta_y = 60$K. Finally, the parameterization of the boundary layer is changed from linear to quadratic damping, with a co-efficient of 0.7×10^{-5} m^{-1}. These are the same parameter settings as in the reference simulation of S04.

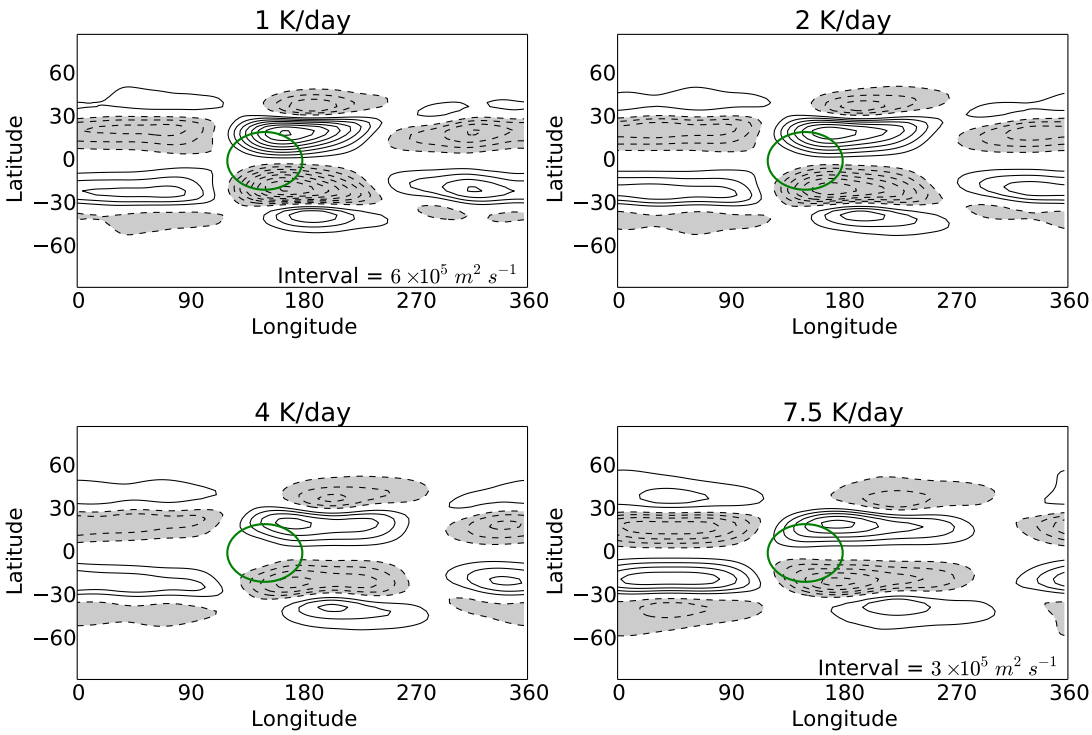


Figure 4.16: As in Figure 4.1 but for the experiments with the S04 forcing and the results have been normalized by $1/Q_0$. Note the different contour level used in the bottom right panel.

This set-up produces more Earth-like tropical temperatures and a stronger Hadley circulation than the Held-Suarez set-up, but its zonal wind distribution is less realistic. For instance, the vertical-mean winds at the equator are nearly superrotating in the unperturbed state (diamonds in Figure 4.13), and the winds in the upper troposphere superrotate even without any applied heating.

Despite this reference state, the stronger Hadley circulation results in the equatorial winds accelerating more slowly when tropical heating is applied (Figure 4.13), and the response stays in an approximately linear regime for heating rates up to 2K/day (top panels of Figure 4.16). This response is dominated by a Rossby wave in each hemisphere, and the Kelvin wave of the Matsuno-Gill response is much less prominent. This is because even in the unperturbed state the upper troposphere su-

perrotates and so the zonal advection term plays a larger role in the vorticity budget than in the experiments with the Held-Suarez set-up (bottom panel of Figure 4.8; note that the vorticity balance of a stationary Rossby wave is between the meridional and zonal advection terms).

The equatorial winds accelerate more rapidly between $Q_0 = 2$K/day and $Q_0 = 4$K/day, and in the $Q_0 = 7.5$K/day the vertically-integrated winds are roughly the same as in the corresponding experiment with the original Held-Suarez set-up, as is the pattern of the eddy streamfunction response (bottom panels of Figure 4.16). So although the model exhibits a different linear response when forced with the S04 set-up than when it is forced with the Held-Suarez set-up, it undergoes a similar transition and produces a similar response for large Q_0.

4.7 Conclusion

This study has investigated the response of a dry atmosphere to an equatorial heat source that mimics the convective heating due to the positive phase of the ENSO. Using the standard Held-Suarez set-up it is found that weak (<0.5K/day) heating rates produce responses that are in an approximately linear regime and that resemble the response of the classic Matsuno-Gill model to equatorial heating. This resemblance can be seen both by visual inspection of the responses and by analyzing the vorticity budgets of the simulations. The breakdown of the linear regime takes place because the heating stabilizes the tropical atmosphere, which causes the stretching term in the vorticity budget to increase sub-linearly as Q_0 is increased. In the non-linear regime the response is dominated by a Rossby wave that propagates away from the equator along a great circle and resembles the response of a superrotating barotropic model to a tropical heat source [105].

At the same time, the model increasingly superrotates as the maximum heating rate is increased. This could also be a reason for the breakdown of the linear regime, as the Matsuno-Gill model assumes that the tropics are quiescent, but the response becomes non-linear because of the increased stability before the superrotation becomes significant. The superrotation is driven by the equatorward flux of momentum by the stationary waves excited by the heating, and is damped by the vertical advection of low momentum air by the mean circulation and by the transient eddies, which increasingly break in the deep tropics, transferring momentum to higher latitudes. This contrasts with previous studies, such as [63], in which the mean vertical advection term is the only negative feedback on superrotation. The results here are also quite different from the idealized studies of [110] and [104]. The former assumed that the mean vertical advection was the only negative feedback on superrotation, while in the two-level model of [104] the equator becomes transparent to transient eddies, which propagate from one hemisphere to the other. Here it has been shown that in a strongly superrotating, multi-level GCM transient eddies are the main negative feedback on the acceleration of the equatorial winds when strong heating is applied to the GCM.

These dynamics have been explored by varying the equator-to-pole temperature gradient of the equilibrium temperature field and by replacing the Held-Suarez forcing with the Schneider (2004) forcing, which strongly constrains the tropics to follow a moist pseudoadiabat. The same qualitative behavior is seen in the experiments with varied equator-to-pole temperature gradients; however the model can be made to strongly superrotate by applying a large heating to a set-up with a smaller equator-to-pole temperature gradient. This large acceleration occurs because the equatorial winds transition from being a sink for transient baroclinic eddies to becoming both a source and a sink, so that the vertically-averaged transient EMFs no longer decelerate the flow. As the winds accelerate the stationary EMF convergence is also reduced,

as the vertical structure of the stationary response changes, and so eventually the deceleration by the vertical advection of low momentum air is enough to balance the acceleration. No evidence of hysteresis was seen in the GCM. Note, also, that the strong superrotation requires a maximum heating rate greater than 5K/day, which is roughly three times the largest heating rates observed in the present climate of the Earth.

Finally, when the model is forced with the Schneider (2004) set-up the linear response is dominated by a stationary Rossby wave because the upper tropospheric winds superrotate even without any applied heating. The stronger Hadley circulation in this set-up also means that the equatorial winds accelerate more slowly. However, when large enough heatings are applied to the model the non-linear regime is similar to that in the original Held-Suarez set-up.

At present Earth's atmosphere seems to respond approximately linearly to the tropical heating it experiences; however, this linear regime could break down if the tropical heating on Earth were to strengthen or if the equator-to-pole temperature gradient were to be reduced significantly. Superrotation would also be more likely in these scenarios. The results of this study are also relevant for planetary atmospheres; for example, the atmosphere of a tidally-locked planet that orbits close to its star would experience very strong equatorial heating. As was mentioned in section 4.6 however, a major caveat is that this study has focused on the behavior of a dry atmosphere. Some of the same dynamics might be expected to hold in moist models; for instance, moist models also produce Matsuno-Gill-type responses to tropical heating (e.g., [14]; [68]), but the key differences would be in the response of the tropical stability and in the shape of the heating, which would deepen as the maximum heating rate is increased. It is left for future work to determine how the results of this study would be affected by the presence of atmospheric water vapor.

Chapter 5

Lower Tropospheric Eddy Momentum Fluxes in Idealized Models and Reanalysis Data

5.1 Introduction

One of the distinctive features of Earth's troposphere is the convergence of angular momentum in midlatitudes by large-scale eddies. This transfer mainly takes place in the upper troposphere, where the convergence of eddy momentum flux (EMF) helps sustain an eddy-driven jet in each hemisphere. From a wave-mean flow perspective, the explanation for this pattern in the EMF is that baroclinic zones in midlatitudes act as source regions for eddies, which propagate meridionally until they break before or near their critical latitudes [95]. The irreversible process of breaking transfers momentum from the sink regions, where the waves break, to the source regions, where the eddies originate (e.g., [39]; [129]).

As EMFs are much larger in the upper troposphere than in the lower troposphere, there has been little study of lower tropospheric EMFs. However, O'Rourke and

Vallis (2016) recently showed that in an idealized dry GCM long wavelength eddies with slow eastward propagation *diverge* momentum away from the eddy-driven jet in the lower troposphere in Earth-like settings [86]. While these fluxes are weak and do not contribute substantially to the vertically integrated flux that controls the near surface winds, Chai et al. (2016) found that the EMFs in the lower troposphere of a similar idealized, dry GCM grow in magnitude when the frictional damping time-scale near the surface is increased, reaching values comparable to the upper level EMFs when this time scale is increased by several orders of magnitude (a parameter setting which may be relevant for studying Jupiter's atmosphere) [16]. The long, slow waves responsible for these lower tropospheric EMFs may also play a more prominent role in double-jet states ([62]; [85]) and in superrotating atmospheres [104].

Here the EMFs in the lower troposphere of two different idealized models and in a reanalysis dataset are studied. I start by comparing the EMFs in the upper and lower troposphere of the reanalysis data. Next, I ask whether the idealized models can reproduce the features seen in the reanalysis data, and then use the models to interpret this behavior of the eddies. The models considered are a two-layer quasi-geostrophic (QG) model on a β-plane and the same GCM as was used in the previous chapters. The two-layer QG model formed the basis for the first numerical study of the general circulation [91] and has continued to play an important role in the theoretical development of atmospheric dynamics, being used for instance in studies of baroclinic wave-packets [66], in the development of eddy closure schemes ([89]; [44]; [137]) and in idealized studies of annular modes ([139]; [138]). The value of the two-layer QG model in these studies is due to the fact that despite its simplicity, it is able to capture many key features of the observed dynamics of the midlatitude troposphere. In this study I use it as the base of a model hierarchy for studying lower tropospheric EMFs. The GCM is used to test how the two-layer dynamics carry over

into the more complex setting of a primitive equation model on a sphere, providing a connection from the two-layer model to the reanalysis data.

5.2 Data, Models and Methods

5.2.1 Reanalysis data

The observational data are taken from the Modern-Era Retrospective Analysis for Research and Applications (MERRA) dataset [96]. To make as clean a comparison as possible with the idealized models only data from the southern hemisphere have been used and I focus on austral summer (DJFM); the reason for this restriction is discussed in section 5.3.

5.2.2 Two-layer QG model

The two-layer QG model consists of two different density layers on a β-plane, in which the meridional temperature gradient is relaxed towards an equilibrium profile. The layers have equal depths and bottom friction is present in the lower layer. In non-dimensional form the equations are

$$\frac{\partial q_k}{\partial t} + J(\psi_k, q_k) = -\frac{1}{\tau_d}(-1)^k(\psi_1 - \psi_2 - \psi_R) - \frac{1}{\tau_f}\delta_{k2}\nabla^2\psi_k - \nu\nabla^4 q_k, \tag{5.1}$$

where $q_k = \nabla^2\psi_k + (-1)^k(\psi_1 - \psi_2) + \beta y$ is the potential vorticity (PV) in the upper ($k = 1$) and lower ($k = 2$) layers; the ψ_ks are the corresponding streamfunctions; τ_d is a Newtonian relaxation time scale; τ_f is a Rayleigh friction time scale acting only in the lower layer (this is indicated by the Kronecker δ function); and ν is a hyper-diffusion coefficient.

The model domain is a zonally periodic channel with a baroclinic zone in the center of the domain created by setting the radiative equilibrium temperature $(\psi_1 - \psi_2)$

gradient to a hyperbolic secant centered at $y = 0$. In radiative equilibrium (i.e. in the absence of eddy fluxes) the lower layer flow ψ_2 is identically zero so that the zonal flow in the upper layer $U_1(y) = -\partial\psi_1/\partial y = -\partial\psi_R/\partial y$ is:

$$-\frac{\partial\psi_R}{\partial y} = sech^2(y/\sigma), \tag{5.2}$$

where σ sets the half-width of the jet.

The code is spectral and doubly periodic so sponges are present near the northern and southern boundaries in order to produce a channel geometry. The sponges take the form of strong exponential damping with the same half-width as the jet. I have verified that the domain is wide enough that the sponges do not affect the dynamics.

The control non-dimensional parameter settings are: $\beta = 0.2$, $\sigma = 3.5$, $\tau_f = 15$, $\tau_d = 100$ and $\nu = 0.01$. The zonal width $L_x = 46$ and the meridional width $L_y = 68$; 42 and 85 zonal and meridional Fourier modes are retained, respectively, using a standard spectral transform algorithm that computes the projection of non-linear products onto the retained modes exactly. The maximum strength of the vertical shear of the zonal wind in radiative equilibrium is used as the velocity scale (U) in non-dimensionalizing these equations, while the length scale (L) is the deformation radius. The time scale is then L/U, which I refer to as a "model day", although it is only about a fifth of a day for plausible choices of L and U. It is preferable to describe results from the two-layer model non-dimensionally because there is no unambiguously optimal choice of parameters that provides the best comparison with observations.

Each simulation was run for 10 000 model days, with data recorded once every four model days. I have conducted a variety of parameter variations to test for robustness, but the most interesting, discussed in section 5.5, is the sensitivity of the EMFs to the strength of the frictional damping,

With the control parameter settings the two-layer model produces an Earth-like climate [139]. For instance, in observations the ratio of eddy kinetic energy to zonal-mean kinetic energy is approximately unity on Earth, and this is often a good measure of realistic Earth-like nonlinearity in an idealized model. This ratio is a reasonable value of 1.3 in the two-layer model when the control parameters are used. However, a potentially important difference with the Earth's atmosphere is that the jet is not "self-maintaining" in this set-up. Following Robinson (2006) [100], a jet is self-maintaining if there is a maximum in the upper level PV flux (i.e., since the flux is negative, a minimum in the amplitude of the flux) in the core of the jet. This means that eddies break near their critical latitudes and so the baroclinicity is reduced more on the flanks of the jet than in the center, and is what is observed in Earth's jets. Eddies in the two-layer model typically break well before reaching their critical latitudes [65] and so in this sense the EMFs in the model are quite different from those in Earth's atmosphere. Weak baroclinic instability (high β) and strong friction are required to produce a self-maintaining jet in the two-layer model ([89]; [65]), so it is difficult to produce a climate that is both Earth-like and has a self-maintaining jet.

5.2.3 Primitive equation model

As in the previous three chapters, the idealized atmospheric GCM is the GFDL spectral dynamical core, which solves the primitive equations for a dry ideal gas and is forced by zonally-symmetric Newtonian relaxation to a prescribed equilibrium temperature field and damped by Rayleigh friction near the surface. The standard Held-Suarez parameter settings were used. The model was run at T85 resolution with 30 vertical levels for 10 000 days, with the first 500 days discarded as spin-up and data recorded once per day. The stratosphere is poorly represented in this model.

5.2.4 Methods

For both the GCM and the reanalysis data 300hPa is taken as a representative upper tropospheric level and 800hPa is taken as a representative lower tropospheric level. The choice of lower-tropospheric level is more significant in the reanalysis data than in the idealized GCM because topography intrudes into this level in the reanalysis data. I have discarded all data for which this is the case and linearly interpolate across these gridpoints. 800hPa is the lowest level at which this does not qualitatively affect the results in the vicinity of the jet. However, intruding topography is particularly an issue at high latitudes and so I have cut-off the analysis of the lower tropospheric spectra at 65°S. At lower latitudes the majority of the data are retained but there are still some discontinuities, mainly due to the Andes. Since the Andes mostly sit between about 30°S and 10°S they do not affect the spectra near the jet significantly.

My main analysis tool is eddy flux co-spectra, as used by [38], [95] and many others. To calculate these I compute the space-time co-spectra of (u, v) at each latitude and then transform the spectra to (phase speed, wavenumber) space, for the two-layer model; or (angular phase speed $\times$ a, wavenumber) space for the GCM and reanalysis data, where a is the Earth's radius. On the sphere it is the angular phase speed rather than the phase speed which is conserved by Rossby wave packets. Finally I sum over all wavenumbers to obtain the spectra as functions of (angular) phase speed and latitude. The seasonal spectra are calculated by estimating the spectra for each year individually and then averaging over all years (35 in total).

5.3 EMFs in Reanalysis Data

The average DJFM EMF divergence in the southern hemisphere of the reanalysis dataset is shown in the left panel of Figure 5.1 for reference. There is a region of strong EMF convergence close to the maximum jet-speed, centered at about 250hPa

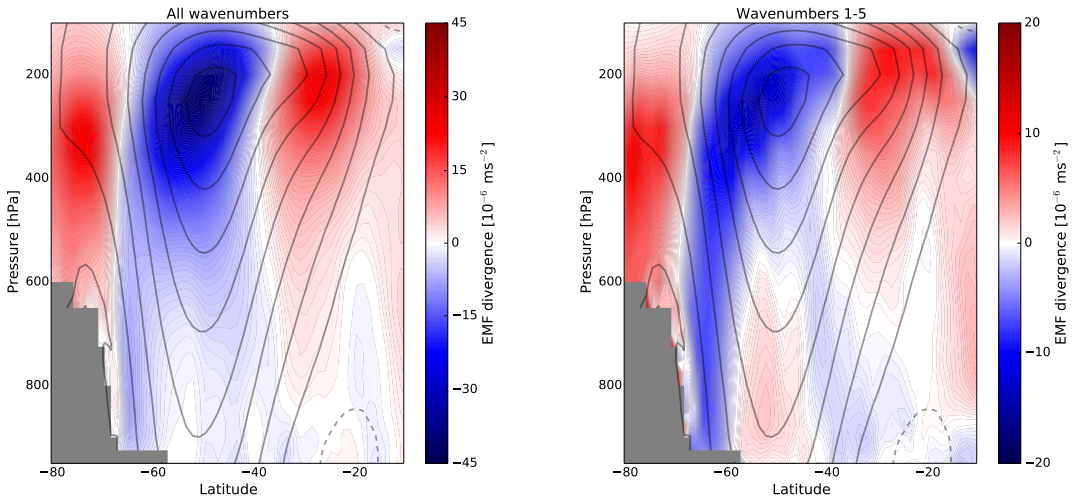


Figure 5.1: The left panel shows the average DJFM EMF divergence in the southern hemisphere of the MERRA data in color and the zonal-mean zonal winds in gray, with contour spacing 4 ms^{-1} and negative values dashed. Locations at which topography intrudes into more than one third of the gridpoints are shaded. The right panel shows the average DJFM EMF divergence due to eddies with wavenumbers one to five. Note the different colorbar scales.

and 50°S, and on either side of this convergence are regions of weaker EMF divergence, with more divergence on the equatorward side of the jet than on the poleward side. The maximum EMF divergence on the poleward side of the jet is at a lower altitude (∼350hPa) than the equatorward maximum. As discussed earlier, the EMFs are much larger in the upper than in the lower troposphere.

The right panel of Figure 5.1 shows the contribution of eddies with wavenumbers one to five to the average EMF divergence in this season. The pattern is generally quite similar to that of the total EMF divergence, however in the lower troposphere there is a region of EMF divergence in the jet core, centered at about 850hPa. There are regions of EMF convergence on either side of this, with the convergence on the poleward side being particularly strong. As in the idealized model of O'Rourke and Vallis then, long waves transfer momentum out of the jet in the lower troposphere.

The top panels of Figures 5.2 and 5.3 show the divergence of the DJFM EMF co-spectra at the 300hPa and 800hPa levels, respectively. The upper tropospheric

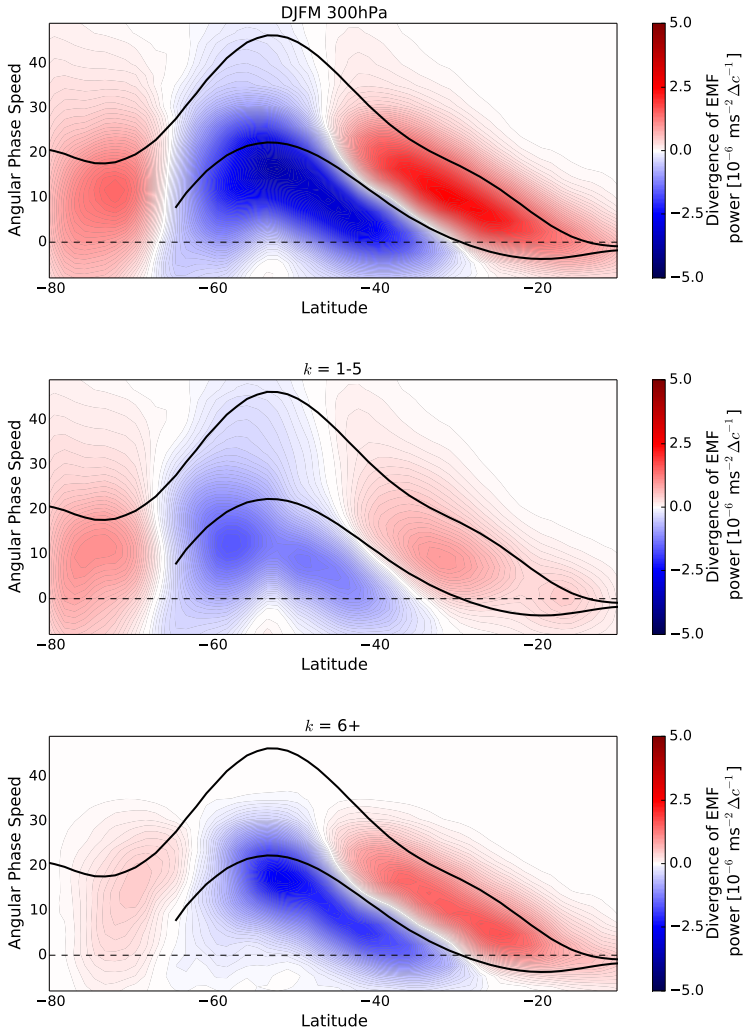


Figure 5.2: Top panel: DJFM average of the divergence of the EMF co-spectra at the 300hPa level in the MERRA data. Middle panel: same but with the co-spectra only calculated using wavenumbers one to five. Bottom panel: same but with the co-spectra only calculated using wavenumbers six and higher. The solid black lines show the zonal-mean winds at 300hPa and 800hPa. Δc is 2.3 ms^{-1}.

fluxes are familiar, with EMF convergence in midlatitudes and EMF divergence in the subtropics near the eddies' critical latitudes. There is also some divergence near the poleward critical latitudes. The eddies mostly propagate eastwards with angular phase speeds of 5 - 20ms^{-1} and the maximum convergence takes place in the jet core at an angular phase speed of approximately 15ms^{-1}.

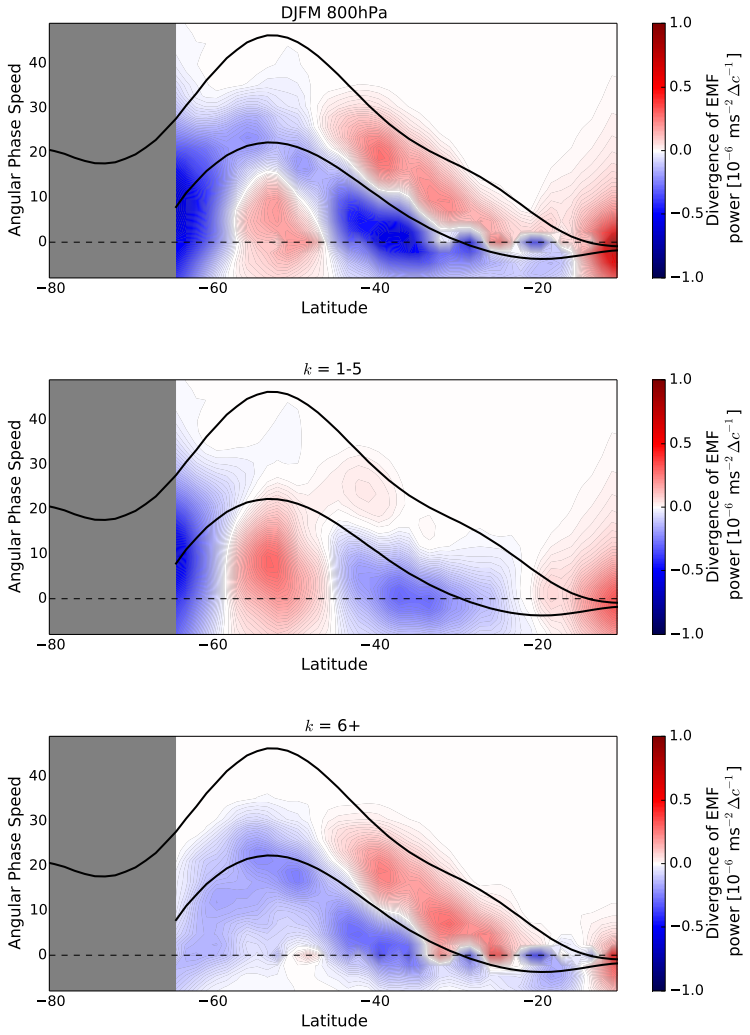


Figure 5.3: Same as Figure 5.2 but for the 800hPa level in the MERRA data. Δc is 2.3 ms^{-1}.

In the lower troposphere there is EMF divergence at slow ($\leq$10ms^{-1}) phase speeds in the center of the jet. This divergence at slow phase speeds is seen in all seasons but is most prominent in DJFM, which is why I focus on austral summer here. Equatorward of this divergence is a region of EMF convergence near the flank of the jet in the lower troposphere, where lower tropospheric eddies would be expected to break. There appears to be strong EMF convergence on the poleward side of the jet in the lower troposphere; this is expected from Figure 5.1 but could equally

be due to contamination by intruding topography. There is also a region of weak EMF convergence in the jet center at phase speeds close to the maximum lower tropospheric jet speed ($\sim$20ms^{-1}), and a region of EMF divergence in the subtropics at phase speeds close to the subtropical jet speed in the upper troposphere.

The middle and bottom panels of Figures 5.2 and 5.3 show the spectra calculated using only zonal wavenumbers one to five and using only wavenumbers six and greater, respectively. In the upper troposphere (Figure 5.2) the spectra are quite similar in these two spectral ranges, though wavenumbers six and higher contribute more to the EMF convergence in the center of the jet. The EMF by the high zonal wavenumbers is strongly biased towards the equator, whereas that due to the smaller wavenumbers is fairly symmetric about the center of the jet.

The decomposition shows that in the lower troposphere the low wavenumber eddies are responsible for the EMF divergence in the jet center, as well as the EMF convergence on the flanks of the jet (Figure 5.3). The pattern of the high wavenumber eddies is similar to what is seen in the upper troposphere, as there is EMF convergence at fast phase speeds in the jet center and EMF divergence in the subtropics; the EMF convergence cancels out the divergence by the low wavenumber eddies somewhat.

This distinction between the high wavenumber eddies, which are similar in the upper and lower troposphere, and the low wavenumber eddies, which behave differently in the upper and lower troposphere, is what I will focus on with the idealized models.

5.4 EMF spectra of the Idealized Models

Figure 5.4 shows the divergence of the EMF co-spectra in the lower tropospheres of the idealized models. As before, the top panels show the spectra calculated using all the wavenumbers, the middle panels show the spectra calculated using wavenumbers

one to five and the bottom panels show the contributions from higher wavenumbers. Panels on the left show results from the QG model and panels on the right show results from the GCM. The upper tropospheric spectra of both models have been studied by many others in the past and so I do not show them here.

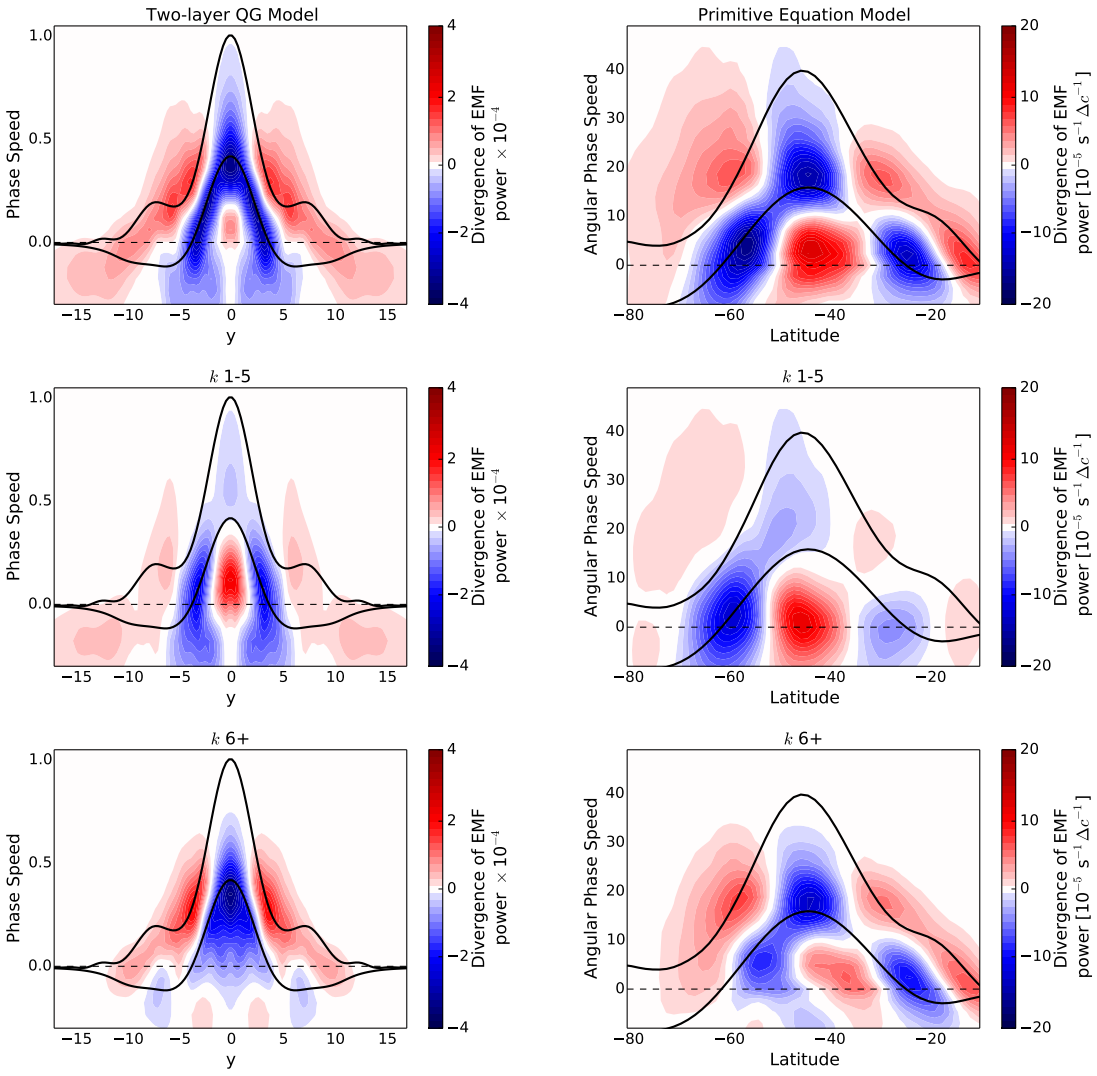


Figure 5.4: Same as Figure 5.2 but for the lower layer of the two-layer QG model (left panels) and the 800hPa level in the primitive equation model (right panels). Δc is 0.06 for the QG model and 2.3 ms^{-1} for the primitive equation model.

In the lower layer of the QG model there is a dipole in the center of the domain, with a maximum in the EMF convergence at phase speeds close to the maximum lower layer wind speed and a weaker maximum in the divergence at phase speeds slightly greater than zero (top left panel of Figure 5.4). The former is flanked by regions of divergence and the latter is bordered by regions of convergence, after which there is divergence still further from the jet. The EMF divergence in the jet center at slow phase speeds is due to low wavenumber eddies and is partially cancelled out by the EMF convergence due to shorter waves. The pattern of the short waves resembles the pattern in the upper layer (not shown), though the EMF convergence maximum is at a faster phase speed in the lower layer. This could be because there are some more slowly propagating waves which cause divergence in the lower layer, as the long waves do, and cancel out some of the convergence at lower phase speeds.

The lower troposphere of the GCM is similar (right panels of Figure 5.4), with a region of EMF convergence at fast phase speeds in the center of the jet bordered by regions of divergence, and a region of EMF divergence in the center of the jet at slow phase speeds bordered by regions of convergence. The EMF divergence in the center of the jet is relatively stronger than in the QG model, though it is still weaker than the convergence. There is little evidence of the eddies being stronger on the equatorward side of the jet. Once again, the low wavenumber eddies cause the EMF divergence in the center of the jet, and this is partially cancelled out by EMF convergence due to the fast eddies. However, there is some EMF divergence at slow phase speeds for wavenumbers six and higher and so the separation between the fast waves, which converge momentum into the jet, and the slow waves, which diverge momentum out of the jet, takes place at a different wavenumber in the GCM.

The lack of equatorward bias in the lower troposphere of the GCM can partly be explained by the fact that the lower layer winds are fairly symmetric about the jet center. The eddy heat flux (EHF), which can be taken as a proxy for the baro-

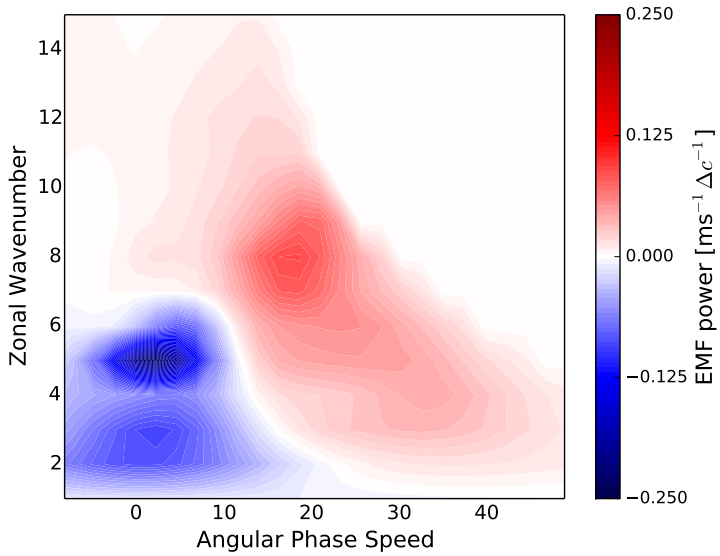


Figure 5.5: Zonal wavenumber-phase speed co-spectra for the eddy momentum flux in the GCM at 48°S. Δc is 2.3 ms^{-1}.

clinic stirring that excites meridionally-propagating eddies, is also symmetric about the jet (not shown), so eddies in the lower troposphere are equally likely to propagate polewards or equatorwards. In contrast, in the upper troposphere there is a large separation between the baroclinic source region and the breaking region on the equatorward side of the jet, while the poleward breaking zone is close to the baroclinic source. This means that in the upper troposphere there is less space for the eddies to propagate polewards and transport momentum from high latitudes into the jet. [60] noted this asymmetry in an idealized GCM similar to the one used here, in CMIP3 models and in observations; and suggested that it is relevant for the expected poleward shift of the midlatitude jets in global warming scenarios.

More insight into the behavior of the eddies can be obtained by examining zonal wavenumber-phase speed co-spectra at individual latitudes. Figure 5.5 shows this for the GCM at 48°S, which is slightly polewards of the maximum jet speed. There is a clear separation between wavenumbers ≤ 6, which transport momentum away from the jet at slow phase speeds, and the higher wavenumbers, which transport

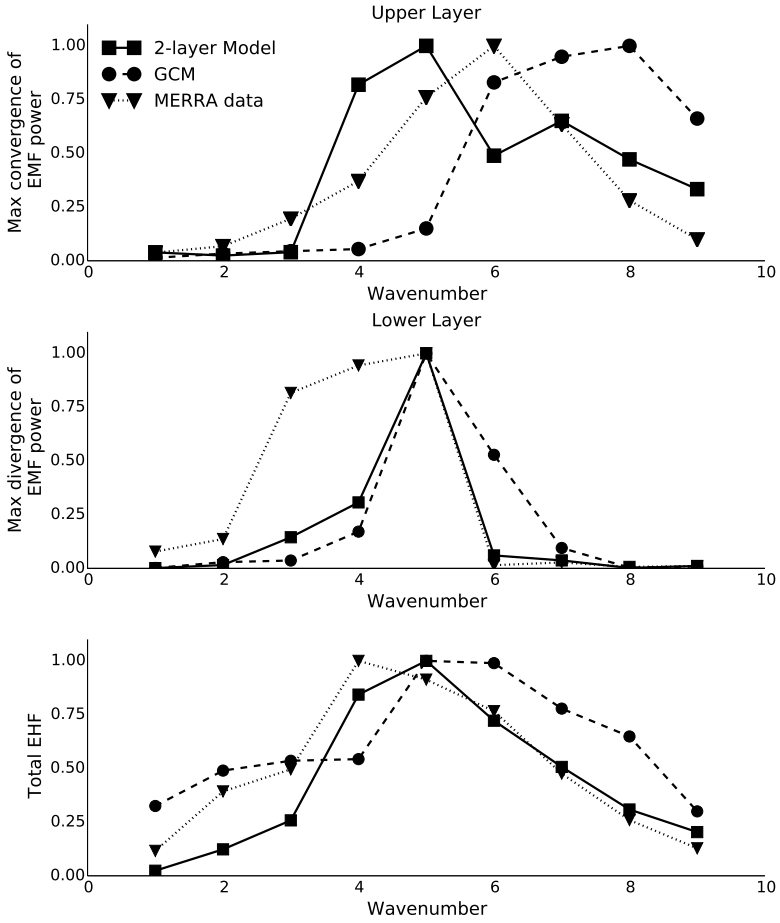


Figure 5.6: Top panel: Maximum EMF convergence in the jet core as a function of wavenumber for the upper layer of the two-layer QG model (squares), the 300hPa level in the primitive equation model (circles) and the 300hPa level in the MERRA data (triangles). The values have been normalized so that the largest absolute value of the EMF convergence is one and spectra have only been calculated for the first nine wavenumbers. Middle panel: same but for the EMF divergence in the lower layer of the two-layer QG model and the 800hPa level in the primitive equation model and the MERRA data. Bottom panel: the integrated EHF as a function of wavenumber in the lower layer of the QG model and the 800hPa level in the primitive equation model and the MERRA data.

momentum into the jet at faster phase speeds. Note, however, that low wavenumber eddies do transport momentum into the jet at fast phase speeds, but this flux is weaker than the flux at slow phase speeds.

To understand more systematically which wavenumbers dominate the EMFs, the maximum EMF convergence at the latitude of maximum wind speed in the upper troposphere and the maximum EMF divergence at the latitude of maximum wind speed in the lower troposphere are plotted as a function of wavenumber for both models and for the reanalysis data in the top two panels of Figure 5.6. That is, the EMF co-spectra were calculated for the first nine wavenumbers individually and the maximum and minimum EMF divergence at the center of the jet were then calculated for each wavenumber. The curves are normalized by their largest absolute value to facilitate comparison between the two models and the reanalysis data.

In the upper layer of the QG model there is significant EMF convergence for wavenumbers four and five, after which the EMF convergence essentially decreases with increasing wavenumber. The GCM results are similar, except that the largest convergence is at wavenumbers six and seven. Note that the dominant wavenumber in the QG model can be changed if desired by adjusting the length of the channel. In the reanalysis data the EMF convergence peaks at wavenumber six and then decreases with increasing wavenumber.

The curves for the lower layers of the two models are nearly identical to each other, with the largest EMF divergence in the center of the domain at wavenumber five, as was seen by [85], though wavenumbers three and four are also responsible for some EMF divergence. In the primitive equation model there is some additional divergence due to wavenumber six eddies, as expected from Figure 5.4. Wavenumber five eddies are also responsible for the largest EMF divergence in the reanalysis data, but wavenumbers three and four contribute nearly as much to the total divergence.

The differences in the EMF divergence between the two models and the reanalysis data may reflect differences in the stirring. This can be seen from the bottom panel of Figure 5.6, which is similar to the upper two panels but instead of taking the maximum of each EMF co-spectrum, the integral of each EHF co-spectrum is computed. In

agreement with the EMF results, the EHF by wavenumber six is much stronger in the GCM than in the QG model or in the MERRA data, while in the reanalysis data the EHF by wavenumber four eddies is stronger. Hence the lower layer EMFs are closely tied to the stirring, whereas the upper layer eddies are less directly influenced by the wavenumber structure of the stirring.

These comparisons show that the idealized models can reproduce many of the features of the reanalysis co-spectra, though there are some differences in the relative magnitudes of the EMF divergence and convergence, as well as in the wavenumbers of the dominant eddies. Nevertheless, it seems reasonable to interpret the reanalysis data by considering the behavior of the eddies in the idealized models.

5.5 Effects of varying the frictional time-scale

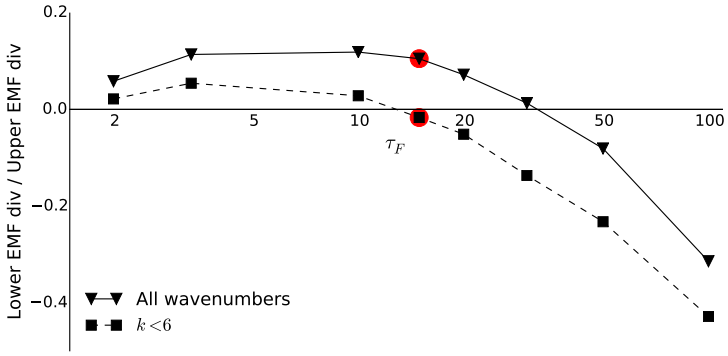


Figure 5.7: The lower layer EMF divergence divided by the upper layer EMF divergence in the QG model as the frictional time-scale is varied (solid line and triangles). The dashed line and squares show the same quantity but only the lower layer EMF divergence due to eddies with wavenumbers one to five is used. The red dots indicate the ratios for the control simulation.

In a QG system the vertically integrated EMFs must go to zero in the limit of vanishing surface friction, i.e the upper and lower tropospheric EMFs must cancel, if they are non-zero. This implies that the lower tropospheric EMFs must increasingly

diverge momentum away from the jet and must also become stronger relative to the upper tropospheric EMFs as friction is decreased. As mentioned in the introduction to this chapter, Chai et al. found that the EMFs in the lower troposphere of an idealized GCM become much stronger and diverge momentum out of the jet when the frictional time-scale is increased by several orders of magnitude relative to the standard Held-Suarez value. However, in the GCM the approach to this limit is non-monotonic, as varying friction also causes the jets to shift in latitude, which affects the propagation of eddies. For instance, there is less EMF divergence in the lower troposphere of the GCM if the frictional time-scale is either doubled or halved than with the original parameter setting (not shown).

The effects of varying friction can be studied more cleanly in the two-layer model as the position of the jet is fixed. Figure 5.7 plots the ratio of the lower layer EMF divergence to the upper layer EMF divergence as the frictional time-scale τ_F is varied from 2.5 model days to 100 model days (which is roughly equivalent to 20 Earth days; i.e., approximately one diabatic time-scale). When the time-scale is decreased from the control value (τ_F = 15 model days) the ratio slowly decreases, while the ratio decreases and then changes sign when τ_F is increased. As expected, this is because the low wavenumber eddies increasingly diverge momentum out of the jet (dashed curve in Figure 5.7). The higher wavenumber eddies are relatively insensitive to the strength of the friction.

The divergence of the EMF co-spectra in both layers for the experiment with τ_F = 100 model days is shown in Figure 5.8. The region of EMF divergence in the lower layer is now much broader and stronger, and there is little EMF convergence in the lower layer. The pattern of the upper layer co-spectra is fairly similar to what is seen in the control run. Surprisingly, the phase speeds are relatively unchanged, despite the large acceleration of the lower layer winds.

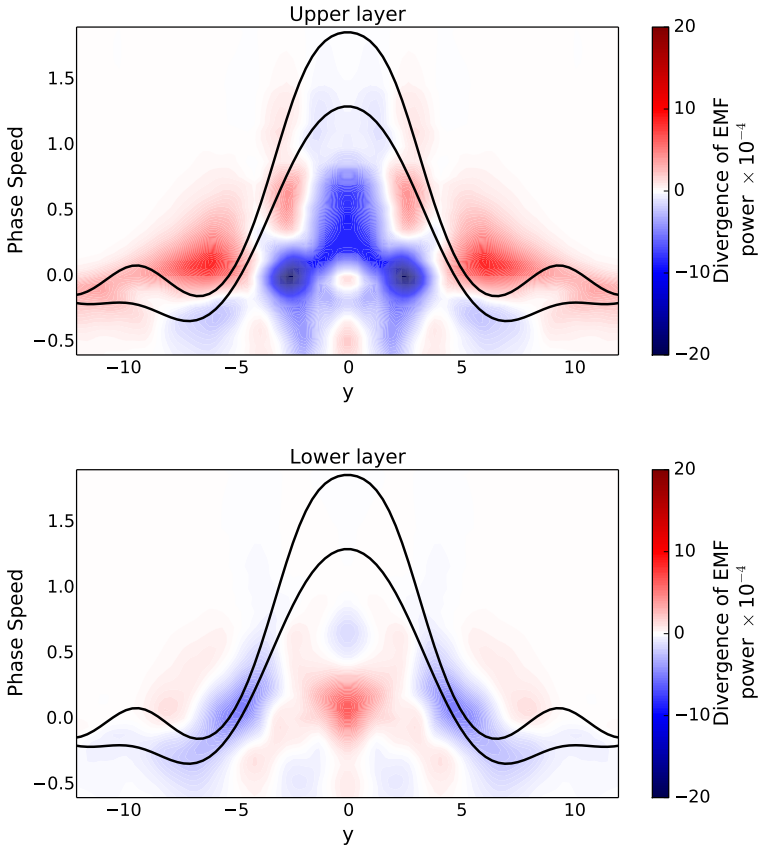


Figure 5.8: Divergence of the EMF co-spectra in the upper (top panel) and lower (bottom panel) layer of the two-layer QG model for the experiment with $\tau_F = 100$ days. Δc is 0.06.

5.6 Interpretation of the Lower Tropospheric Spectra

The previous sections have shown that there is a marked difference between the behavior of the high ($\geq$ six) wavenumber eddies and the low wavenumber eddies in both models, as well as in the reanalysis data. The high wavenumber eddies are essentially equivalent barotropic, and cause EMF convergence at fast phase speeds in the center of the jets and EMF divergence on the flanks. They also show more of an equatorward bias when spherical geometry is included. Conversely, the low

wavenumber eddies behave differently in the upper and lower layers: in the upper layer they converge EMF in the jet center while in the lower layer they produce both EMF divergence and EMF convergence. So understanding the lower tropospheric co-spectra requires understanding the fast, equivalent barotropic eddies as well as the slow eddies which are more prominent in the lower troposphere.

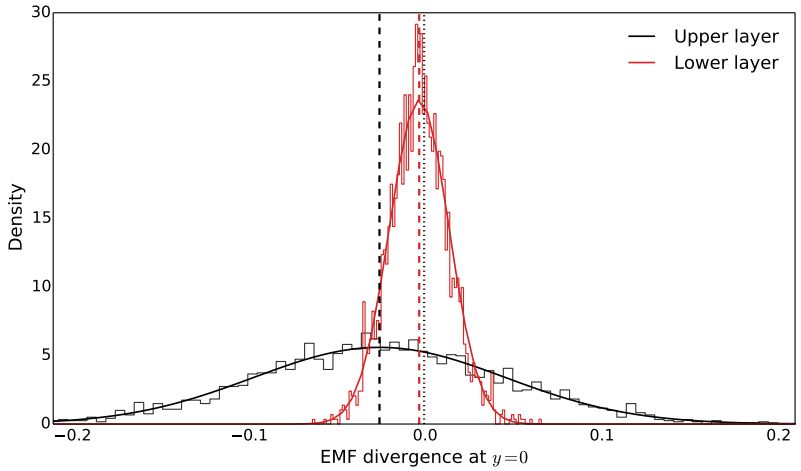


Figure 5.9: Probability density functions (PDFs) of the daily EMF divergence in the center of the upper (thin black lines) and lower (thin red lines) layers of the two-layer QG model. The thicker lines show Gaussian fits to the PDFs and the dashed vertical lines show the means of the distributions.

The similarities of the co-spectra suggest that the two-layer model can be used to interpret the dynamics of the lower troposphere, even though the jet in the control set-up is not self-maintaining. However, the co-spectra in this simulation are the result of a large amount of cancellation. This can be seen from Figure 5.9, which plots the probability density functions of the daily upper (black) and lower (red) EMF divergence in the center of the two-layer model, and shows that the time-mean divergence in each layer is a very small fraction of the total variability range. Together with the strong coupling between the two layers, this makes it difficult to cleanly isolate the dynamics generating the lower tropospheric EMFs. Nevertheless, I offer the following tentative interpretation.

The fast eddies can be understood using the modal perspective of [88] and [104], who showed that in the two-layer QG model fast, high wavenumber internal modes propagate at phase speeds between the upper and lower zonal-mean wind speeds (i.e $U_2 < c < U_1$). These modes are excited by baroclinic stirring and propagate meridionally away from the baroclinic zone before breaking at their critical latitudes, where they decelerate the flow. Physically, they can be thought of as baroclinic modes, in contrast to the more barotropic external modes that propagate at slower phase speeds. The ratio of the amplitude of the internal modes in the upper layer to their amplitudes in the lower layer, α, is given by [88]

$$\alpha = R_1^2 - R_2^2 - \left[(R_1^2 - R_2^2)^2 + 4\right]^{1/2}, \tag{5.3}$$

where R_1^2 is the zonal-mean PV gradient in the upper layer divided by the upper-layer zonal-mean wind in the reference system moving with the wave and R_2^2 is the zonal-mean PV gradient in the lower layer divided by the lower layer zonal-mean wind in the reference system moving with the wave. This ratio will generally be larger than one, so the EMF transported by the internal mode is larger in the upper-layer of the model. [104] identified the internal modes as dominating the EMF flux in a two-layer primitive equation model.

I interpret the EMF divergence in the lower layer as being due to eddies that are mostly localized to the lower layer and that are also excited by the baroclinic stirring (Note: as in the primitive equation experiments of [3], simulations in which non-linear eddy-eddy interactions were turned off produced a very different EMF structure). Figure 5.10 shows that the stirring is broad and so there is not a clear separation between a stirred region and a propagating region in the lower layer. The propagation of eddies in the lower layer is anyways limited by the weak PV gradient there (dashed line in Figure 5.10) and so the modal perspective cannot be used to

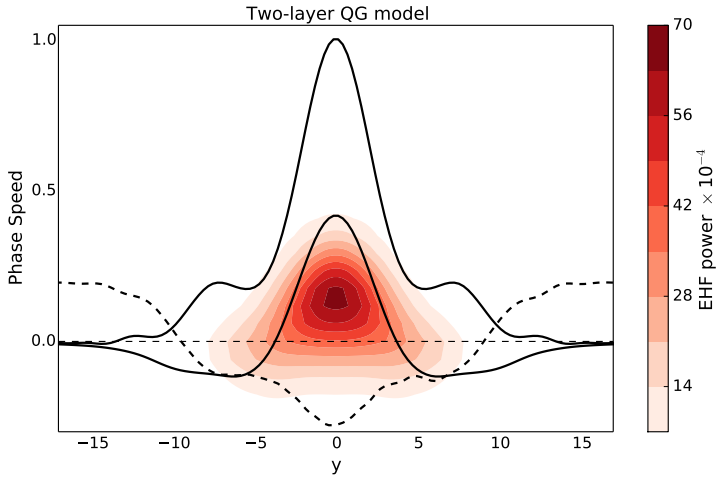


Figure 5.10: Contours show the eddy heat flux co-spectra in the lower layer of the two-layer QG model. The solid lines show the upper and lower layer zonal-mean zonal winds and the thick dashed line shows the lower layer PV gradient. Δc is 0.06.

explain their behavior. Instead, the wide disturbance means that some eddies are generated near their critical lines and accelerate the flow there when they break, as the PV gradient is still negative. There is compensating deceleration in the center of the domain where there is eddy generation but relatively little breaking.

The phase speeds of the lower tropospheric eddies are determined by the phase speeds of the stirring generating them and so the eddies propagate westward with respect to the mean flow, despite the lower layer PV gradient being negative. In fact, the EHF co-spectra shows that the stirring mainly occurs at phase speeds less than U_2, whereas linear theory suggests that the stirring should mostly take place at the steering level of the eddies. I attribute these slower phase speeds to the non-linear inverse energy cascade, which causes the energy-containing eddies to be larger (and slower) than would be expected from linear theory. The difference can be thought of as a measure of the strength of the inverse cascade. That the phase speeds are similar in the $\tau_F = 100$ days experiment implies that the strength of the inverse cascade is independent of friction.

5.7 Conclusion

In this study I have investigated the eddy momentum fluxes in the lower tropospheres of a two-layer QG model, a dry primitive equation model and the southern hemisphere of a reanalysis dataset. The EMF co-spectra are very similar in the two models, showing a dipole structure in the center of the jet, with EMF convergence at phase speeds close to the lower layer jet speed and EMF divergence at slower phase speeds. These regions are bordered by regions of EMF divergence and EMF convergence, respectively. Calculating the spectra as a function of wavenumber shows that long, slow waves are responsible for the EMF divergence, while short, fast waves are mostly responsible for the EMF convergence at the center of the jet. Many of the same features are seen in the co-spectra of the reanalysis data, particularly in austral summer. This suggests that the same fundamental dynamics are at play in the models as well as in the reanalysis data.

I attribute the EMF divergence in the lower troposphere to the weak, negative PV gradient there and to the width of the disturbance which excites the lower tropospheric eddies. Together these mean that the lower troposphere cannot be separated into a stirred region and a propagating region. Instead, eddies which are excited near their critical latitudes by the disturbance break and accelerate the flow there, while the center of the jet is decelerated as eddies form, but do not break there. The EMF convergence at faster phase speeds is due to the internal mode, which mostly propagates on the upper tropospheric potential vorticity gradient. The internal mode accelerates the flow where it forms and decelerates the flow where it breaks. This modal language is natural in the two-layer model, and the similarity between the two-layer model and the GCM and reanalysis data suggests that a similar language might be relevant with more continuous stratification as well.

One of the motivations for this study was the result of Chai et al. that the eddies in the lower troposphere of an idealized GCM diverge momentum when the fric-

tional time-scale is very large [16]. This agrees with the intuition that the vertically-integrated EMFs must cancel in the limit of zero surface friction. I have investigated the approach to this limit using the two-layer model, in which there are no complications due to jet shifts. In these simulations the lower layer EMF divergence increases as the frictional time-scale is increased, with the increased divergence being due to the long waves. Interestingly, the phase speeds of the eddies are essentially the same in the low friction runs as in the runs with Earth-like parameters, which I interpret as indicating that the strength of the inverse cascade is unaffected by friction, likely because there is little room for a cascade to larger scales in Earth-like geometries where the width of the baroclinic zone limits the length scale of eddies.

Due to the fact that the time-mean momentum fluxes in the lower layer are a small residual of fluxes that, at any instant of time, vary over a large range of positive and negative values, as well as the strong coupling between the layers, I have not attempted to develop a quantitative theory for the parameter-dependence of the lower tropospheric EMF divergence. However, the qualitative interpretation presented here says that this dependence is closely tied to the stirring that generates the eddies. Developing a quantitative theory for this stirring is beyond the scope of this study, however the stochastic approach of [29], [25] and others is a promising route to understanding this stirring and the resultant mixing of potential vorticity.

Chapter 6

Applying the Fluctuation-Dissipation Theorem to a Two-Layer Model of Quasi-Geostrophic Turbulence

6.1 Introduction

There is interest in using the Fluctuation-Dissipation Theorem (FDT) to calculate linear response operators for climate models or, more ambitiously, for the climate system itself. Heuristically, the FDT says that the fluctuations of a system in equilibrium can be used to predict how that system will respond to a small perturbation. Perturb a system of the form

$$\frac{d\mathbf{x_e}}{dt} = M(\mathbf{x_e}, t), \tag{6.1}$$

by a small force

$$\frac{d\mathbf{x_f}}{dt} = M(\mathbf{x_f}, t) + \Delta\mathbf{f} \tag{6.2}$$

(I will only consider the case of a time-independent force). The FDT says that the fluctuations of the unperturbed system can be used to calculate a linear response operator, $\mathbf{L}$, with which one can directly compute the response of the time-averaged solution

$$< \mathbf{x_f} - \mathbf{x_e} >= \delta\mathbf{x} = \mathbf{L}\Delta\mathbf{f}. \tag{6.3}$$

Much effort has been devoted to understanding the internal variability, or "fluctuations", in observations and in models, so it is intriguing to be able to use this framework to predict how these systems respond to perturbations.

It is perhaps unsurprising then that the FDT has a relatively long history in the climate science literature, beginning with the seminal work of Leith (1975) [67], followed among others by [5], [73], [35], [97] and [74]. Recently, concerns about the assumptions underlying the FDT and their applicability for the climate system have been addressed ([73]; [35]) and I will be focusing here on the "quasi-Gaussian" formulation of the FDT, in which the linear operator is calculated as

$$\mathbf{L} = \int_0^\infty \mathbf{C}(\tau)\mathbf{C}(0)^{-1}d\tau, \tag{6.4}$$

where the $\mathbf{C}$'s are covariance matrices and τ represents time lags. While non-parametric versions that do not assume multi-variate Gaussian statistics have been described in the literature [21], the practical implementation of more general versions appears to be very formidable. Other options, such as the blended-response algorithm of [1] require information about the underlying dynamical operator. My focus here is on the version that requires only the covariance matrix in an equilibrium state, with no knowledge required of the underlying dynamics that produces these covariance statistics. I refer to this classical formulation as simply the FDT in the following.

The accuracy of the FDT in climate problems of interest remains unclear, however. [35] found good agreement between their FDT estimates and the response of

an atmosphere-only General Circulation Model (GCM) to heating perturbations; this appears to be the most promising result to date. [97] were not able to obtain accurate estimates for the response of a dry dynamical core to various zonally symmetric torques using a Principal Oscillation Pattern (POP) analysis, rather than the full FDT. Whether the full FDT would work better in this case is unclear. Previous work has also focused on more idealized systems, such as the Lorenz-96 model and variants of Burger's equation (see e.g., [73]), in order to develop the theoretical framework of the FDT and to compare alternative formulations. Hence there is room for work on intermediate complexity systems with large numbers of degrees of freedom, motivated by climate change issues, but in which the covariance statistics are more easily generated than for primitive equation models on the sphere. These intermediate systems can also allow for more careful study of how best to choose a basis on which to project the evolution of the model state and how best to truncate this basis so that it is small enough to allow robust estimation of the covariance matrix. The goal is to avoid subjective choices that complicate the testing of the robustness and accuracy of the FDT.

With this motivation, in the following work I have applied the FDT to a turbulent, baroclinically unstable jet in a two-layer quasi-geostrophic (QG) model. The two-layer model is simple enough that large amounts of data can be gathered relatively quickly, ensuring robust statistics, and conduct extensive sensitivity tests. At the same time, its simplicity makes it a strict test of the FDT's value, to see if it can provide estimates for the model's response to forcings that are accurate both qualitatively and quantitatively, effectively serving as a parameterization for the transient eddy momentum fluxes that determine the model's response.

Moreover, as mentioned in chapter 5, the two-layer model captures many essential features of atmospheric circulation in the midlatitudes and so is also of much scientific interest. A particular motivation for this work is the presence of annular mode-like

variability in this model. Annular modes are the dominant mode of variability in the zonal-mean winds in the extra-tropics and qualitative application of FDT-like thinking connects the autocorrelation time scale of this mode to the response of the midlatitude circulation to forcing (e.g., [33]; [97]; [12]). This suggests that there is an FDT-like connection between the autocorrelation of the annular modes and the response of the midlatitude circulation to forcing, though previous applications of the FDT have not been quantitatively successful ([97]; F. C. Cooper and P. H. Haynes 2013, personal communication). If the FDT does hold, it would be concerning as many GCMs have overly persistent annular modes, potentially leading to overestimates of the actual response of midlatitudes to small perturbations, with consequences for the response of midlatitude circulation to the ozone hole as one important example.

Finally, several papers have investigated the complex structure of the autocorrelation of the annular modes ([33]; [140]; [138]). In particular, [140] showed that this autocorrelation includes high and low frequency components which reflect the effects of positive and negative eddy feedbacks. This may explain the lack of quantitative results in [97], as simplified methods which effectively assume the structure of the correlations are unlikely to give accurate estimates, and also justifies the use of the full FDT, which integrates over different time scales.

The rest of this chapter is structured as follows. The methodology is presented in the next section followed in section 6.3 by an examination of how the model responds to small perturbations and how its behavior varies as the supercriticality of the control climate's jet is varied. The results of the FDT calculations are then presented in section 6.4 before the chapter ends with conclusions.

6.2 Methodology

6.2.1 Model formulation

The same non-dimensional two-layer QG model was used as in chapter 5, with the same control parameters: the jet width σ is 3.5, β is 0.196, τ_f is $\sim$15, τ_d is $\sim$100 and ν is 0.01. These are non-dimensionalized versions of the parameters used by [140], who showed that they produce qualitatively realistic annular mode variability. The time-averaged zonal-mean zonal winds and the time-averaged zonal-mean eddy heat and momentum fluxes are shown in Figure 6.1.

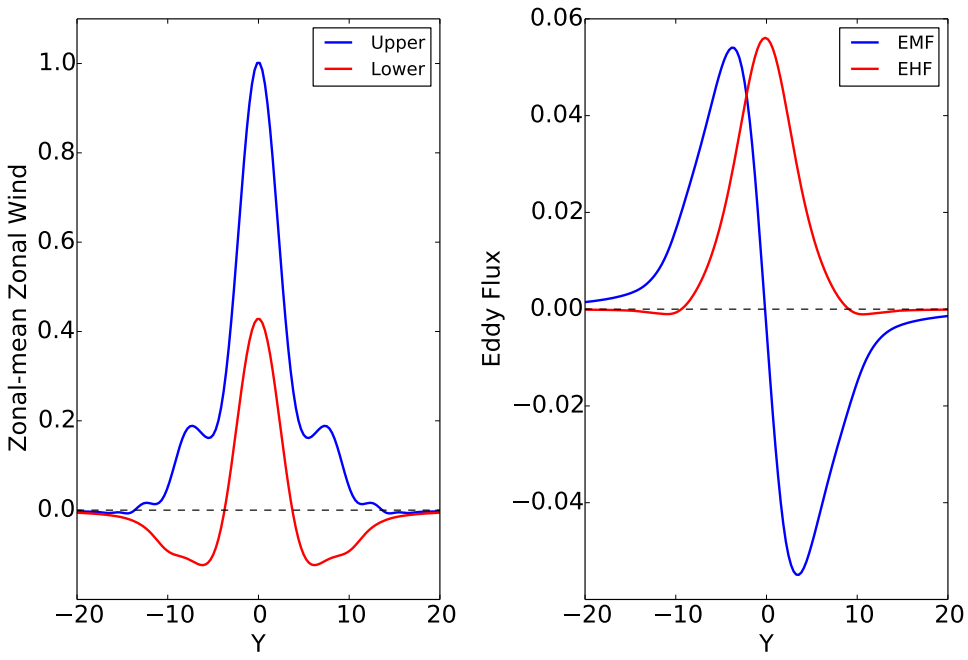


Figure 6.1: (left) Time-averaged zonal-mean zonal wind profiles for both layers from a 10^5-day integration of the two-layer model using the parameter settings of [140] and (right) the time-averaged zonal-mean EMF and EHF.

This model is also similar to that used by DelSole (1996) in a study using POP analysis [24]. DelSole found that the empirical operator obtained by the POP analysis

depends on time-lag, inconsistent with the Markov model approximation underlying that technique. The FDT does not share this limitation.

6.2.2 Control simulations and perturbations

In order to estimate the covariance statistics the model was integrated for 10^6 model days, with the first 10^3 model days discarded to ensure that the model had equilibrated. Data was recorded every four model days (i.e every 0.8 Earth days). Tests indicated that higher frequency sampling produces no significant change in the results. The resulting dataset was then divided into an ensemble of 10 members, each representing approximately 10^5 model days of data, to estimate the sampling error.

The most general zonally symmetric perturbation in this model can be expressed as zonally symmetric source terms in the upper and lower layer potential vorticity equations. For a heating perturbation Q and upper and lower layer torques (f_1, f_2),

$$\frac{\partial \overline{q_1}}{\partial t} = ... - \frac{\partial f_1}{\partial y} + Q, \tag{6.5a}$$

$$\frac{\partial \overline{q_2}}{\partial t} = ... - \frac{\partial f_2}{\partial y} - Q. \tag{6.5b}$$

Equivalently, one can think of forcing the barotropic and baroclinic components of the flow (the sum and difference of the upper and lower layers). The response to heating is equivalent to the response to a purely baroclinic zonal force with $f_1 = -f_2$, and the baroclinic case can be thought of as either the response to heating Q or to a baroclinic zonal force. I consider pure barotropic and pure baroclinic forcing. The FDT prediction for a more general perturbation (momentum forcing in the upper layer only, for example) can be obtained from the linear superposition of barotropic and baroclinic special cases.

I describe the baroclinic case first. Given the knowledge that the dominant mode of variability in this model is annular mode-like ([140]; see also Figure 6.3 below),

consisting of a meridional shift in the winds and storm track, just as in the atmosphere, the latitudinal structure of the forcing was designed to give the FDT the best chance to generate robust responses. To do this, I choose Q proportional to the derivative of the radiative equilibrium temperature field. For small perturbations this is equivalent to a meridional shift in the baroclinic zone:

$$Q = Q_0 \frac{\partial \psi_R}{\partial y}. \tag{6.6}$$

As described below, when performing the FDT computations the model output was decomposed into Empirical Orthogonal Functions (EOFs). In order to perform this decomposition a basis with which to compute the covariance matrix and a corresponding norm are required. Since the control and perturbed models are both zonally symmetric only the EOFs of the zonal mean circulation are required by the FDT. Although the numerical model is formulated using potential vorticity as the prognostic variable, better results are obtained when performing the FDT calculations using the zonal-mean zonal wind to define the basis and norm. Using the zonal-mean potential vorticity variance as the norm when computing the EOFs results in EOFs with more fine-scale structure than if the zonal-mean zonal wind variance is used as the norm. This fine-scale structure magnifies errors in the FDT calculations and so the results are cleaner when using the zonal-mean zonal wind. To directly apply the FDT formalism in this basis the potential vorticity forcings need to be converted into zonal wind tendencies (just as in [97]). For the baroclinic forcing the result is

$$\frac{\partial \overline{u}_k}{\partial t} \equiv (-1)^k F, \tag{6.7}$$

where k indicates the model level and $F(y)$ is obtained by solving

$$\left(\frac{\partial^2}{\partial y^2} - 2 \right) F = \frac{\partial Q}{\partial y} = Q_0 \frac{\partial^2 \psi_R}{\partial y^2}. \tag{6.8}$$

This zonal wind tendency is shown in panel *(b)* of Figure 6.2. Physically, it forces a southward shift of the baroclinic component of the radiative equilibrium jet (see panel *(a)*) and the response to this perturbation is shown in *(c)* of the same figure.

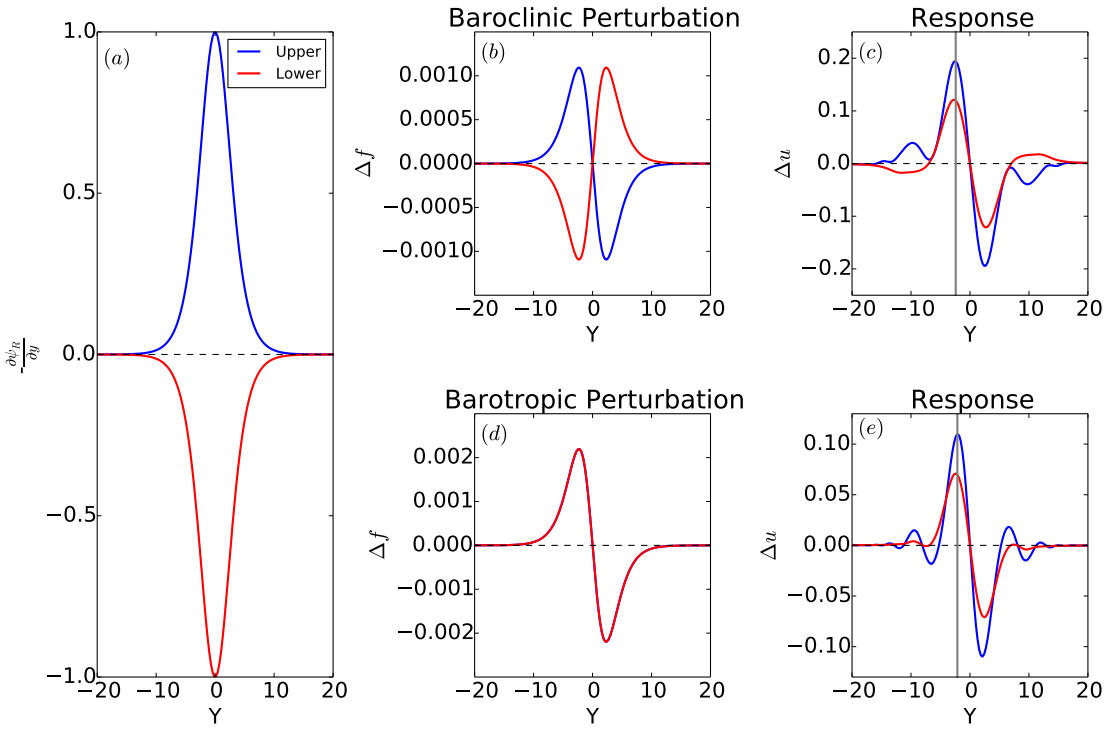


Figure 6.2: *(a)* Profile of $\frac{\partial \psi_R}{\partial y}$; *(b)* the baroclinic perturbation to the zonal momentum equations applied to the two-layer model and *(c)* the resulting model response (the zonal wind tendency is inverted from the thermal forcing); *(d)* the barotropic perturbation (note: the perturbations to the upper and lower layers plot on top of each other) and *(e)* the model response. The vertical gray lines in panels *(c)* and *(e)* show the position of the $max\Delta u$ metric.

The relationship between Q and the zonal tendency F accounts for the effects of the mean meridional circulation. In the barotropic case of equal zonal forces in the two layers there is no induced meridional circulation and the imposed potential vorticity tendency is proportional to the derivative of the zonal force in both layers; that is,

$$\frac{\partial \overline{u_k}}{\partial t} = f_k, \tag{6.9}$$

where f_k is the same as in equation 6.5a. The profile of this force was chosen to be similar to that obtained from equation 6.8 for the baroclinic zonal wind tendency by simply setting f_1 and f_2 to

$$f_1 = f_2 = f_0 \frac{\partial^2 \psi_R}{\partial y^2}. \tag{6.10}$$

This zonal wind tendency represents a southward shift of the barotropic component of the radiative equilibrium jet and is shown in panel *(d)* of Figure 6.2. The response is shown in *(e)*; note that the barotropic and baroclinic forcings produce qualitatively similar equivalent barotropic responses.

The amplitude of the forcings must be small enough that the responses are in the linear regime and large enough that these linear responses can be isolated accurately from the model's variability. I have found that $f_0 = Q_0 = 0.01$ is safely in this range, verifying that the changes in the responses are negligible when the forces are increased or decreased by a factor of 2. Forces of this strength shift the baroclinic zone by roughly 24% of the half-width of the jet (σ). Tests in which the domain size was doubled but the resolution was kept constant indicated no sensitivity of the responses to domain size.

After performing these calculations with the control parameters, the simulations were repeated while varying β in increments of 0.05 from the original value of roughly 0.2 up to a value of 0.4 (when β is decreased from 0.2 the width of the domain begins to affect the model's response). This induces substantial changes in the model behavior, which are discussed in section 6.3, and was done in order to test how the FDT fared under different parameter settings. In every case the forces were again halved and doubled to verify that the responses are linear functions of the perturbation strength.

6.2.3 Regularization Strategy

As has been discussed by, for example, [35], errors in the calculation of the linear operator $\mathbf{L}$ are a function of the length of the available data, n, and the "effective" number of degrees of freedom [78]. The former simply arises from the central limit theorem, which says that the errors in the covariance estimates will be proportional to $1/\sqrt{n}$. The second is a result of the $\mathbf{C}(0)^{-1}$ term. For a system with many degrees of freedom $\mathbf{C}(0)$ is likely to be an ill-conditioned matrix, resulting in large errors when its inverse is estimated. However, only a subset of the total degrees of freedom are relevant for the FDT computation, while the other degrees of freedom simply decay and so cause errors in the estimation of $\mathbf{C}(0)$. The goal of regularization is to minimize the effects of the latter degrees of freedom.

The most commonly used way of regularizing the $\mathbf{C}(0)$ matrix in FDT studies is to truncate the number of included degrees of freedom. This strategy involves a balance between including enough dimensionality to capture the behavior of the data and not including unnecessary dimensionality. To do this I have followed previous works by projecting the data onto the EOFs and then truncating the number of EOFs included in the calculations.

The two-layer model with a climate that is symmetric about the center of the channel has two types of zonal-mean zonal wind EOFs: half are symmetric about the center of the channel and the other half are anti-symmetric. The leading EOF has an anti-symmetric annular mode-type structure, the next leading EOF has a pulsing symmetric structure, and so on. Symmetric perturbations and responses only project onto the symmetric EOFs while anti-symmetric perturbations and responses only project onto the anti-symmetric EOFs. Hence only the anti-symmetric EOFs have been used here as the perturbations described above are both anti-symmetric. For some cases the higher ranking EOFs were not purely symmetric or anti-symmetric due to sampling issues, but they were still recognizably symmetric or anti-symmetric

and so were binned accordingly. Tests indicated that this separation did not affect the results.

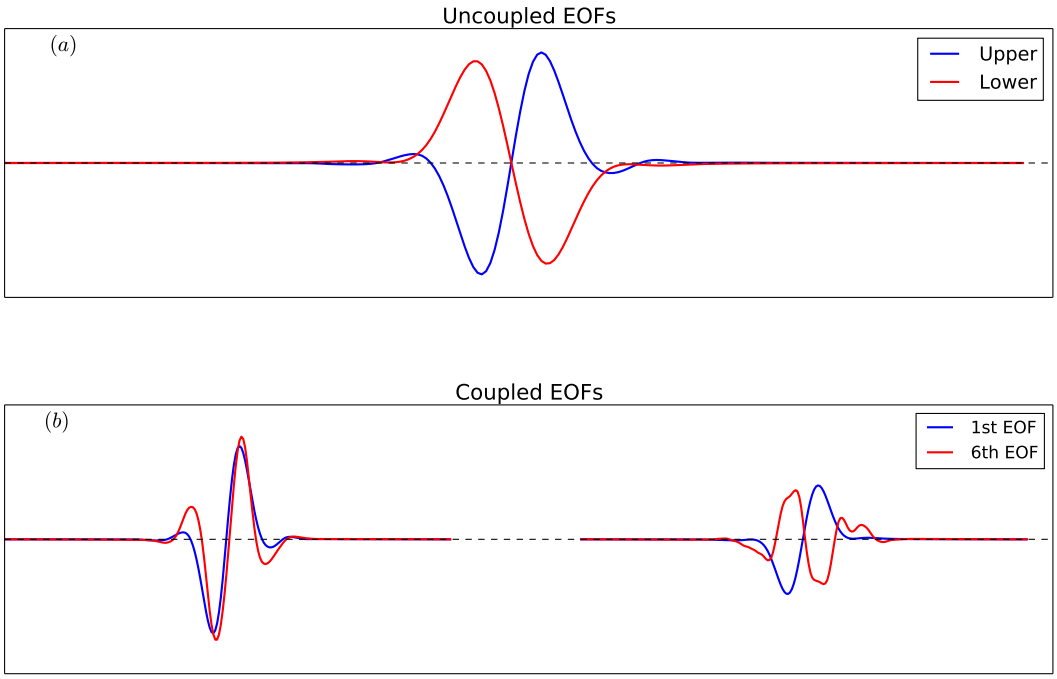


Figure 6.3: *(a)* The leading uncoupled EOF in each layer when $\beta = 0.2$; *(b)* the leading coupled EOF (blue) and the sixth anti-symmetric coupled EOF (red) for the same case. The lines to the left correspond to the lower layer and the lines to the right correspond to the upper layer.

In addition to this partition I initially considered two ways of defining the EOFs: calculating them separately for each layer or for both layers simultaneously. The former will be referred to as "uncoupled EOFs" and Figure 6.3*(a)* shows the leading EOF calculated for each layer separately. The latter will be referred to as "coupled EOFs" and Figure 6.3*(b)* shows the leading EOF calculated using both layers simultaneously.

The calculations below were carried out with both kinds of anti-symmetric EOF but the calculations using the coupled EOFs were expected to have less error than those carried out with the uncoupled EOFs as the lag-zero covariance matrix of the

coupled EOFs is likely to be more well-conditioned than that of the individual EOFs, being diagonal by definition. A physical interpretation for this is the strong coupling between the upper and lower layers through the potential vorticity; hence treating the layer EOFs as independent degrees of freedom produces a poorly conditioned covariance matrix. The results of calculations using uncoupled EOFs are not shown here, but this was indeed the case.

Having defined the EOFs, the question raised in the introduction of this chapter of how many EOFs to retain remains. This is a central concern whenever the FDT is applied to large systems and is discussed in detail in section 6.4.1.

6.2.4 Testing Gaussianity

The formulation of the FDT which I have used assumes that the system is Gaussian. This is unlikely to be the case in practice, but the relationship between non-Gaussian behavior and bias in FDT estimates is still unclear. I have not attempted to explore this question rigorously but to help address this issue I have used Mardia's test to calculate the multi-variate skewness γ and kurtosis K, and so test for multivariate Gaussianity. These are given by:

$$\gamma = \frac{1}{n^2}\sum_{i=1}^{n}\sum_{j=1}^{n}[(\mathbf{x}_i - \bar{\mathbf{x}})^T\mathbf{C}(0)^{-1}(\mathbf{x}_j - \bar{\mathbf{x}})]^3, \tag{6.11a}$$

$$K = \frac{1}{n}\sum_{i=1}^{n}[(\mathbf{x}_i - \bar{\mathbf{x}})^T\mathbf{C}(0)^{-1}(\mathbf{x}_i - \bar{\mathbf{x}})]^2, \tag{6.11b}$$

where $\mathbf{x}$ is the state vector of length d and n is the number of data points in each ensemble member (10^5) [136]. I have calculated γ and K for each ensemble member separately and then averaged the results. Overbars denote mean values. With these

definitions two test statistics can be defined, T_γ and T_K,

$$T_\gamma = \frac{n}{6}\gamma, \tag{6.12a}$$

$$T_K = \sqrt{\frac{n}{8d(d+2)}}\left[K - d(d+2)\right]. \tag{6.12b}$$

For a multivariate normal system T_γ will have a χ^2 distribution with $\frac{1}{6}d(d+1)(d+2)$ degrees of freedom while T_K will have a normal distribution with mean zero and standard deviation one [136]. Hence once T_γ and T_K are calculated p values can be calculated to test the assumption of Gaussianity: if the p value of each of these is less than 0.05 the null hypothesis that the data is normally distributed can be rejected.

6.2.5 Another Computational Note

Estimating $\int_0^T \mathbf{C}(\tau)d\tau$ is very time-consuming: the most obvious algorithms require $O(d^2nr)$ operations, where n and d are as before and r is the number of datapoints corresponding to a lag T. In an unpublished manuscript Cooper and Haynes have shown that this can be reduced to an $O(nd^2)$ calculation by a suitable rearrangement of the double summation over the r time lags and n data points. As it has not previously been published the details of this algorithm are given in appendix A.

6.3 Model Results

6.3.1 Behavior of the model as β is increased

Varying β substantially affects the model's behavior, even before perturbations are applied. For instance, the time-averaged behavior of the zonal jets changes noticeably as β is increased. In the upper layer the jet, which is similar to the radiative equilibrium jet when $\beta = 0.2$, becomes narrower and strengthens, while adding structure in the "wings" (top panel of Figure 6.4). In the lower layer the jet becomes nar-

rower but its strength does not change significantly as β is increased (bottom panel of Figure 6.4).

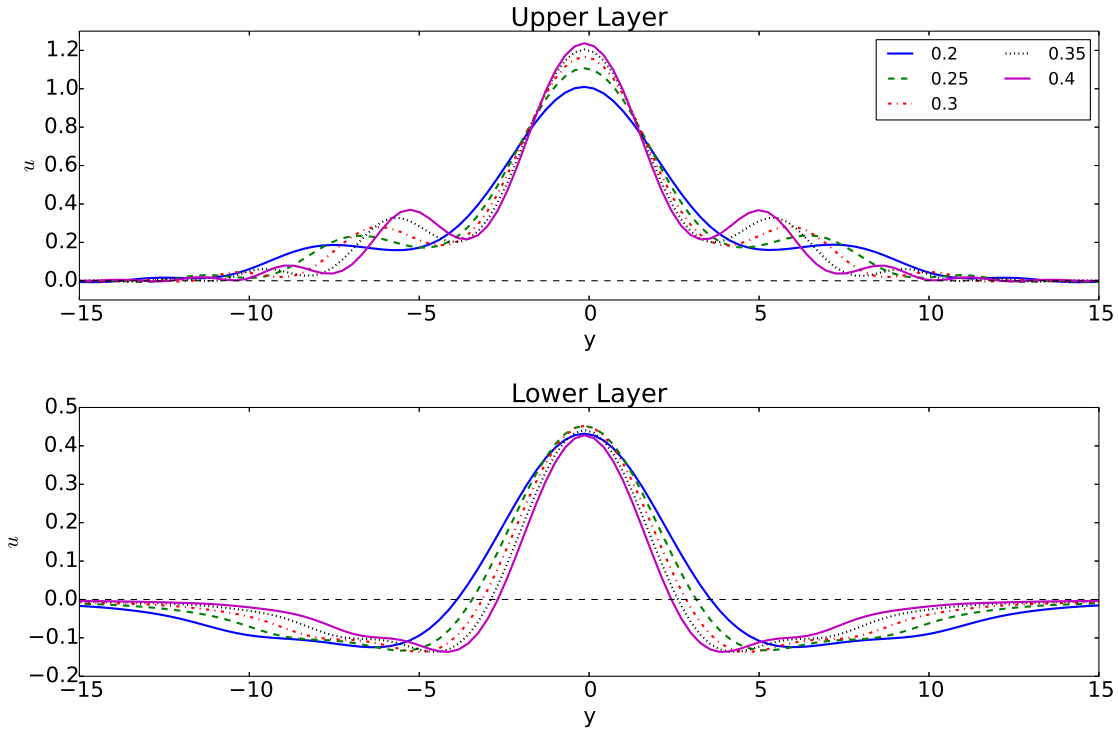


Figure 6.4: Comparison of the time-averaged zonal-mean zonal winds as β is varied from 0.2 to 0.4. (top) The upper layer and (bottom) the lower layer.

From an FDT perspective the variability of the model is centrally important and this is also affected by increasing β, with the flow becoming more persistent. This can be seen in Figure 6.5, which plots the autocorrelation of the first principal component for the different values of β. Clearly, the annular mode becomes more persistent as β is increased, so that when $\beta = 0.4$ the autocorrelation oscillates significantly even at very long lags. This is associated with the development of a low-frequency peak in the eddy momentum forcing spectrum as β is increased (not shown). Another noticeable feature, which may be related, is that the transition between the negative eddy feedback, which causes the autocorrelation to decay rapidly, and the positive eddy feedback, which causes the autocorrelation to decay less rapidly, takes place

sooner and becomes noticeably sharper as β is increased (see inset of Figure 6.5; also see [140] for a discussion of the positive and negative eddy feedbacks).

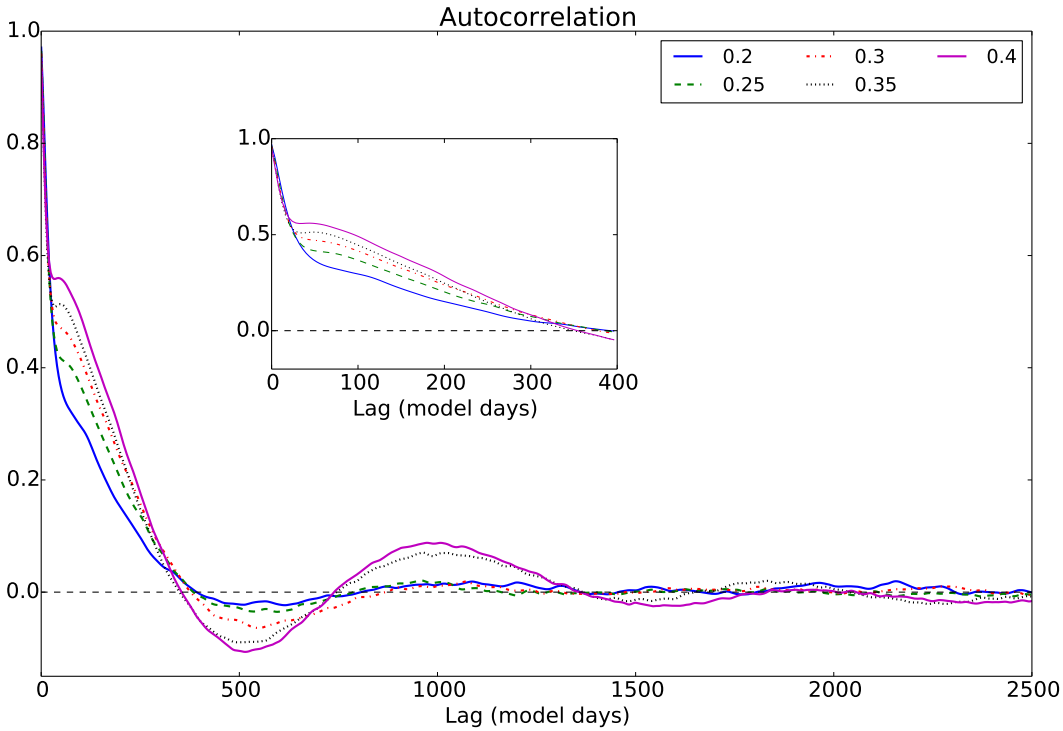


Figure 6.5: Autocorrelation of the first principal component as β is increased (5 model days $\equiv$ 1 Earth day). The inset is a close-up of lags zero to 400.

In addition to becoming more persistent as β is increased, the model also becomes less Gaussian. This can be seen in the left panels of Figure 6.6, which plot the multivariate skewness and kurtosis test statistics for the first six coupled anti-symmetric EOFs for three values of β (note: in this and in all subsequent figures the plus/minus one standard deviation envelope is calculated by dividing the standard deviation of the ensemble estimates by $\sqrt{10}$). The skewness increases monotonically with β and, while the kurtosis does not follow as clear a trend, the $\beta = 0.2$ data is closest to the 95% confidence interval. In all cases the data shows significant departures from Gaussianity. This is concerning for the FDT, which of course assumes that the data is at least approximately Gaussian, and may be of relevance to the results below.

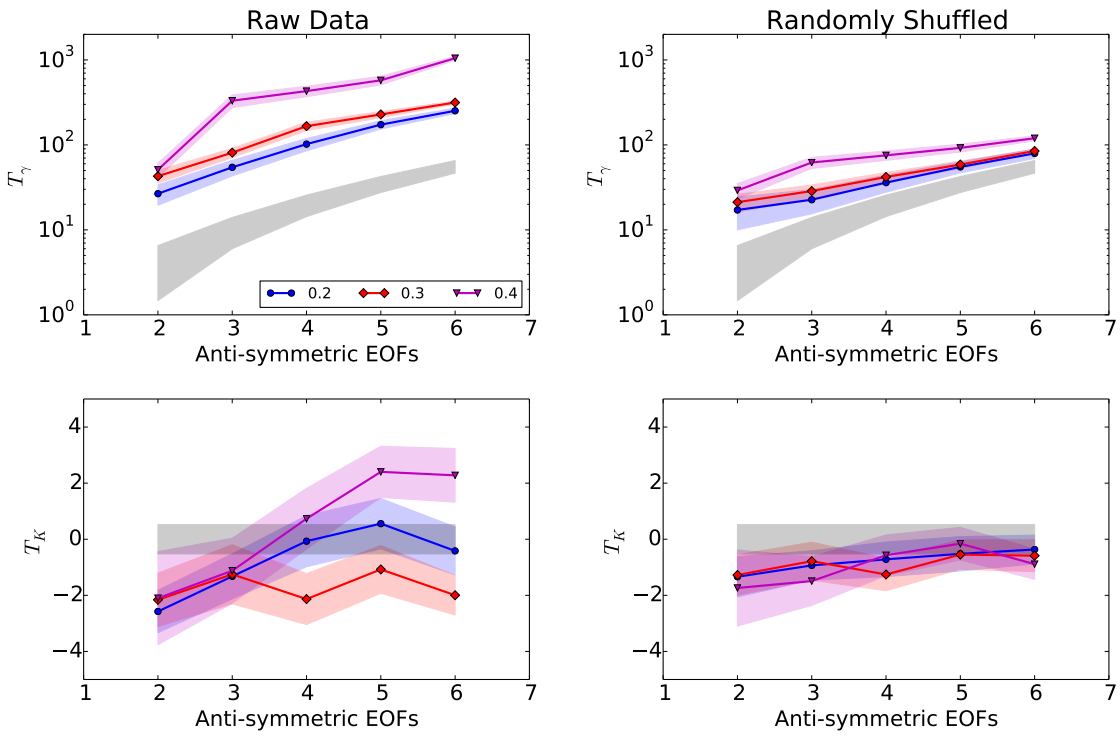


Figure 6.6: (left) Ensemble-mean estimates of the multivariate skewness, T_γ (top), and kurtosis, T_K (bottom), test statistics as a function of the number of included anti-symmetric EOFs for different values of β. The gray shaded regions show the 95% confidence intervals corresponding to a 10-member mean sample multivariate skewness and kurtosis, when the underlying data are Gaussian and these statistics are distributed as explained in section 6.2.4. The colored shading shows plus/minus one standard deviation divided by $\sqrt{10}$ of the estimates. (right) As in (left), but where the principal component time series are randomly disordered to remove the coupling between EOFs.

To test if the non-Gaussianity arises from the joint probability distributions or if the univariate probability distributions for the individual modes are non-Gaussian, I have removed the coupling between modes by randomly disordering each of the principal component time series. This substantially reduces the departures from Gaussianity (see right panels of Figure 6.6), though the data is still not quite Gaussian. There is also less dependence on β. The interactions between modes thus explain much of the departures from Gaussianity, as well as the increasingly non-Gaussian behavior as β is increased.

6.3.2 Model Responses

The model responses to the two perturbations in the initial setting with $\beta = 0.2$ are shown in panels *(c)* and *(e)* of Figure 6.2. In both cases the response is anti-symmetric, has the same sign in each layer and is stronger in the upper layer than in the lower layer. There is also a significant response in the wings in each case, suggesting that the response involves other aspects of the model besides the annular modes (which have little structure in the wings in this parameter setting). The gray lines in panels *(c)* and *(e)* mark the maximum of the model responses; a criterion which I have used to evaluate the performance of the FDT is the estimate of the response at these locations, which I term "$max\Delta u$". This criterion is relevant if one is more interested in capturing the magnitude of the responses in the center of the domain than in the wings.

As β is increased the responses become stronger and narrower. Focusing on the barotropic perturbation, there is a clear change in strength, shown by the black lines in panels *(a)* and *(c)* of Figure 6.7, which plot $max\Delta u$ in each layer versus β (note the near linear relationship between the two variables). More detail concerning the structure of the responses is given by the black lines of Figure 6.8, which show that besides the change in strength, the response is narrower in the center and stronger in the wings as β is increased. The baroclinic responses can be seen in Figure 6.17 and are similarly affected by increasing β.

These variations are partly the result of the changing role of eddies in determining the model's response. To demonstrate this, I have repeated the experiments with the non-linear terms in the model removed, eliminating the transient EMFs, so that the balance in the model is between the forcing, the Newtonian relaxation and the friction. Figure 6.9 compares the resulting "no-eddy" responses to the two perturbations with the full model responses in the $\beta = 0.2$ and $\beta = 0.4$ cases (the no-eddy responses are independent of β). For the barotropic perturbation the $\beta = 0.2$ case is actually quite

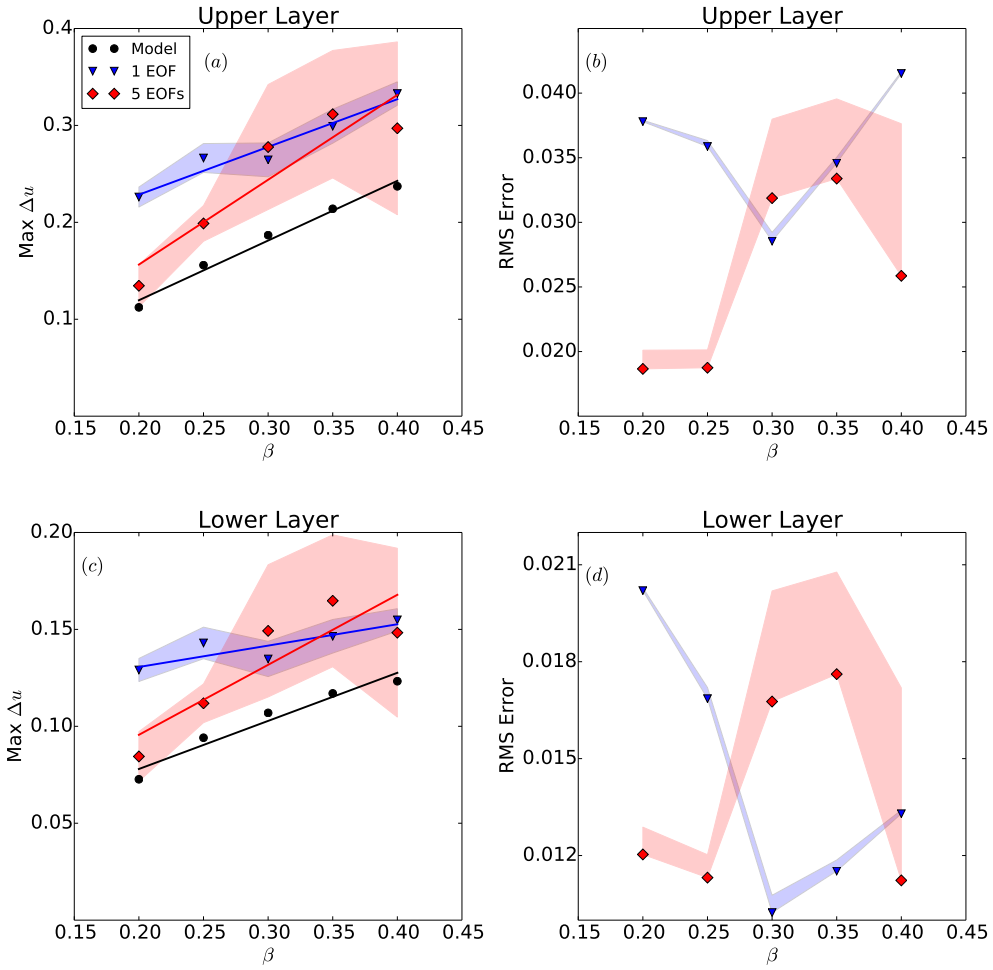


Figure 6.7: *(a)* Variation of $max\Delta u$ as β is increased (black circles) and the corresponding ensemble-mean FDT estimates for the upper layer using the leading EOF (blue triangles) and the first five antisymmetric EOFs (red diamonds). The shading is the plus or minus one standard deviation envelope while the straight lines represent linear least squares fits to the data. *(b)* As in *(a)*, but for the RMS error instead of $max\Delta u$. *(c)*, *(d)* As in *(a)*, *(b)*, but for the lower layer.

similar to the no-eddy response, with the eddies simply acting to amplify and broaden the response in the center of the domain slightly as well as to add structure in the wings. This resemblance may be related to the similarity between the time-mean jet and the radiative equilibrium profile in this setting. However, as β is increased the response of the full model changes (red lines in Figure 6.9) while the no-eddy response

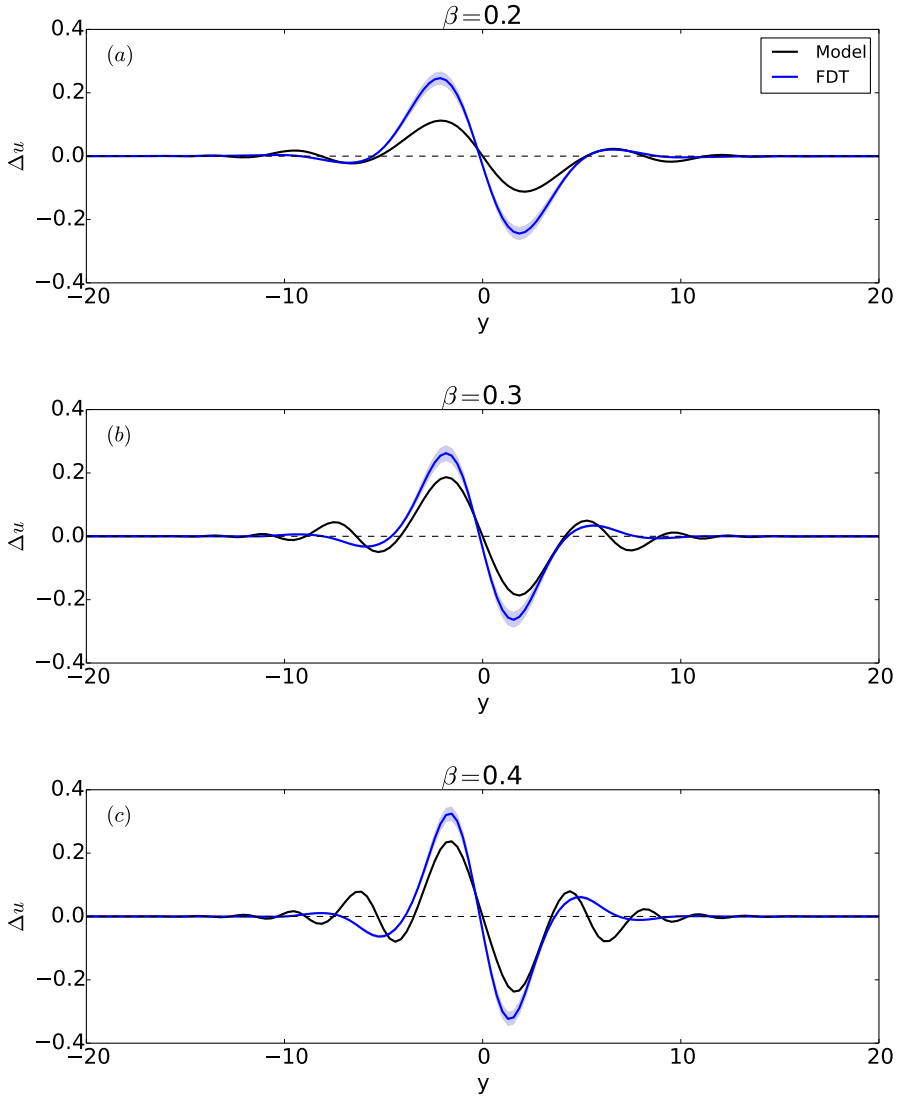


Figure 6.8: Comparison of upper-layer model responses to the barotropic perturbation for three values of β (black lines) and ensemble-mean FDT estimates using the leading coupled EOF (blue lines) in each case. The shading is plus/minus one standard deviation.

is unaffected, showing that eddies increasingly push the full model's response away from the no-eddy response. In the baroclinic case there is no response in the lower layer when eddies are turned off, so that no matter what value β takes eddies play a large role in determining the response of the model. The FDT will have to capture this changing eddy behavior.

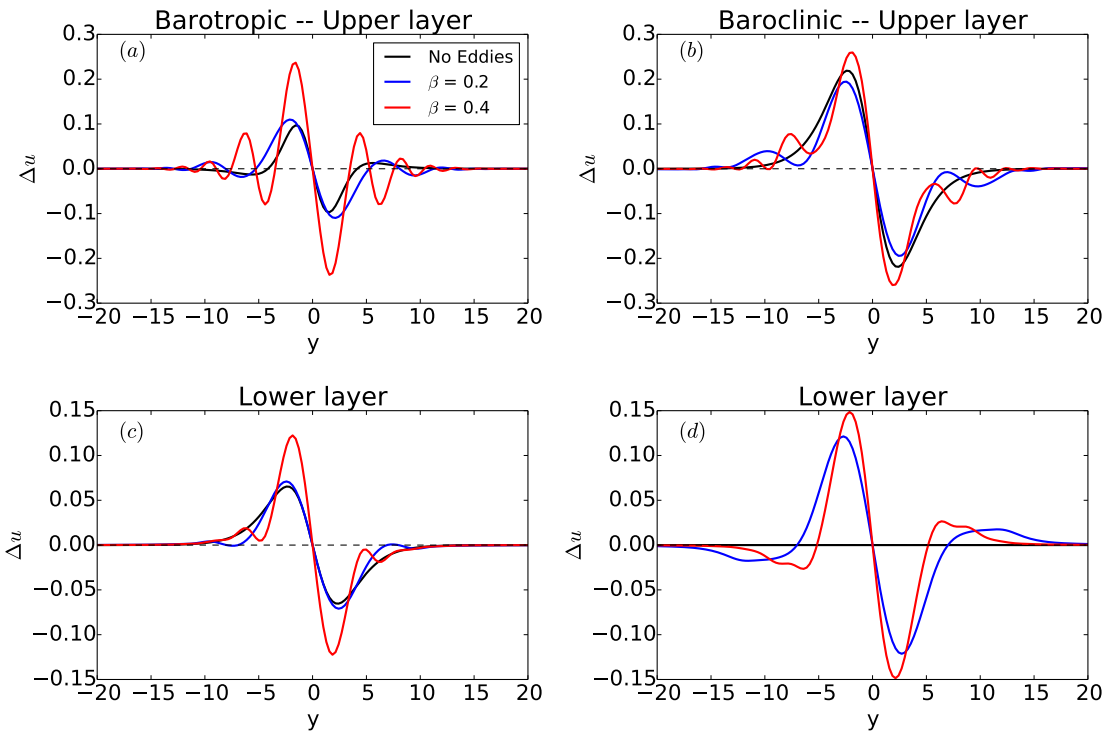


Figure 6.9: *(a)*, *(c)* The model response to the barotropic perturbation without eddies in black, the model responses with eddies and $\beta = 0.2$ in blue and $\beta = 0.4$ in red. P*(c)*, *(d)* As in *(a)*, *(b)*, but for the baroclinic perturbation.

6.4 FDT Calculations

6.4.1 Choosing how many EOFs to retain

Making an appropriate choice of how many degrees of freedom to retain is crucial for producing accurate FDT estimates. Given that the model responses have already been generated, an obvious choice would be to keep only those EOFs onto which these responses project; however, the aim is to decide how many EOFs to retain a priori, without resorting to running the model first. This is part of the motivation for using the FDT in the first place.

As can be seen from Figure 6.10, the leading EOF explains between 65% and 75% of the variance for every value of β, quantifying the dominance of the annular mode in

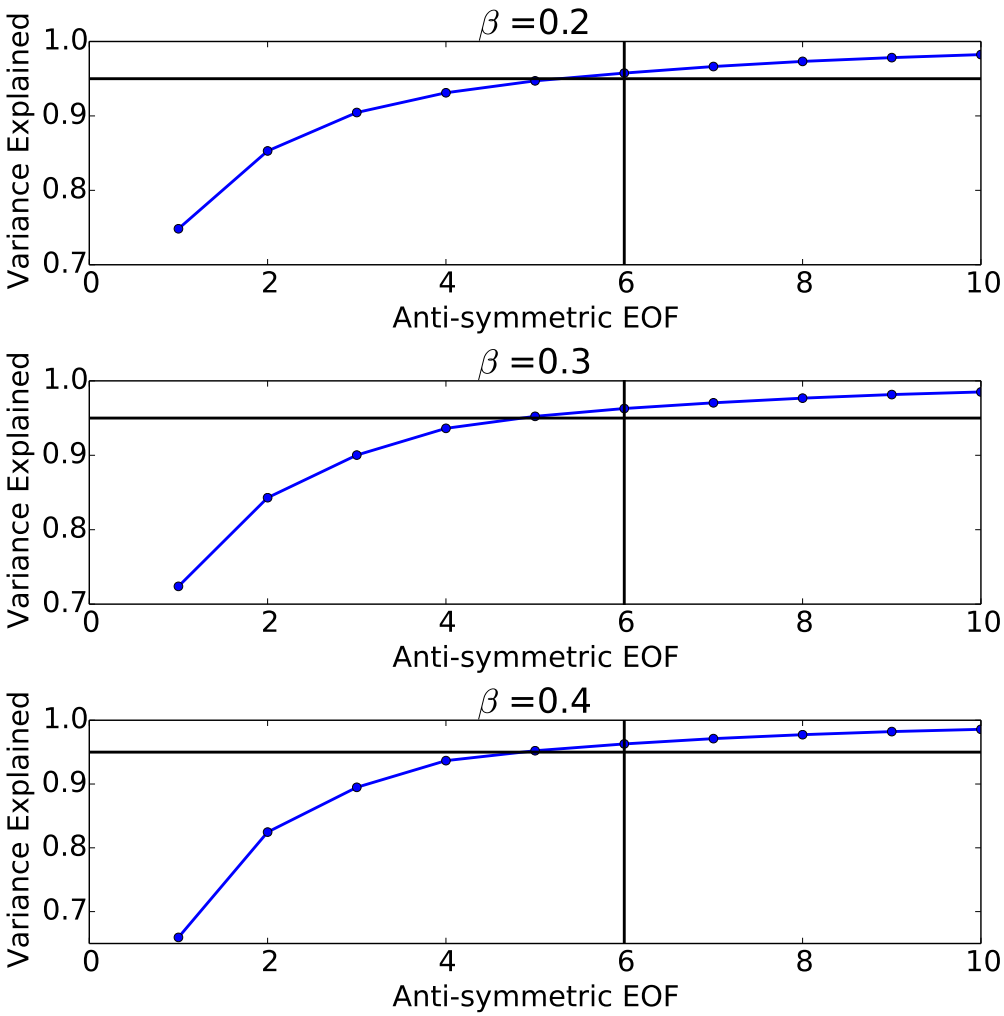


Figure 6.10: The cumulative variance explained by the anti-symmetric EOFs for three values of β. The horizontal black lines mark the 95% line while the vertical black lines denote the first EOF which was not well separated.

this model and suggesting that the most obvious strategy would be to retain only the leading EOF in each case. This is also appealing owing to the hypothesized connection between the response of the midlatitudes to perturbations and the autocorrelation time scale of the annular modes, and so this is the first strategy I have adopted. However, given that the responses have significant structure in the wings it is likely that more EOFs are required for accurate FDT calculations. There are then two a priori criteria which could be used to decide how many EOFs to retain: *(1)* determine

how many EOFs are well resolved and discard the rest; or *(2)* retain the minimum number of EOFs required to explain some threshold of variance. Note that these are likely to be related: EOFs which explain significant variance will be excited more often and hence be better resolved. However, the choice of threshold is subjective and so I have focused on the first criterion.

To determine how many EOFs were well resolved I have followed [24] and calculated how many EOFs were well-separated by the [82] criterion. Here well-separated means that the separation between the eigenvalues corresponding to the EOFs is greater than the sampling error in the eigenvalues themselves. More explicitly, I calculated the value of S_n for each eigenvalue λ_n:

$$S_n = \frac{2\lambda_n}{\lambda_{n-1} - \lambda_{n+1}}. \tag{6.13}$$

From Figure 6.5 the decorrelation time is of order 1000 model days and each ensemble member contained 10^5 model days so the relative error, ϵ, was of order 10%. I used this to define an anti-symmetric, coupled EOF as well-separated when $\epsilon S_n < 1$ and the vertical black lines in Figure 6.10 mark for each value of β the first EOF which was not well separated by this criterion. In every case only the first five EOFs were well separated. The horizontal black lines in Figure 6.10 also show that the first five EOFs explained roughly 95% of the variance in every case. For comparison, previous FDT studies have typically retained between 90 and 99% of the variance ([35]; [97]; [30]).

This is a plausible criteria, which can be used without considering the model responses, but there is a problem when applying this criterion to the case of a baroclinic perturbation. Returning to Figure 6.2, the baroclinic perturbation produces an equivalent barotropic response. This response projects strongly onto the leading EOF but the perturbation does not and instead projects strongly onto the sixth EOF. Examin-

ing the structure of the EOFs shows that for every value of β this corresponds to an "equivalent" baroclinic EOF (layer values have opposite sign but different magnitude; see red line in panel *(b)* of Figure 6.3), in contrast to the first five EOFs which are equivalent barotropic. Hence it is unsurprising that this EOF was poorly resolved (note that it is not as smooth and anti-symmetric as the leading EOF) and does not explain much variance, as the equivalent baroclinic variability of the two-layer model is overwhelmed by the equivalent barotropic variability. In every case the sixth EOF also decorrelates very quickly, typically in one or two model days, further suggesting that it is not being resolved from the noise and so will cause problems for the FDT.

Given the evident sampling error, it is clearly not desirable to include the sixth EOF in the calculations, however it appeared to be necessary for the baroclinic case. As such, for the barotropic case I only retained the first five EOFs while in the baroclinic case the calculations were performed using both five and six EOFs.

6.4.2 Barotropic Perturbation

1 EOF

I begin the presentation of the results by discussing how well the model responses to the barotropic perturbation were estimated using the leading EOFs. As has been mentioned, one of the motivations for this study was the hypothesis that the autocorrelation time scale of the annular modes controls the strength of the response of the midlatitudes to small perturbations. In the context of the FDT, this amounts to saying that the integral of the annular mode autocorrelation can give an accurate estimate of the model's response.

To test this, the blue lines in Figure 6.8 compare the ensemble-mean FDT estimates of the upper layer responses using the leading EOFs to the true responses for three different values of β. In each case 2000 model time-units, or 400 Earth days, was used as the upper limit T. This upper limit was chosen as the autocorrelation of

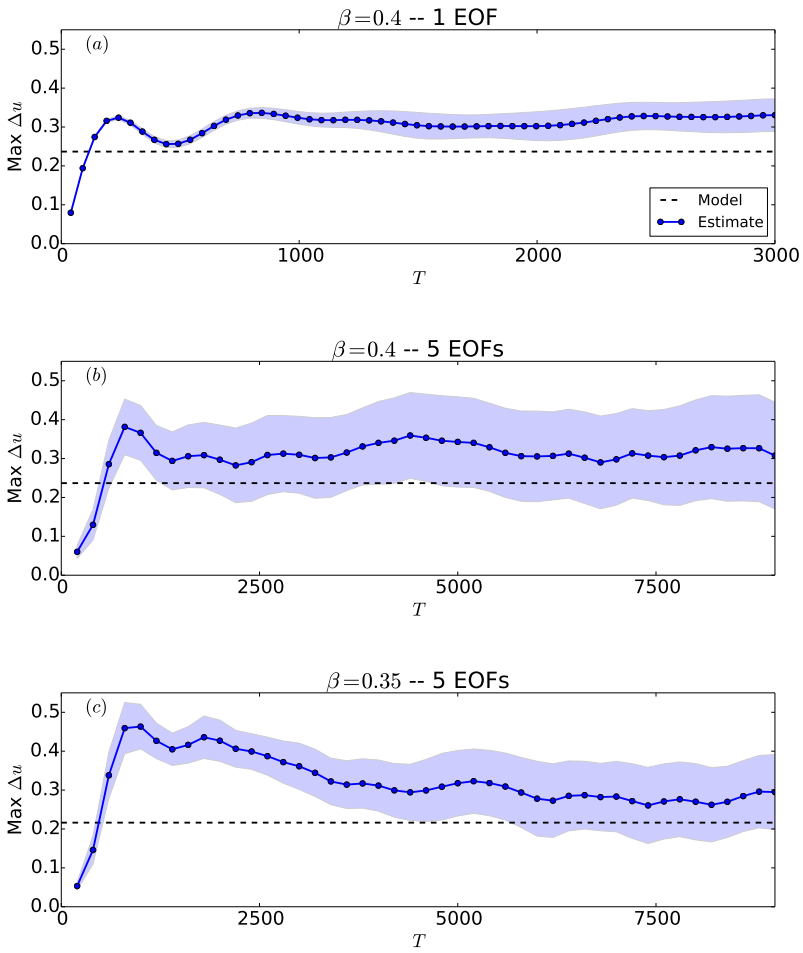


Figure 6.11: *(a)* FDT estimate of the value of $max\Delta u$ in the upper layer using the leading coupled EOF for the case $\beta = 0.4$ as a function of the upper integration limit, T. The blue dots show the ensemble-mean while the shading is plus/minus one standard deviation. The horizontal dashed line shows the value of $max\Delta u$ for the model response. *(b)* is the same but using the first five anti-symmetric coupled EOFs in the FDT calculations and *(c)* shows this for the $\beta = 0.35$ case also using five EOFs.

the principal components had approximately decayed to zero in all cases at this lag (Figure 6.5). The FDT overestimated the model's response and failed to capture the response in the wings, however the estimates were still reasonable, particularly in the $\beta = 0.3$ case, which had a very small root-mean-square (RMS) error (see panels *(b)*

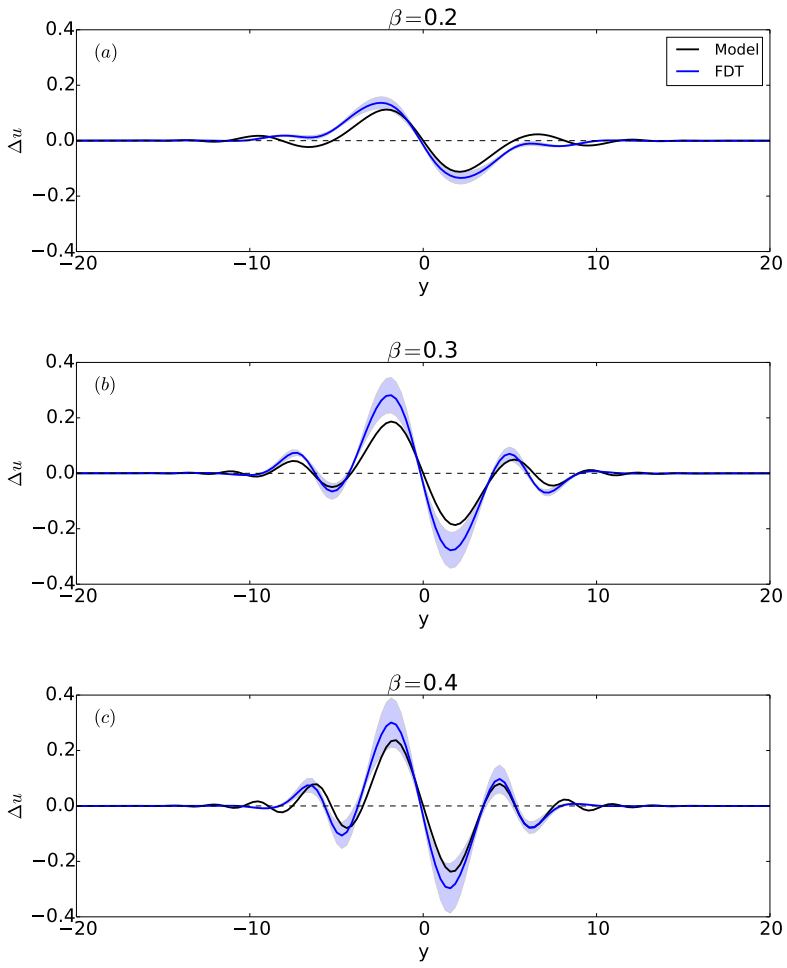


Figure 6.12: As in Figure 6.9 but the FDT estimates used the first five antisymmetric coupled EOFs.

and *(d)* of Figure 6.7). The FDT was also able to at least approximate the difference in magnitudes between the responses of the two layers (Figure 6.7).

Although a single EOF cannot be expected to capture the full structure of the response, an interesting question is whether it can capture how the strength of the response varies with β. To test this I examined how the estimates of $max\Delta u$ varied as β was increased (Figure 6.7). As was mentioned previously, there is a near linear relationship in both layers between $max\Delta u$ and β, with a least-squares fit to the data giving a linear slope of 0.61 in the upper layer and 0.25 in the lower layer. Repeating

this calculation for the FDT estimates, slopes of 0.49 and 0.11 were obtained. These differ significantly from the true slopes but, given that the slopes are of the right sign and magnitude, the FDT using only the dominant EOF can be said to capture the qualitative changes in the linear response as supercriticality is varied.

To first order then, the FDT did a reasonable job of estimating the model's response with just the leading EOFs. To ensure that these estimates were robust to the choice of the upper limit of integration, T was varied from 40 to 3000 model days in each case. From Figure 6.5 one would expect the $\beta = 0.4$ case to be the most sensitive to T and so I show how the FDT estimate of $max\Delta u$ in the upper layer was affected by changing T in this set-up in panel *(a)* of Figure 6.11 (the results in the lower layer and for other values of β were similar). The estimate was relatively stable for T greater than 1000 days, though there was some oscillatory behavior due to the structure at long lags. It is possible that better estimates could have been obtained in each case by choosing T more carefully but I was not seeking to tune the calculations in this way and so felt comfortable using an upper limit of 2000 model days. Note that this is much longer than previous FDT studies, which have used values of T closer to 30 Earth days (150 model days) and is necessary because of the unrealistically long decorrelation times in the model.

5 EOFs

The results of the previous section are promising, however based on section 6.4.1 five EOFs were expected to produce the best estimates. Hence I repeated the calculations of the previous section with the first five EOFs, the results of which are shown for the upper layer in Figure 6.12. A significantly better fit was now obtained, particularly in the wings, and though the FDT continued to overestimate the magnitude of the response, this overestimation was generally less than when only the leading EOFs were included. Panels *(b)* and *(d)* of Figure 6.7 quantify this by comparing the RMS

error of the estimates using the leading EOF only and using the first five EOFs. In general using five EOFs produced lower RMS errors, except for the $\beta = 0.3$ and $\beta = 0.35$ cases when the estimates using five EOFs overestimated the magnitude of the response more than the estimates using the leading EOF. However even in these cases using five EOFs resulted in much better estimates of the wings of the responses. The cause of the overestimation is unclear but may have something to do with the non-Gaussian behavior mentioned in section 6.3. For instance, the overestimation and the sampling error generally increase with β (Figure 6.12), similar to how the data becomes less Gaussian.

As another way of presenting these results, in the left panels of Figure 6.13 the upper layer no-eddy response has been subtracted from every curve in panels *(a)*, *(c)* and *(e)* of Figure 6.12, leaving the "eddy-only" response (the lower layer results are similar). The ability of the FDT to capture the effects of the eddies on the response is clearly quite good as the FDT was able to produce accurate estimates for the shape of the eddy-only response, though once again the response in the center of the domain was overestimated, particularly for larger values of β. Similarly, the right panels show the model response of the upper layer potential vorticity flux and the corresponding FDT estimates (the potential vorticity flux response can be calculated directly from the estimates of the zonal-mean zonal wind response). These calculations show that the FDT is qualitatively capturing how the eddies vary with β.

The a priori calculations suggested that five EOFs would be required to produce the best estimates but to check this I varied the number of EOFs included in the calculations from one to 15. When fewer than five EOFs were used the results were not as accurate (sometimes the FDT estimates even had the wrong sign), suggesting that too few degrees of freedom were included, whereas when six or more EOFs were included the results varied widely because of the sampling error. In line with the expectations then, five EOFs consistently produced the best FDT estimates in terms

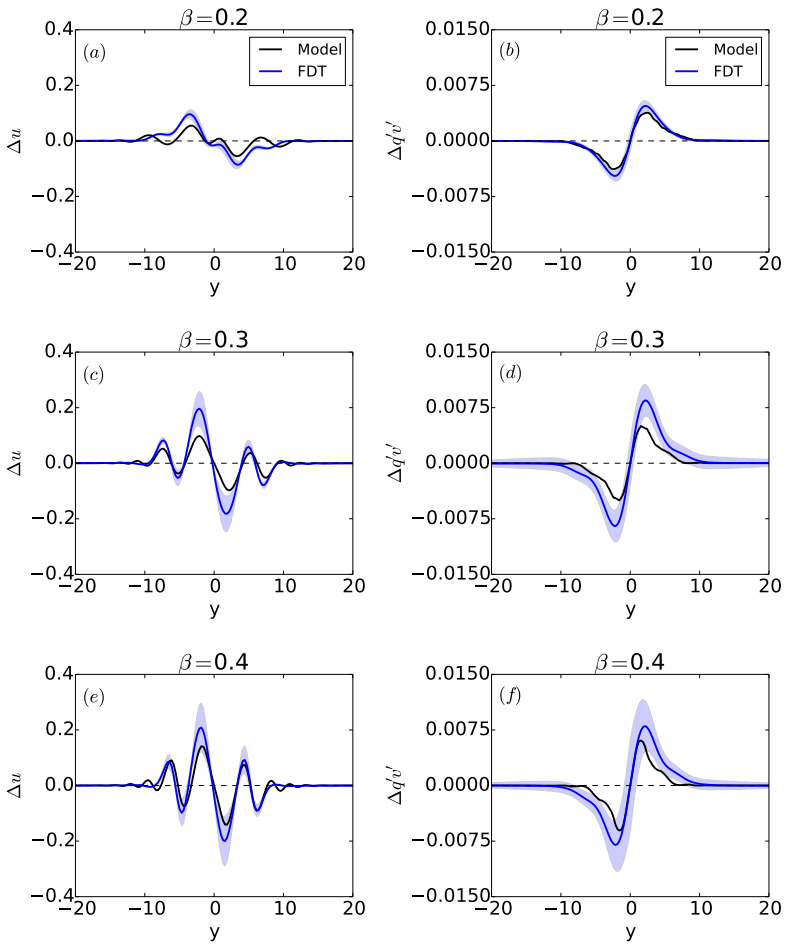


Figure 6.13: *(a)*, *(c)*, *(e)* as in Figure 6.12 but the no-eddy response has been subtracted from every curve. *(b)*, *(d)*, *(f)* The model response of the upper layer potential vorticity flux in black and the corresponding FDT estimates in blue.

of the shapes and amplitudes of the responses. However, using five EOFs did not improve the estimate of the slope of $max\Delta u$ versus β, giving slopes of 0.87 and 0.36 for the upper and lower layers, respectively (Figure 6.7, note the larger sampling errors). These results also point to the importance of only keeping the well-resolved EOFs. Choosing to retain 90% of the variance would have produced worse estimates and similarly if 99% of the variance had been retained, yet a priori there was no way of knowing that retaining 95% would work better than either of these.

To obtain these estimates a value of 2000 model days was again used for T in all cases except when β was set to 0.35. In this case it was found that the estimates took much longer to converge (see panel *(c)* of Figure 6.11) and so the FDT estimate for $\beta = 0.35$ case shown here was obtained using 5000 model days for T; in the other cases I continued using 2000 model days in order to limit the sampling error. It is unclear why this case took so much longer to converge as in the other cases the estimates had essentially converged after roughly 1500 model days (e.g. panel *(b)* of Figure 6.11), though it is noticeable that the FDT estimate for the $\beta = 0.35$ case overshot significantly at short lags.

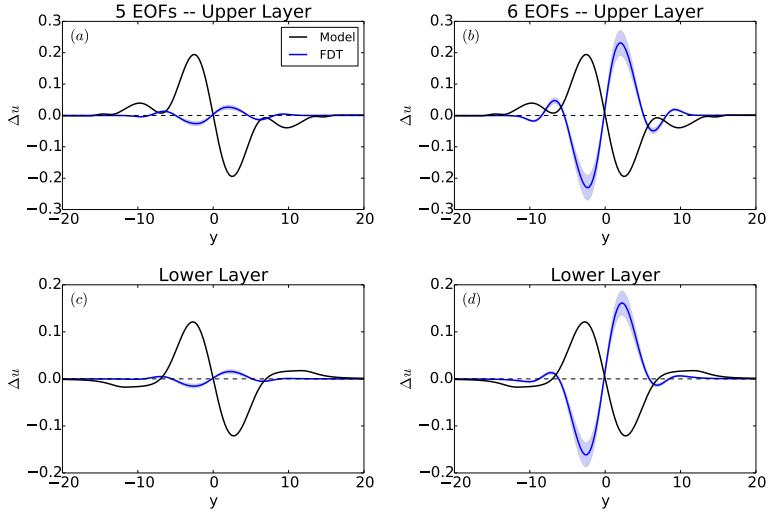


Figure 6.14: Ensemble-mean FDT estimates for the model's response to the baroclinic perturbation in the case $\beta = 0.2$. *(a)*, *(c)* The results using the first five coupled anti-symmetric EOFs. *(b)*, *(d)* The results using the first six coupled anti-symmetric EOFs. The color scheme is the same as in Figure 6.8 and the top panels show the upper layer while the lower panels show the lower layer.

6.4.3 Baroclinic Perturbation

The discussion in section 6.4.1 showed that the FDT was unlikely to produce a good estimate for the model's response to the baroclinic perturbation using this basis as the perturbation does not project onto the well resolved EOFs. For instance, the left

two panels of Figure 6.15 show that when five EOFs were used in the $\beta = 0.2$ case the FDT estimate substantially underestimated the response and the estimate was also of the wrong sign. The right panels then show that when six EOFs were used the FDT estimate had approximately the right magnitude but again had the wrong sign. The FDT performed just as poorly for other values of β.

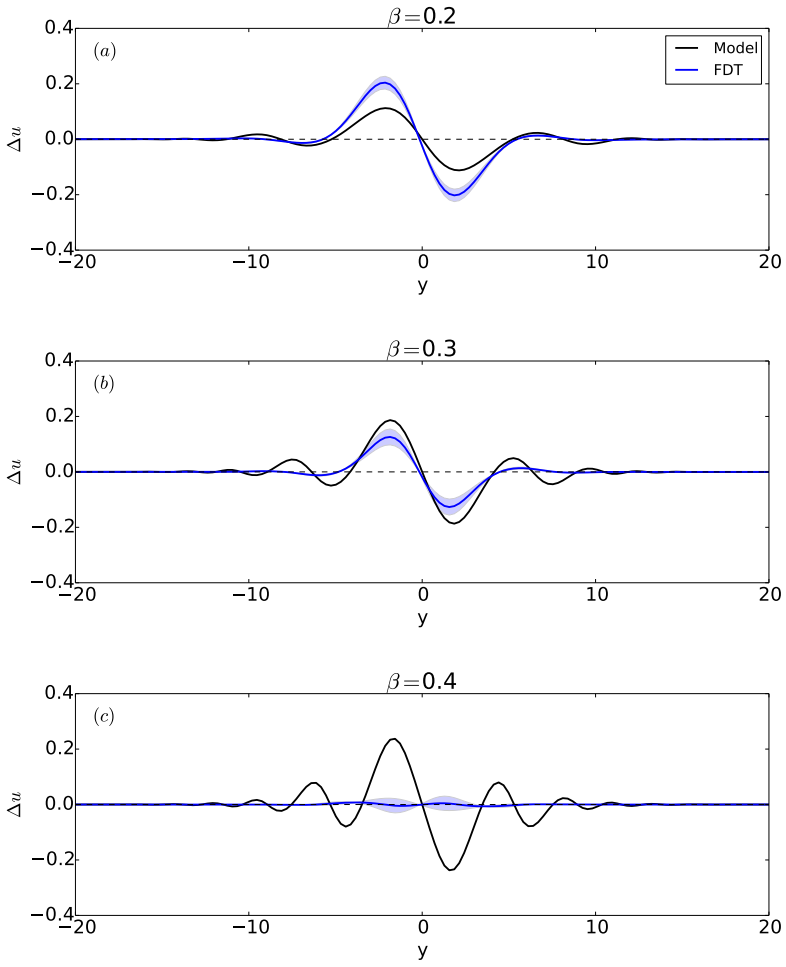


Figure 6.15: Ensemble-mean FDT estimates for the upper layer model responses to the barotropic perturbation using the leading barotropic and baroclinic EOFs for three values of β. The color scheme is the same as in Figure 6.8.

In order to get around the problem of capturing the perturbation while ensuring that the EOFs were well sampled I repeated these calculations using two alternative bases. The first basis was constructed by separating the data into their barotropic

and baroclinic components and then calculating a new set of EOFs. The barotropic variability is less dominant than the equivalent barotropic variability and so might not be as well sampled, but conversely the purely baroclinic variability might be easier to resolve than the equivalent baroclinic variability. Indeed, using the symmetry/asymmetry of the EOFs as a measure of the sampling errors, the baroclinic EOFs were better sampled. Only the leading barotropic and baroclinic EOFs were included in the FDT calculations (calculations in which more EOFs were included produced worse estimates), however this was enough to ensure that both sets of perturbations and responses projected strongly onto the EOFs.

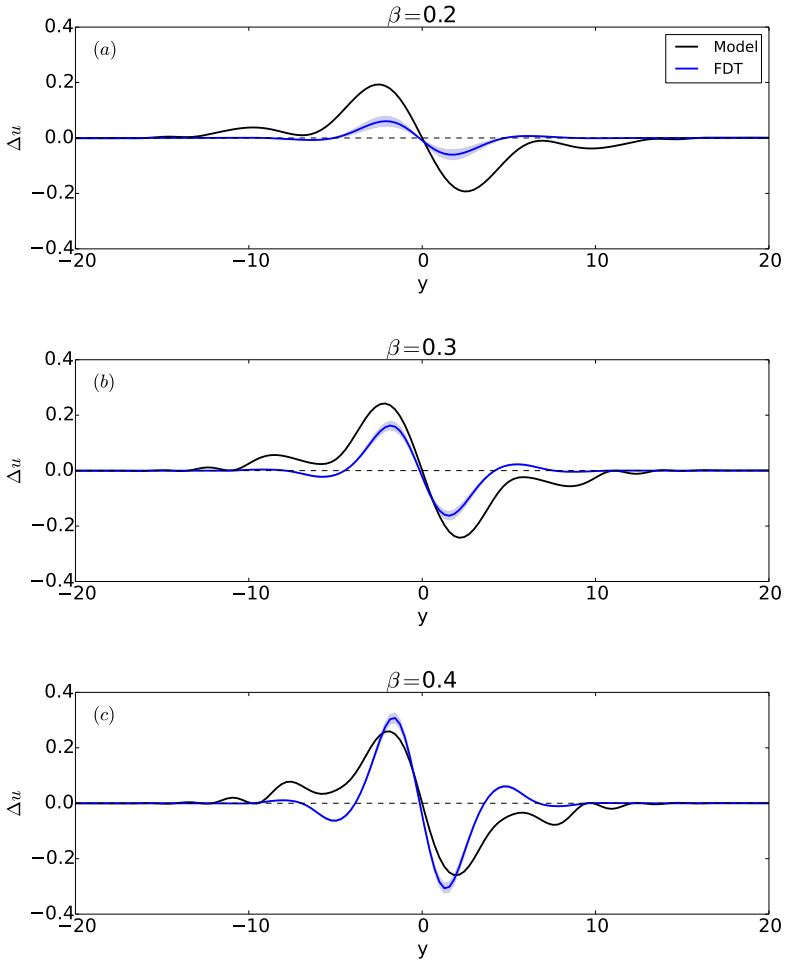


Figure 6.16: As in Figure 6.15 but for the baroclinic perturbation.

In the barotropic case these new EOFs performed worse than the coupled EOFs, as the resulting FDT estimates predicted that the model's response would decrease in strength with β. Nevertheless, the estimates were still reasonable in all cases apart from when $\beta = 0.4$ (see Figure 6.15). On the other hand, much better estimates for the baroclinic perturbation were obtained (Figure 6.16; the agreement for the lower layer was similar) and the FDT now correctly predicted that the response would increase with β, though the slope was significantly overestimated: the response when $\beta = 0.2$ was substantially underestimated while the response when $\beta = 0.4$ was slightly overestimated. In all cases an upper limit of 2000 model days was again used and the estimates were checked to ensure that they were robust to the choice of T.

The FDT can thus produce reasonable estimates for the baroclinic case following the procedure from before but dividing up the data in such a way as to improve the sampling. Hence the sampling is the issue, not a more fundamental failure of the formalism due, in particular, to non-Gaussianity.

A second alternative basis was generated for each perturbation by first subtracting the variability associated with the forcing vector from the data and calculating EOFs for the remaining variability. These EOFs were then combined with the forcing vector to produce the new basis. New bases thus had to be tailored to each perturbation and could not be reused for other perturbations to the forcing. Also, the different forcing vectors were not independent of the EOFs and so the $\mathbf{C}(0)$ matrices were no longer diagonal. On the other hand, this choice of basis still does not assume anything about the form of the response.

Once these bases were generated only the well-separated EOFs were retained – in addition to the forcing vector – in order to reduce the sampling errors (only the leading EOF was well separated). This approach was very sensitive to the length of the dataset, so using the whole time series produced better, and more robust, estimates than taking the average of the ensemble members. However, once the estimates had

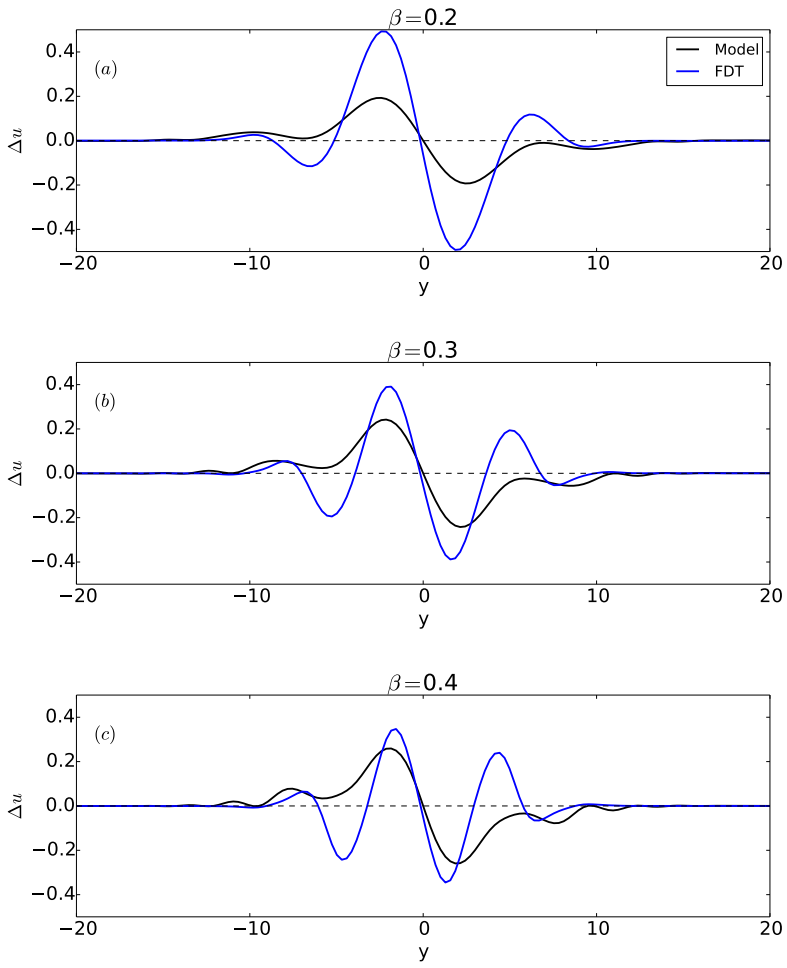


Figure 6.17: As in Figure 6.16 but the FDT estimates use a new basis with the leading EOF having the form of the baroclinic perturbation and are calculated using the whole time-series rather than an ensemble (hence there are no estimates of the sampling error). The lower layer results are similar.

converged they were quite accurate. The barotropic estimates were very similar to those using the coupled EOFs, while the baroclinic estimates captured the leading order behavior for every case except when $\beta = 0.2$ (Figure 6.17).

6.5 Conclusions

In this work I have used the FDT to estimate the response of a baroclinically unstable jet in a two-layer QG model on a β-plane in a periodic channel. The control climate that is perturbed is symmetric about the center of the channel. I consider two perturbations, both of which produce zonal wind responses that are anti-symmetric about the center of the channel, and are therefore annular mode-like, but differ in the vertical structure of the forcing. For the barotropic perturbation the FDT gives robust and accurate estimates for a range of values of β using the first five anti-symmetric, coupled EOFs, though it consistently overestimates the response, perhaps due to significant departures from Gaussianity in the data. Recently, Hassanzadeh and Kuang (2016) have suggested that non-normality may also limit the ability of the FDT to make quantitatively accurate predictions in many climate settings [37]. Five EOFs is exactly how many EOFs are well-separated according to the criterion of [82], suggesting that this is a useful method of deciding how many EOFs to retain, though more rigorous testing would be required to verify that this is a general result. Reasonable estimates are also obtained using just the leading EOF in each case and the FDT was able to qualitatively predict how the amplitude of the response increases with β. This adds to the evidence that the annular-mode time scale plays an important role in determining the response of the midlatitudes to small perturbations, though it should be noted that the results are still more qualitatively accurate than quantitative and it is not clear that inaccuracies in [97] are a result of their use of a POP-based formalism.

Conversely, the baroclinic perturbation is more challenging for the FDT. The perturbation to the forcing projects too weakly onto the well resolved EOFs for these to produce accurate estimates but adding the poorly resolved EOFs that the forcing does project onto results in large errors. To get around this problem I have devised two new strategies for performing the FDT calculations. In the first, the

data were divided into their barotropic and baroclinic components and new EOFs were calculated. This alternative basis better resolves the baroclinic variability and so can handle the baroclinic perturbation. The second method uses EOFs tailored to each forcing perturbation. This approach produced accurate estimates for both barotropic and baroclinic forcing perturbations, but is more sensitive to the length of the time-series.

Taken as a whole, these results show the importance of sampling when applying the FDT to climate systems. On the one hand, adding poorly resolved EOFs reduces the accuracy of FDT estimates, but the perturbation and the response must both be captured by the well resolved EOFs in order to obtain accurate estimates. This is similar to the findings of [30], who obtained better FDT estimates for the response of an intermediate-complexity GCM to realistic perturbations than to idealized "hot-spot" perturbations.

The strategy of using the perturbation to the forcing as the leading EOF might provide a way around some of these difficulties. This approach is different from that used in previous studies in that it requires calculating a new basis for every forcing perturbation, but still does not require knowledge of the model's response. Hence, future FDT studies might consider a hybrid strategy in which a conventional basis is used for forcing perturbations which project strongly onto the leading modes of variability, while more specialized bases are used for perturbations which are poorly captured by the conventional EOFs. As a topical example, it may be possible to use a carefully constructed basis to produce FDT estimates for the response in more complex models of the mid-latitudes to high latitude stratospheric cooling.

Finally, although the results have investigated the importance of resolution, there are still several other outstanding issues with using the FDT for climate purposes. For instance, I have suggested that the overestimates of the magnitude of the response are correlated with non-Gaussian behavior in the model, but I have been unable to

show quantitatively how departures from Gaussianity bias FDT estimates. Another question is how the importance of resolution varies as the size of the system increases. The system considered here has relatively few active degrees of freedom because of its zonal symmetry and because of the symmetry of the control climate about the center of the channel, and I work with five to six EOFs. In contrast, in the study of [35] the linear operator involved 1800 three-dimensional EOFs. For such a large system it is possible that even if a few EOFs were poorly sampled, these would constitute a much smaller fraction of the total number of included degrees of freedom and so their inclusion would not affect the FDT estimates as significantly as including a single additional EOF can here. In any case, although progress is still needed before the FDT is ready to quantitatively address larger questions such as estimating climate responses from observations, it has been shown here that it can in some cases reproduce the response of a two-layer model to small perturbations in forcing with considerable accuracy. A linear, perturbative theory can thus be substituted for the eddy flux theories otherwise needed to predict these responses.

Chapter 7

Conclusion

7.1 Summary

This thesis has investigated the role of eddy momentum fluxes (EMFs) in several different problems of atmospheric dynamics. The first half of the thesis, comprising three chapters, considered the influence of stationary waves on the momentum budget of a dry general circulation model (GCM). Chapters 2 and 3 studied the response of the GCM to idealized, Gaussian orography. For mountain heights less than 1km the GCM's response was found to be in a linear regime, with the amplitude of the response proportional to the height of the mountain. This response consisted of a meridionally-trapped, wavenumber five "circumglobal" wave [9] that propagates along the waveguide formed by the midlatitude jet. For larger mountain heights the response transitions to a non-linear regime that is dominated by a lower wavenumber wave that mostly propagates meridionally into the tropics. A barotropic model on a sphere is able to reproduce this transition, though the reasons for the breakdown of the linear regime appear to be different in the two models. It was hypothesized that the transition in the GCM is caused by the stationary wave eroding the waveguide, eventually allowing for increased meridional propagation when the wave is no

longer trapped by the jet, however I have been unable to definitely verify that this is responsible for the transition.

The non-acceleration theorem says that in an inviscid, adiabatic quasi-geostrophic (QG) system the stationary EMF convergence will exactly balance the torque; however analysis of the GCM's momentum budget reveals that in the linear regime the stationary EMF convergence is shifted polewards of the torque, and is also slightly larger (Chapter 3). Experiments with a stationary wave model indicate that the displacement is caused in part by a stationary non-linearity due to the air flowing around the orography, in addition to flowing up and over the orography. Interactions with transient eddies also push the stationary EMF convergence polewards in the GCM. The increased meridional propagation of the stationary wave in the non-linear regime results in the stationary EMF convergence becoming much larger than the torque for these mountains; this is compensated for by the responses of the friction and of the transient EMF convergence.

For mountain heights less than 3km there is increased transient EMF convergence polewards of the jet and reduced transient EMF convergence equatorwards of the jet, while the friction is increased polewards of the jet and decreased equatorwards of the jet. These responses reflect a poleward shift of the midlatitude jet. The patterns are reversed for mountain heights $\geq$3km, as the jet shifts equatorward. A tentative explanation for this transition was made based on a competition between the stationary EMFs, which tend to push the jet polewards, and the transient EMFs, which tend to push the jet equatorwards. For smaller mountains the stationary EMFs succeed in pushing the jet shifts polewards, while for larger mountains the transient EMFs dominate and the jet shifts equatorwards.

Chapter 4 turned to the question of equatorial heating. For small heating rates ($<$0.5K/day) the GCM's response corresponds to the response of the linear Matsuno-Gill model. This linear response breaks down for larger heating rates because the

heating stabilized the tropical troposphere, and a large-scale Rossby wave dominates the response. At the same time, the equatorial winds increasingly superrotate. This superrotation is driven by the stationary EMFs due to the stationary wave response to the heating, and is damped by the vertical advection of low momentum air by the Hadley circulation and also by the transient EMFs. These increasingly diverge momentum from the equator as the tropical winds accelerate because baroclinic eddies originating in mid-latitudes are able to propagate deeper into the tropics, where they break and decelerate the flow. It was also found that the GCM can be made to strongly superrotate by reducing the equator-to-pole temperature gradient and applying a large heating.

The second half of the thesis focused on the relationship between transient EMFs and mid-latitude jets. Chapter 5 investigated the lower tropospheric EMFs in a two-layer QG model, in the GCM and in a reanalysis dataset. The structure of the lower tropospheric EMFs are very similar in the two models and in the reanalysis dataset, as the transient EMFs converge momentum into the jet at phase speeds close to the lower tropospheric jet speed and diverge momentum out of the jet at slower phase speeds. On the flanks of the jet there is EMF divergence at fast phase speeds and EMF convergence at slow phase speeds. The similarities across the models and the reanalysis dataset suggest that the dynamics of the QG model can be used to interpret the behavior of the lower tropospheric eddies. In this context, a conceptual picture of the lower tropospheric eddies was suggested, based on the premise that the weak, negative PV gradient in the lower troposphere means that eddies localized there cannot propagate significant distances. Instead, the wide baroclinic disturbance that is responsible for the eddies excites lower tropospheric eddies near their critical latitudes, where they break and accelerate the flow. In the center of the jet there is less breaking and so there is compensating deceleration. The EMF convergence at faster phase speeds is due to equivalent barotropic eddies, which mostly propagate

on the (positive) upper tropospheric potential vorticity gradient and so accelerate the flow in the center of the jet, where they form, and decelerate the flow on the flanks of the jet, where they break.

Finally, in Chapter 6 the Fluctuation-Dissipation Theorem (FDT) was used to predict the response of the QG model to two perturbations: a barotropic perturbation, with the same sign in each layer, and a baroclinic perturbation, with the opposite sign in each layer. The power of the FDT is that it allows the response of a system to an external forcing to be predicted based on the internal variability of the unperturbed system. The FDT was able to produce qualitatively accurate predictions for the barotropic perturbation, and these predictions were shown to be robust to the choices made in the FDT calculations, however the FDT struggled to produce even qualitatively accurate predictions for the baroclinic perturbation. This is because the baroclinic variability is hard to estimate accurately in the QG model, whose internal variability is dominated by equivalent barotropic eddies. Several strategies were investigated for better estimating the baroclinic variability, which could be relevant for future FDT studies using more comprehensive atmospheric models.

7.2 Discussion

In addition to the results from the individual projects, a larger theme of this thesis has been an attempt to connect linear theory to the non-linear behavior of fully turbulent atmospheres. In Chapters 2, 3 and 4 the relevance of linear stationary wave theory for the GCM was evaluated, and the breakdown of linearity was investigated. In Chapter 5 the interpretation of the lower tropospheric EMFs was based on a linear picture in which the characteristics of the non-linear stirring are taken as given and in Chapter 6 the FDT was used to estimate a linear operator for the QG model.

Linear theory often provides a starting point for understanding the behavior of non-linear systems, and many outstanding problems in atmospheric dynamics involve incorporating non-linear effects into linear theory. One method for studying non-linear effects is the use of a "hierarchy" of models [46], in which the linear system is connected to more realistic atmospheres via a series of intermediate models. By gradually introducing increased complexity, a model hierarchy allows non-linear effects to be isolated and studied systematically. Several of the projects in this thesis have used such a hierarchy, with a linear system or a conceptual model based on linear thinking at the base: the barotropic index of refraction (Chapter 2), the non-acceleration theorem (Chapter 3), the Matsuno-Gill model (Chapter 4) and the linear theory of wave-mean flow interactions (Chapter 5).

At the same time, new questions arise as complexity is added, and it can be difficult, or even impossible, to provide more than heuristic answers for these questions. The transition to meridional propagation in Chapter 2 remains somewhat poorly understood: although the stationary wave seems to erode the waveguide downstream of the mountain, I have been unable to show conclusively that this is responsible for the transition. In Chapter 3 a tentative explanation for the transition from a poleward jet shift to an equatorward jet shift was offered, but confirming this hypothesis will require analyzing the wave-breaking characteristics of the transient eddies as well as performing life-cycle calculations. Similarly, I have been unable to test the conceptual picture for the lower tropospheric EMFs described in Chapter 5, as the time-mean transient EMFs are a small residual of fluxes that vary over a large range of values at any instant in time. Furthermore, this interpretation suggests that the lower tropospheric EMFs are largely determined by the highly non-linear stirring that excites the eddies and so a complete theory for the lower tropospheric EMFs requires a theory for this stirring. Finally, even the best results in Chapter 6 are qualitatively accurate, rather than quantitative. It was shown that one reason for this is that the dynamics

of the QG model have significant deviations from Gaussianity, whereas the formulation of the FDT that was used in Chapter 6 assumes that the system is Gaussian; but there are other possible reasons for the lack of quantitative agreement [37].

Tools are available to answer some of these questions, such as stochastic closures and baroclinic lifecycle calculations; however, even with these it is likely that we will not be able to resolve all of these issues. This reflects the fact that the troposphere is a highly non-linear, turbulent system; which is exactly the type of system that modern science struggles most to investigate quantitatively. This limits our ability to understand the present-day climatology of the general circulation and also our ability to accurately predict how the circulation will change in the future [111]. Instead, we may have to content ourselves with qualitative explanations, careful analysis of numerical simulations, quantitative comparisons with observed circulation trends and systematic analysis of uncertainties and biases.

Appendix A

Cooper-Haynes Algorithm

To integrate the lag-covariance matrices for the FDT calculations in chapter 6 I have used an algorithm proposed by Cooper and Haynes in an unpublished manuscript. First note that I am integrating

$$\int_0^\infty C(\tau)d\tau \approx \int_0^T C(\tau)d\tau. \tag{A.1}$$

For a particular lag τ the entry in $C(\tau)$ for two elements, a and b, of the model state vector, X, is

$$C(\tau)_{ab} = \frac{1}{n-q-1}\sum_{p=1}^{n-q} x_p y_{q+p} \tag{A.2}$$

where n is the total length of the time-series, q is the number of datapoints representing a lag t and

$$x_a = X_a(t) - \bar{X}_a,$$
$$y_b = X_b(t) - \bar{X}_b.$$

Now taking r to be the number of datapoints representing a lag of T the trapezoid rule can be used to write the integral as

$$\int_0^\infty C(\tau)d\tau \approx \frac{\Delta\tau}{2(n-1)}\sum_{p=1}^{n} x_p y_p + \sum_{q=1}^{r}\frac{\Delta\tau}{n-q-1}\sum_{p=1}^{n-q} x_p y_{q+p}, \tag{A.3}$$

where $\Delta\tau$ is the spacing in time of the datapoints. The last term on the right hand side can be approximated as (for $r << n$):

$$\begin{aligned}\sum_{q=1}^{r}\frac{\Delta\tau}{n-q-1}\sum_{p=1}^{n-q} x_p y_{q+p} &\approx \frac{\Delta\tau}{n-r-1}\sum_{q=1}^{r}\sum_{p=1}^{n-q} x_p y_{q+p}, \\ &= \frac{\Delta\tau}{n-r-1}\sum_{p=1}^{n-q} x_p(\sum_{q=1}^{r} y_{q+p}).\end{aligned} \tag{A.4}$$

The sum in brackets can then be updated from the $p-1$th operation using just one subtraction and one addition operation. The algorithm thus takes of the order n operations, so that the whole matrix $C(\tau)$ can be integrated using d^2n operations where d is the spatial dimension of the dataset.

Bibliography

[1] R V Abramov and A J Majda. A New Algorithm for Low-Frequency Climate Response. *Journal of the Atmospheric Sciences*, 66(2):286–309, 2009.

[2] A F Adames and D Kim. The mjo as a convectively coupled moisture wave: theory and observations. *Journal of the Atmospheric Sciences*, 73(21):913–941, 2016.

[3] F Ait-Chaalal and T Schneider. Why eddy momentum fluxes are concentrated in the upper troposphere. *Journal of the Atmospheric Sciences*, 72(4):1585–1604, 2015.

[4] N P Arnold, E Tziperman, and B Farrell. Abrupt transition to strong superrotation driven by equatorial wave resonance in an idealized gcm. *Journal of the Atmospheric Sciences*, 69:626–640, 2010.

[5] T L Bell. Climate Sensitivity from Fluctuation–Dissipation: Simple model Tests. *Journal of the Atmospheric Sciences*, 37(8):1700–1707, 1980.

[6] J A Biello, A J Majda, and M W Moncrieff. Meridional momentum flux and superrotation in the multi-scale ipesd mjo model. *Journal of the Atmospheric Sciences*, 64(5):1636–1651, 2007.

[7] Jenny Brandefelt and Heiner Kornich. Northern hemisphere stationary waves in future climate projections. *Journal of Climate*, 21(23):6341–6353, 2008.

[8] Grant Branstator. Horizontal energy propagation in a barotropic atmosphere with meridional and zonal structure. *Journal of the Atmospheric Sciences*, 40(7):1689–1708, 1983.

[9] Grant Branstator. Circumglobal teleconnections, the jet stream waveguide, and the north atlantic oscillation. *Journal of Climate*, 15(14):1893–1910, 2002.

[10] Grant Branstator and Frank Selten. 'modes of variability' and climate change. *Journal of Climate*, 22(10):2639–2658, 2009.

[11] D J Brayshaw, B Hoskins, and M Blackburn. The basic ingredients of the north atlantic storm track. part i: Landsea contrast and orography. *Journal of the Atmospheric Sciences*, 66(14):2539–2558, 2009.

[12] A H Butler, D W J Thompson, and R Heikes. The Steady-State Atmospheric Circulation Response to Climate Changelike Thermal Forcings in a Simple General Circulation Model. *Journal of Climate*, 23(13):3474–3474, 2010.

[13] Rodrigo Caballero and Matthew Huber. Spontaneous transition to superrotation in warm climates simulated by cam3. *Geophysical Research Letters*, 37(11), 2010. L11701.

[14] Henrik Carlson and Rodrigo Caballero. Enhanced mjo and transition to superrotation in warm climates. *Journal of Advances in Modeling Earth Systems*, 8(1):304–318, 2016.

[15] P Ceppi and D L Hartmann. On the speed of the eddy-driven jet and the width of the hadley cell in the southern hemisphere. *Journal of Climate*, 26:3450–3465, 2012.

[16] J Chai, M Jansen, and G K Vallis. Equilibration of a baroclinic planetary atmosphere toward the limit of vanishing bottom friction. *Journal of the Atmospheric Sciences*, 2016.

[17] E K M Chang. Diabatic and orographic forcing of northern winter stationary waves and storm tracks. *Journal of Climate*, 22(14):670–688, 2009.

[18] J. G. Charney and A. Eliassen. A numerical method for predicting the perturbations of the middle latitude westerlies. *Tellus*, 1(2):38–54, 1949.

[19] Jule G. Charney and John G. DeVore. Multiple flow equilibria in the atmosphere and blocking. *Journal of the Atmospheric Sciences*, 36(7):1205–1216, 1979.

[20] Kerry H. Cook and Isaac M. Held. The stationary response to large-scale orography in a general circulation model and a linear model. *Journal of the Atmospheric Sciences*, 49(6):525–539, 1992.

[21] F C Cooper and P H Haynes. Climate Sensitivity via a Nonparametric Fluctuation–Dissipation Theorem. *Journal of the Atmospheric Sciences*, 68(5):937–953, 2011.

[22] Michael K. Davey. A quasi-linear theory for rotating flow over topography. part 1. steady b-plane channel. *Journal of Fluid Mechanics*, 99(2):267–292, 1980.

[23] D. P. Dee, S. M. Uppala, A. J. Simmons, P. Berrisford, P. Poli, S. Kobayashi, U. Andrae, M. A. Balmaseda, G. Balsamo, P. Bauer, P. Bechtold, A. C. M. Beljaars, L. van de Berg, J. Bidlot, N. Bormann, C. Delsol, R. Dragani, M. Fuentes, A. J. Geer, L. Haimberger, S. B. Healy, H. Hersbach, E. V. Hlm, L. Isaksen, P. Kllberg, M. Khler, M. Matricardi, A. P. McNally, B. M. Monge-Sanz, J.-J. Morcrette, B.-K. Park, C. Peubey, P. de Rosnay, C. Tavolato, J.-N. Thpaut, and F. Vitart. The era-interim reanalysis: configuration and performance of the data assimilation system. *Quarterly Journal of the Royal Meteorological Society*, 137(656):553–597, 2011.

[24] T DelSole. Can Quasigeostrophic Turbulence Be Modeled Stochastically? *Journal of the Atmospheric Sciences*, 53(11):1617–1633, 1996.

[25] T DelSole. A simple model for transient eddy momentum fluxes in the upper troposphere. *Journal of the Atmospheric Sciences*, 58:3019–3035, 2001.

[26] Jacques Derome and A. Wiin-Nielsen. The response of a middle-latitude model atmosphere to forcing by topography and stationary heat sources1,,2. *Monthly Weather Review*, 99(7):564–576, 1971.

[27] J. Egger. Dynamics of blocking highs. *Journal of the Atmospheric Sciences*, 35(10):1788–1801, 1978.

[28] J. Gavin Esler, Lorenzo M. Polvani, and R. Alan Plumb. The effect of a hadley circulation on the propagation and reflection of planetary waves in a simple one-layer model. *Journal of the Atmospheric Sciences*, 57(10):1536–1556, 2000.

[29] B F Farrell and P J Ioannou. Stochastic dynamics of the midlatitude atmospheric jet. *Journal of the Atmospheric Sciences*, 52:1642–1656, 1995.

[30] D Fuchs, S Sherwood, and D Hernandez. An Exploration of Multivariate Fluctuation Dissipation Operators and Their Response to Sea Surface Temperature Perturbations. *Journal of the Atmospheric Sciences*, Accepted.

[31] E P Gerber and L M Polvani. Stratosphere-troposphere coupling in a relatively simple agcm: The importance of stratospheric variability. *Journal of Climate*, 22:1920–1933, 2009.

[32] E P Gerber and G K Vallis. Eddy-zonal flow interactions and the persistence of the zonal index. *Journal of the Atmospheric Sciences*, 64:3296–3311, 2007.

[33] E P Gerber, S Voronin, and L M Polvani. Testing the Annular Mode Autocorrelation Time Scale in Simple Atmospheric General Circulation Models. *Monthly Weather Review*, 136(4):1523–1535, 2008.

[34] A E Gill. Some simple solutions for heat-induced tropical circulation. *Quarterly Journal of the Royal Meteorological Society*, 106:447–462, 1980.

[35] Andrey Gritsun and Grant Branstator. Climate Response Using a Three-Dimensional Operator Based on the Fluctuation–Dissipation Theorem. *Journal of the Atmospheric Sciences*, 64(7):2558–2575, 2007.

[36] William L. Grose and Brian J. Hoskins. On the influence of orography on large-scale atmospheric flow. *Journal of the Atmospheric Sciences*, 36(2):223–234, 1979.

[37] P Hassanzadeh and Z Kuang. The linear response function of an idealized atmosphere. part ii: Implications for the practical use of the fluctuationdissipation theorem and the role of operators nonnormality. *Journal of the Atmospheric Sciences*, 73(9):3441–3452, 2016.

[38] Y Hayashi. A generalized method of resolving disturbances into progressive and retrogressive waves by space fourier and time cross-spectral analyses. *Journal of the Meteorological Society of Japan*, 49:125–128, 1971.

[39] I M Held. Momentum transport by quasi-geostrophic eddies. *Journal of the Atmospheric Sciences*, 32:1494–1497, 1975.

[40] I M Held. Stationary and quasi-stationary eddies in the extratropical troposphere: theory. In B J Hoskins and R P Pearce, editors, *Large-scale Dynamical Processes in the Atmosphere*. Academic Press, New York, NY, 1983.

[41] I M Held. The macroturbulence of the troposphere. *Tellus A*, 51(1):59–70, 1999.

[42] I M Held. The general circulation of the atmosphere *Woods Hole Lecture Notes*, 2000.

[43] I M Held and I-S Kang. Barotropic models of the extratropical response to el nio. *Journal of the Atmospheric Sciences*, 44(23):3576–3586, 1987.

[44] I M Held and V D Larichev. A scaling theory for horizontally homogeneous, baroclinically unstable flow on a beta plane. *Journal of the Atmospheric Sciences*, 53:946–952, 1996.

[45] I M Held, R L Panetta, and R T Pierrehumbert. Stationary external rossby waves in vertical shear. *Journal of the Atmospheric Sciences*, 42(9):865–883, 1985.

[46] Isaac M Held. The gap between simulation and understanding in climate modeling. *Bulletin of the American Meteorological Society*, 86(11):1609–1614, 2005.

[47] Isaac M. Held and Peter J. Phillips. A barotropic model of the interaction between the hadley cell and a rossby wave. *Journal of the Atmospheric Sciences*, 47(7):856–869, 1990.

[48] Isaac M. Held and Max J. Suarez. A proposal for the intercomparison of the dynamical cores of atmospheric general circulation models. *Bulletin of the American Meteorological Society*, 75(10):1825–1830, 1994.

[49] Isaac M. Held, Mingfang Ting, and Hailan Wang. Northern winter stationary waves: Theory and modeling. *Journal of Climate*, 15(16):2125–2144, 2002.

[50] H H Hendon. The timemean flow and variability in a nonlinear model of the atmosphere with tropical diabatic forcing. *Journal of the Atmospheric Sciences*, 43(23):72–88, 1986.

[51] G Holloway and J Eert. Intransitive multiple equilibria in eddy-active barotropic flows. *Journal of the Atmospheric Sciences*, 44(15):2001–2005, 1987.

[52] B. J. Hoskins, A. J. Simmons, and D. G. Andrews. Energy dispersion in a barotropic atmosphere. *Quarterly Journal of the Royal Meteorological Society*, 103(438):553–567, 1977.

[53] Brian J. Hoskins and Tercio Ambrizzi. Rossby wave propagation on a realistic longitudinally varying flow. *Journal of the Atmospheric Sciences*, 50(12):1661–1671, 1993.

[54] Brian J. Hoskins and David J. Karoly. The steady linear response of a spherical atmosphere to thermal and orographic forcing. *Journal of the Atmospheric Sciences*, 38(6):1179–1196, 1981.

[55] F F Jin and M Ghil. Intraseasonal oscillations in the extratropics: Hopf bifurcation and topographic instabilities. *Journal of the Atmospheric Sciences*, 47(24):3007–3022, 1990.

[56] E Kallen. The nonlinear effects of orographic and momentum forcing in a low-order, barotropic model. *Journal of the Atmospheric Sciences*, 38(10):2150–2163, 1981.

[57] E Kallen. On hysteresis-like effects in orographically forced models. *Tellus A*, 37A(3):249–257, 1985.

[58] S M Kang and L M Polvani. The interannual relationship between the latitude of the eddy-driven jet and the edge of the hadley cell. *Journal of Climate*, 24:563–568, 2011.

[59] Akira Kasahara. The dynamical influence of orography on the large-scale motion of the atmosphere. *Journal of the Atmospheric Sciences*, 23(3):259–271, 1966.

[60] J Kidston, G K Vallis, S M Dean, and J A Renwick. Can the increase in the eddy length scale under global warming cause the poleward shift of the jet streams? *Journal of Climate*, 24:3764–3780, 2010.

[61] Peter D. Killworth and Michael E. McIntyre. Do rossby-wave critical layers absorb, reflect, or over-reflect? *Journal of Fluid Mechanics*, 161:449–492, 1985.

[62] H k Kim and S Lee. The wavezonal mean flow interaction in the southern hemisphere. *Journal of the Atmospheric Sciences*, 61:1055–1067, 2001.

[63] I Kraucunas and D L Hartmann. Equatorial superrotation and the factors controlling the zonal-mean zonal winds in the tropical upper troposphere. *Journal of the Atmospheric Sciences*, 62:371–389, 2005.

[64] A L Laraia and T Schneider. Superrotation in terrestrial atmospheres. *Journal of the Atmospheric Sciences*, 72(7):4281–4296, 2015.

[65] S Lee. Finite-amplitude equilibration of baroclinic waves on a jet. *Journal of the Atmospheric Sciences*, 67:434–451, 2010.

[66] S Lee and I M Held. Baroclinic wave packets in models and observations. *Journal of the Atmospheric Sciences*, 50:1413–1428, 1993.

[67] C E Leith. Climate Response and Fluctuation Dissipation. *Journal of the Atmospheric Sciences*, 32(10):2022–2026, 1975.

[68] Stephanie Leroux, Gilles Bellon, Romain Roehrig, Mihaela Caian, Nicholas P. Klingaman, Jean-Philippe Lafore, Ionela Musat, Catherine Rio, and Sophie Tyteca. Inter-model comparison of subseasonal tropical variability in aqua-planet experiments: Effect of a warm pool. *Journal of Advances in Modeling Earth Systems*, 8(4):1526–1551, 2016.

[69] R S Lindzen and B Farrell. A simple approximate result for the maximum growth rate of baroclinic instabilities. *Journal of the Atmospheric Sciences*, 37(14):1648–1654, 1980.

[70] J Liu and T Schneider. Convective generation of equatorial superrotation in planetary atmospheres. *Journal of the Atmospheric Sciences*, 68(7):2742–2756, 2011.

[71] N J Lutsko and I M Held. The response of an idealized atmosphere to orographic forcing: Zonal versus meridional propagation. *Journal of the Atmospheric Sciences*, 73(9):3701–3718, 2016.

[72] N J Lutsko, I M Held, and P Zurita-Gotor. Applying the fluctuation-dissipation theorem to a two-layer model of quasi-geostrophic turbulence. *Journal of the Atmospheric Sciences*, 72:3161–3177, 2015.

[73] A J Majda, R Abramov, and M Grote. *Information Theory and Stochastics for Multiscale Nonlinear Systems.* American Mathematical Society, 2005.

[74] A J Majda, B Gershgorin, and Y Yuan. Low-Frequency Climate Response and Fluctuation–Dissipation Theorems: Theory and Practice. *Journal of the Atmospheric Sciences*, 67(4):1186–1201, 2010.

[75] M Mak. A study of topographically induced multiple equilibria and low-frequency variability. i. idealized topography. *Quarterly Journal of the Royal Meteorological Society*, 115(485):45–7, 1989.

[76] S Manabe and T B Terpstra. The effects of mountains the general circulation of the atmosphere as identified by numberical experiments. *Journal of the Atmospheric Sciences*, 31(14):3–42, 1974.

[77] Iris Manola, Frank Selten, Hylke de Vries, and Wilco Hazeleger. waveguidability of idealized jets. *Journal of Geophysical Research: Atmospheres*, 118(18):10,432–10,440, 2013.

[78] R S Martynov and Y M Nechepurenko. Finding the response matrix for a discrete linear stochastic dynamical system. *Journal of Computational Mathematics and Mathematical Physics*, 44:771–781, 2004.

[79] T Matsuno. Quasi-geostrophic motions in the equatorial area. *Journal of the Meteorological Society of Japan*, 44:25–42, 1966.

[80] T M Merlis and T Schndeider. Atmospheric dynamics of earth-like tidally locked aquaplanets. *Journal of Advances in Modeling Earth Systems*, 2(13):1–17, 2010.

[81] J L Mitchell and G K Vallis. The transition to superrotation in terrestrial atmospheres. *Journal of Geophysical Research*, 115(12):4118–4126, 2010.

[82] G R North, T L Bell, R F Calahan, and F J Moeng. Sampling Errors in the Estimation of Empirical Orthogonal Functions. *Monthly Weather Review*, 110(7):699–706, 1982.

[83] A H Oort and E R Rasmusson. Atmospheric Circulation Statistics, NOAA Professional Paper No. 5. Technical report, U.S. Government Printing Office, 1971.

[84] I Orlanksi. Bifurcation in eddy life cycles: Implications for storm track variability. *Journal of the Atmospheric Sciences*, 60(14):993–1023, 2003.

[85] A K O'Rourke and G K Vallis. Jet interaction and the influence of a minimum phase speed bound on the propagation of eddies. *Journal of the Atmospheric Sciences*, 70:2614–2628, 2013.

[86] A K O'Rourke and G K Vallis. Meridional rossby wave generation and propagation in the maintenance of the wintertime tropospheric double jet. *Journal of the Atmospheric Sciences*, 73:2179–2201, 2016.

[87] Hoerling M P, A Kumar, and M Zhong. El nio, la nia, and the nonlinearity of their teleconnections. *Journal of Climate*, 10(8):1769–1786, 1997.

[88] R L Panetta, I M Held, and R T Pierrehumbert. External rossby waves in the two-layer model. *Journal of the Atmospheric Sciences*, 44:2924–2933, 1987.

[89] V Pavan and I M Held. The diffusive approximation for eddy fluxes in baroclinically unstable jets. *Journal of the Atmospheric Sciences*, 53:1262–1272, 1996.

[90] Vladimir Petoukhov, Stefan Rahmstorf, Stefan Petri, and Hans Joachim Schellnhuber. Quasiresonant amplification of planetary waves and recent northern hemisphere weather extremes. *Proceedings of the National Academy of Sciences*, 110(14):5336–5341, 2013.

[91] N A Phillips. The general circulation of the atmosphere: A numerical experiment. *Quaterly Journal of the Royal Meteorological Society*, 82:123–164, 1956.

[92] R A Plumb. On the three-dimensional propagation of stationary waves. *Journal of the Atmospheric Sciences*, 42(3):217 – 229, 1985.

[93] L M Polvani, J G Esler, and R A Plumb. Time variability and simmons-wallace-branstator instability in a simple nonlinear model. *Journal of the Atmospheric Sciences*, 56(23):1445–1460, 1999.

[94] S F Potter, G K Vallis, and J L Mitchell. Spontaneous superrotation and the role of kelvin waves in an idealized dry gcm. *Journal of the Atmospheric Sciences*, 71(7):596–614, 2014.

[95] W J Randel and I M Held. Phase speed spectra of transient eddy fluxes and critical layer absorption. *Journal of the Atmospheric Sciences*, 48:688–697, 1991.

[96] M M Rienecker, M J Suarez, R Gelaro, R Todling, J Bacmeister, E Liu, M G Bosilovich, Schubert S D, L Takacs, G K Kim, S Bloom, J Chen, D Collins, A Conaty, and A da Silva. Merra: Nasa's modern-era retrospective analysis for research and applications. *Journal of Climate*, 24:3624–3648, 2011.

[97] M J Ring and R A Plumb. The Response of a Simplified GCM to Axisymmetric Forcings: Applicability of the Fluctuation–Dissipation Theorem. *Journal of the Atmospheric Sciences*, 65(12):3880–3898, 2009.

[98] T Ringler and K H Cook. Orographically induced stationary waves: Dependence on latitude. *Journal of the Atmospheric Sciences*, 52(14):2548–2560, 1995.

[99] Todd D. Ringler and Kerry H. Cook. Factors controlling nonlinearity in mechanically forced stationary waves over orography. *Journal of the Atmospheric Sciences*, 54(22):2612–2629, 1997.

[100] W A Robinson. On the self-maintenance of midlatitude jets. *Journal of the Atmospheric Sciences*, 63:2109–2122, 2006.

[101] S Saeed, N Van Lipzig, W A Mller, F Saeed, and D Zanchettin. Influence of the circumglobal wave-train on european summer precipitation. *Climate Dynamics*, 43:503–515, 2014.

[102] Barry Saltzman. A generalized solution for the large-scale, time-average perturbations in the atmosphere. *Journal of the Atmospheric Sciences*, 20(3):226–235, 1963.

[103] Barry Saltzman. On the theory of the winter-average perturbations in the troposphere and stratosphere. *Monthly Weather Review*, 93(4):195–211, 1965.

[104] R Saravanan. Equatorial superrotation and mainenance of the general circulation in two-level models. *Journal of the Atmospheric Sciences*, 50:1211–1227, 1993.

[105] P D Sardeshmukh and B J Hoskins. The generation of global rotational flow by steady idealized tropical divergence. *Journal of the Atmospheric Sciences*, 45(7):1228–1251, 1988.

[106] T Schneider. The tropopause and the thermal stratification in the extratropics of a dry atmosphere. *Journal of the Atmospheric Sciences*, 61(12):1317–1340, 2004.

[107] T Schneider and S Bordoni. Eddy-mediated regime transitions in the seasonal cycle of a hadley circulation and implications for monsoon dynamics. *Journal of the Atmospheric Sciences*, 65:915–934, 2008.

[108] T Schneider and J Liu. Formation of jets and equatorial superrotation on jupiter. *Journal of the Atmospheric Sciences*, 66(7):579–601, 2009.

[109] F M Selten, B W Branstator, H A Dijkstra, and M Kliphuism. Tropical origins for recent and future northern hemisphere climate change. *Journal of Geophysical Research: Atmospheres*, 32(21):L21205, 2004.

[110] K M Shell and I M Held. Abrupt transition to strong superrotation in an axisymmetric model of the upper troposphere. *Journal of the Atmospheric Sciences*, 61(21):2928–2935, 2004.

[111] T G Shepherd. Atmospheric circulation as a source of uncertainty in climate change projections. *NATURE GEOSCIENCE*, 7(11):703–708, 2014.

[112] Adam P. Showman and Lorenzo M. Polvani. The matsuno-gill model and equatorial superrotation. *Geophysical Research Letters*, 37(18), 2010. L18811.

[113] Adam P. Showman and Lorenzo M. Polvani. Equatorial superrotation on tidally locked exoplanets. *The Astrophysical Journal*, 738(71):1–24, 2011.

[114] A. J. Simmons, J. M. Wallace, and G. W. Branstator. Barotropic wave propagation and instability, and atmospheric teleconnection patterns. *Journal of the Atmospheric Sciences*, 40(6):1363–1392, 1983.

[115] I R Simpson, M Blackburn, J D Haigh, and S N Sparrow. The impact of the state of the troposphere on the response to stratospheric heating in a simplified gcm. *Journal of Climate*, 23:6166–6185, 2010.

[116] J. Smagorinsky. The dynamical influence of large-scale heat sources and sinks on the quasi-stationary mean motions of the atmosphere. *Quarterly Journal of the Royal Meteorological Society*, 79(341):342–366, 1953.

[117] A Sobel, J Nilsson, and L M Polvani. The weak temperature gradient approximation and balanced tropical moisture waves. *Journal of the Atmospheric Sciences*, 58:3650–3665, 2001.

[118] A H Sobel and E D Maloney. An idealized semi-empirical framework for modeling the madden-julian oscillation. *Journal of the Atmospheric Sciences*, 69(21):1691–1705, 2012.

[119] Paul W. Staten and Thomas Reichler. On the ratio between shifts in the eddy-driven jet and the hadley cell edge. *Climate Dynamics*, 42(5):1229–1242, 2014.

[120] M J Suarez and D G Duffy. Terrestrial superrotation: A bifurcation of the general circulation. *Journal of the Atmospheric Sciences*, 49(7):1541–1554, 1992.

[121] K L Swanson, Kushner P J, and I M Held. Dynamics of barotropic storm tracks. *Journal of the Atmospheric Sciences*, 54(7):791–810, 1997.

[122] A F Thompson. Jet formation and evolution in baroclinic turbulence with simple topography. *Journal of Physical Oceanography*, 40:257–278, 2010.

[123] M F Ting. Steady linear response to tropical heating in barotropic and baroclinic models. *Journal of the Atmospheric Sciences*, 53(12):1698–1709, 1996.

[124] M-F Ting and I M Held. The stationary wave response to a tropical sst anomaly in an idealized gcm. *Journal of the Atmospheric Sciences*, 47(21):2546–2566, 1990.

[125] M F Ting and Hoerling M P. Dynamics of stationary wave anomalies during the 1986/87 el nio. *Climate Dynamics*, 9(3):1698–1709, 1993.

[126] A. Trevisan and A. Buzzi. Stationary response of barotropic weakly nonlinear rossby waves to quasi-resonant orographic forcing. *Journal of the Atmospheric Sciences*, 37(5):947–957, 1980.

[127] K. K. Tung and R. S. Lindzen. A theory of stationary long waves. part i: A simple theory of blocking. *Monthly Weather Review*, 107(6):714–734, 1979.

[128] E Tziperman and B Farrell. The pliocene equatorial temperature lessons from atmospheric superrotation. *Paleoceanography*, 24, 2009. PA1101.

[129] G K Vallis. *Atmospheric and Oceanic Fluid Dynamics*. Cambridge University Press, Cambridge, UK, 1 edition, 2006.

[130] G K Vallis, P Zurita-Gotor, C Cairns, and J Kidston. Response of the large-scale structure of the atmosphere to warming. *Quaterly Journal of the Royal Meteorological Society*, 2014.

[131] C C Walker and T Schneider. Eddy influences on hadley circulations: Simulations with an idealized gcm. *Journal of the Atmospheric Sciences*, 63(7):3333–3350, 2006.

[132] Christopher C. Walker and Gudrun Magnusdottir. Nonlinear planetary wave reflection in an atmospheric GCM. *Journal of the Atmospheric Sciences*, 60(2):279–286, 2003.

[133] J M Wallace and D S Gutzler. Teleconnections in the geopotential height field during the northern hemisphere winter. *Monthly Weather Review*, 109(12):784–812, 1981.

[134] Lei Wang and Paul J. Kushner. Interpreting stationary wave nonlinearity in barotropic dynamics. *Journal of the Atmospheric Sciences*, 67(7):2240–2250, 2010.

[135] P Wang and J L Mitchell. Planetary ageostrophic instability leads to superrotation. *Geophysical Research Letters*, 41(12):4118–4126, 2014.

[136] D S Wilks. *Statistical Methods in the Atmospheric Sciences.* International Geophysics. Academic Press, 2nd edition, 2006.

[137] P Zurita-Gotor. The relation between baroclinic adjustment and turbulent diffusion in the two-layer model. *Journal of the Atmospheric Sciences*, 64:1284–1300, 2007.

[138] P Zurita-Gotor. On the sensitivity of zonal-index persistence to friction. *Journal of the Atmospheric Sciences*, 71:3788–3800, 2014.

[139] P Zurita-Gotor, J Blanco-Fuentes, and E P Gerber. The impact of baroclinic eddy feedback on the persistence of jet variability in the two-layer model. *Journal of the Atmospheric Sciences*, 71:410–429, 2014.

[140] P Zurita-Gotor, J Blanco-Fuentes, and E P Gerber. The Impact of Baroclinic Eddy Feedback on the Persistence of Jet Variability in the Two-Layer Model. *Journal of the Atmospheric Sciences*, 71(1):410–429, 2014.